Effect of Background Turbulence on an Axisymmetric Turbulent Jet

by

Babak Khorsandi

Department of Civil Engineering and Applied Mechanics
McGill University
Montréal, Canada.
June 2011

A thesis submitted to McGill University
in partial fulfillment of the requirements of the degree of
Doctor of Philosophy

Abstract

The effect of background turbulence on a turbulent jet was investigated experimentally. The primary objective of this work was to study the effect of different levels of the background turbulence on the dynamics and mixing of an axisymmetric turbulent jet at different Reynolds numbers. The secondary objective, which arose during the experiments, was to improve the acoustic Doppler velocimetry measurements which were found to be inaccurate when measuring turbulence statistics.

In addition to acoustic Doppler velocimetry (ADV), flying hot-film anemometry was employed in this study. To move the hot-film probe at constant speeds, a high precision traversing mechanism was designed and built. A data acquisition system and LabVIEW programs were also developed to acquire data and control the traversing mechanism. The experiments started by benchmarking the two measurement techniques in an axisymmetric turbulent jet. Comparing the results with those of the other studies validated the use of flying hot-film anemometry to estimate the mean and the root-mean square (RMS) velocities. The experiments also validated the use of ADV for measurement of the mean velocities (measured in three Cartesian directions) and the RMS velocity (measured in the z-direction only). RMS velocities measured by the ADV along the x- and y-direction of the probe were overestimated.

Attempts to improve the turbulence statistics measured by the ADV using the post-processing and noise-reduction methods presented in the literature were undertaken. However, the RMS velocities remained higher than the accepted values. In addition, a noise-reduction method was presented in this study which reduced the RMS velocities down to the accepted values. It was also attempted to relate Doppler noise to current velocity, and thus improve the results by

subtracting the Doppler noise from the measured RMS velocities in the jet. However, no relationship was found between the Doppler noise and the mean velocity.

The effect of different levels of background turbulence on the dynamics and mixing of an axisymmetric turbulent jet at different Reynolds numbers was then investigated. The background turbulence was generated by a random jet array. To confirm that the turbulence is approximately homogeneous and isotropic and has a low mean flow, the background flow was first characterized. Velocity measurements in an axisymmetric jet issuing into two different levels of background turbulence were then conducted. Three different jet Reynolds numbers were tested ($Re = U_J D/\nu$, where U_J is the jet exit velocity, D is the exit diameter of the jet, and ν is the kinematic viscosity). The results showed that (compared to the jet in a quiescent ambient) the mean axial velocities decay faster in the presence of background turbulence, while the mean radial velocities increase, especially close to the edges of the jet. At lower Reynolds numbers, the jet structure was destroyed in the near-field of the jet. The increase in the level of the background turbulence resulted in a faster decay of the mean axial velocities. The RMS velocity of the jet issuing into the turbulent background also increased, indicating that the level of turbulence in the jet increases. In addition, the jet's width increased in the presence of the background turbulence. The mass flow rate of the jet decreased in the presence of the background turbulence from which it can be inferred that the entrainment into the jet is reduced. The effect of background turbulence on entrainment mechanisms – large-scale engulfment and small-scale nibbling – is discussed. It is concluded that in the presence of background turbulence, engulfment is expected to be the main entrainment mechanism.

Sommaire

L'effet de la turbulence ambiante sur l'évolution d'un jet turbulent est étudié dans le cadre de cette recherche expérimentale. L'objectif primaire de ce travail est l'étude de l'effet de l'intensité de la turbulence ambiante sur l'évolution d'un jet turbulent, à trois nombres de Reynolds différents. L'objectif secondaire est l'amélioration des mesures de vélocimétrie acoustique Doppler qui se sont avérées inexactes au cours de ce travail.

Un dispositif à anémométrie à fil chaud volant a aussi été développé pour effectuer des mesures dans le cadre de cette étude. A cette fin, un mécanisme de translation a été conçu pour déplacer la sonde à vitesse constante. Un système d'acquisition de données et des programmes LabVIEW ont été développés pour enregistrer les données et contrôler le mécanisme. De premières expériences (dans un jet turbulent axisymétrique en milieu tranquille) ont prouvé le bien-fondé i) des mesures de vitesses moyenne et moyenne quadratique par anémométrie à fil chaud volant, et ii) des mesures de vitesse moyenne (dans tous le sens) et de vitesse moyenne quadratique (dans le sens z) par vélocimétrie acoustique Doppler. Les mesures par vélocimétrie acoustique Doppler dans les sens x et y étaient surestimées.

L'amélioration des mesures de vitesse moyenne quadratique par vélocimétrie acoustique Doppler a été tentée par moyen de techniques de réduction de bruit existantes. Néanmoins, les vitesses moyennes quadratiques restaient surestimées. Une nouvelle technique de réduction de bruit (qui avait pour résultat des vitesses moyennes quadratiques précises) a été proposée dans le cadre de cette étude. En outre, des expériences ayant pour but de quantifier le rapport entre le bruit Doppler et la vitesse de l'écoulement ont été entreprises (pour pouvoir soustraire le bruit Doppler des mesures de vitesses moyennes

quadratiques). Cependant, celles-ci n'ont trouvé aucun rapport entre ces deux quantités.

Par la suite, l'effet de l'intensité de la turbulence ambiante sur l'évolution d'un jet turbulent axisymétrique, à trois nombres de Reynolds différents, a été étudié. La turbulence ambiante a été produite par moyen d'une maille de jets aléatoires. La turbulence ambiante s'est avérée, par moyen de mesures d'anémométrie à fil chaud volant et de vélocimétrie acoustique Doppler, homogène est isotrope. L'évolution d'un jet turbulent (à trois nombres de Reynolds) émis en milieux turbulents (de deux intensités différentes) a ensuite été étudiée. Les mesures ont démontré que la turbulence ambiante i) réduisait la vitesse axiale moyenne du jet (en augmentant le taux de décroissance), et ii) augmentait la vitesse radiale moyenne du jet (surtout prés du bord du jet). Pour les jets à nombre de Reynolds bas, la structure du jet a été détruite dans le champ proche du jet. Les vitesses moyennes quadratiques du jet émis en milieu turbulent étaient plus grandes, indiquant une croissance du niveau de turbulence dans le jet. En outre, la demi-largeur du jet augmentait en milieu turbulent. Par contre, en environnement turbulent, le débit massique du jet émis a diminué, ce qui implique que le taux d'entraînement du jet est aussi réduit. L'effet de la turbulence ambiante sur les mécanismes de l'entraînement (par engloutissement à grande échelle ou par grignotage) est examiné. Il est conclu que, en environnement turbulent, l'engloutissement est le mécanisme d'entraînement principal.

Acknowledgements

The completion of this research project was not possible without the assistance of many people. I am greatly thankful to my supervisors, Prof. Laurent Mydlarski and Prof. Susan Gaskin. I continuously had their support and guidance during my Ph.D. studies. I am also grateful to Prof. Laurent Mydlarski from whom I gained a knowledge of turbulence.

I would like to acknowledge the funding provided by the Natural Sciences and Engineering Research Council of Canada and the Fonds québécois de la recherche sur la nature et les technologies.

Members of technical staff helped me in the design and construction of the experimental setup. I would like to thank John Bartczak for his thoughtful suggestions during the design and construction and his assistance in constructing the setup. I am also thankful to Marek Przykorski who helped me with the electronics and provided me with tools. George*s* Tewfik and Mario Iacobaccio generously lent me electrical tools, which I appreciate. Jorge Sayat and Dr. William Cook were helpful with my computer and internet problems in the laboratory.

I would also like to sincerely thank fellow graduate students at the turbulence research group, Jason Lepore and Arpi Berajeklian who taught me how to use the hot-film/wire anemometry for velocity measurements and who gave suggestions on the measurement techniques. I also thank Prof. Sofia Babarutsi for her suggestions pertaining to hot-film anemometry. I am also thankful to my friend, Arash Kashi who spent couple of days to help me with the electronics of the traversing mechanism. I am grateful to all my friends who supported me during my studies, especially Colleen Gosse.

Finally, I would like to express my deepest gratitude to my family, my parents, brother and sister who continually supported me throughout my studies as well as the other stages of life.

Table of Contents

List of Figures

List of Tables

Nomenclature

A, B, n	constants pertaining to the calibration curve fits
A	Area
B	velocity decay constant of the jet
B_D	total Doppler bandwidth broadening
B_d	RMS contributions of beam divergence to B_D
B_r	RMS contributions of finite residence time to B_D
B_t	RMS contributions of turbulence to B_D
c	entrainment rate
c	speed of sound in water
D	jet nozzle diameter
d	transverse size of the sampling volume of the ADV
d_p	diameter of particles
E	mean voltage output of the anemometer
E_{DAQ}	input voltage span of A/D board
f	frequency
f_{ADV}	Operating frequency of ADV
K	kurtosis
L	length scale
ℓ	integral length scale of the jet
M	centre to centre distance between RJA jets
M	momentum flow rate
M_I	initial momentum flow rate
M_{ADV}	number of acoustic pulses averaged for calculating the velocities by the ADV

m	mass flow rate of the jet
m_0	initial mass flow rate of the jet
Nu	Nusselt number
R_{cold}	cold resistance of the sensor
R_{op}	operating resistance of the sensor
Re	Reynolds number based on U_J, D, and v
Re_T	turbulent Reynolds number based on u_{rms}, L, and v
r	jet radial coordinate
$r(x)$	local jet radius
$r_{1/2}$	jet velocity half-width
S	skewness
S	spreading rate of the jet
St	Stokes number
T	temperature
T_a	ambient flow temperature
T_{ADV}	time between two successive estimates of velocity by the ADV sensor
t_0	time that takes the ADV sensor to carry out the conversions
t	time
U	mean axial velocity component
U_c	cross-beam or transverse velocity component measured by the ADV
U_{CL}	centreline mean axial velocity
$U_{CL}(x)$	local centreline mean axial velocity component
U_{curve}	velocity predicted by the calibration curve-fit
U_h	mean horizontal velocity measured by the ADV
U_J	jet exit velocity
U_{TM}	traversing mechanism velocity
ΔU	variation of the velocity across the sampling volume of the ADV
u	fluctuating axial velocity component
u_i	fluctuating velocity in the i-direction

u_{rms}	RMS axial velocity
V	mean radial velocity component
v	fluctuating radial velocity component
v_{rms}	RMS radial velocity
W	mean radial velocity component
w	fluctuating radial velocity component
w_{rms}	RMS radial velocity
x	jet axial coordinate
x_i	coordinate in the i-direction
x_0	virtual origin

Greek Symbols

α	entrainment coefficient
ε	turbulent kinetic energy dissipation rate
$\Delta\theta$	bistatic angle of the ADV
κ	wavenumber
κ_1	longitudinal wavenumber
μ	dynamic viscosity
μ_{off}	average off time of random jet array pumps
μ_{on}	average on time of random jet array pumps
ν	kinematic viscosity
π	3.1415926
ρ	jet fluid density
ρ_p	density of particles
σ_{off}	standard deviation of off time
σ_{on}	standard deviation of on time
σ_D^2	Doppler noise contribution to the noise variance
σ_i^2	noise variance along the i-direction
σ_m^2	sampling error contribution to the noise variance
σ_t^2	noise variance along each receiver beam of the ADV

σ_u^2	mean velocity shear within the sampling volume contribution to the noise variance
τ	time between acoustic signal transmissions by the ADV
τ_p	particle response time
Φ	ADV transmitted signal phase
Ω	mean vorticity
ω	fluctuating vorticity

Superscripts and Symbols

°	degree
$\langle \cdot \rangle$	denotes averaging

Subscripts

CL	pertains to centreline quantity
RMS or *rms*	pertains to root-mean square quantity
i	index in tensor notation and pertains to the variable in *i*-direction

Acronyms

ADV	acoustic Doppler velocimeter
FPGA	field-programmable gate array
LIF	laser-induced fluorescence
OHR	overheat ratio
PDF	probability density function
PIV	particle image velocimetry
RJA	random jet array
RMS	root-mean square
SNR	signal-to-noise-ratio
TKE	turbulent kinetic energy

Chapter 1

Introduction

1.1 Background

Industrial activities often result in large quantities of pollutants being discharged into the atmosphere and the hydrosphere (rivers, lakes, oceans) in the form of turbulent jets or plumes. These damage the ecosystem and endanger human health. Dilution of such jets and plumes, which is due to entrainment and mixing of the ambient fluid with the effluents, reduces the acute toxic effects of the pollutants. A higher initial dilution can minimize the immediate effect of the discharge at the point of release and leads to higher dilutions downstream. These impacts necessitate the study and characterization of such phenomena.

Historically, most jet studies have been carried out in quiescent background flows. Consequently their results may not be valid for the prediction of the discharge of effluents into a turbulent environment. The jet's dynamics and entrainment depend on both the parameters of the jet, as well as the environmental parameters characterizing the fluid into which the jet is discharged. These latter parameters include: i) the background turbulence intensity, ii) mean flow advection, iii) density stratification, and iv) the presence of boundaries. It is a

complicated task to account for all the parameters mentioned above as they all have complex effects on the jet. To quantify their individual contributions, it is beneficial to study the effect of one environmental parameter at a time on the dilution of a jet. The environmental turbulence, which is usually present in the receiving fluid, can be expected to have a significant effect on the entrainment into and mixing within the jet. Therefore, to predict and characterize the behaviour of jets in the environment, the study of the jets in the presence of a turbulent background is necessary.

The most common assumption (hypothesis) has been that background turbulence will increase the dilution of the jet due to superposition of the jet dilution and turbulent dispersion (*e.g.,* Wright, 1994). Studies on the effect of oscillating grid turbulence on a jet/plume have been inconclusive due to the jet/plume axis being perpendicular to the grid resulting in background turbulence level increasing in the downstream direction of the jet/plume (*i.e.*, as the jet/plume turbulence level decreased — Ching *et al.* 1995, Guo *et al.* 1999, Law *et al.*, 2001, Guo *et al.* 2005, Cuthbertson *et al*., 2006). On the other hand, Hunt (1994) hypothesized that background turbulence could lower dilution rates by breaking up the jet structure. Experiments have provided qualitative confirmation of this hypothesis (Gaskin *et al.*, 2004). Consequently, it is clear that a thorough and systematic study of jets in background turbulence is required to further confirm or refute the above hypotheses.

1.2 Objectives

This work is an experimental investigation into the effect of background turbulence on a momentum-driven, axisymmetric, turbulent jet. For such a study, the most fundamental background turbulence is desired, which would be homogeneous isotropic turbulence with zero mean flow. Such a background flow will be generated using a random jet array (RJA). Several RJA algorithms will be tested to create the closest approximation to isotropic turbulence with zero-mean

flow. Subsequently, the homogeneity and isotropy of the turbulence will be verified.

The main objective is to study the effect of background turbulence on the dynamics and mixing of an axisymmetric turbulent jet. Initially, the measurement techniques must be benchmarked and compared to results in the literature. Therefore, the statistics of the velocity field of the jet in a quiescent flow will be measured by acoustic Doppler velocimetry and flying hot-film anemometry. The results will be compared to those in the literature to validate the measurement techniques. Subsequently, the effect of background turbulence on the dynamics and mixing of the jet will be investigated. Velocity measurements of the jet propagating into different levels of background turbulence will be measured by acoustic Doppler velocimetry and flying hot-film anemometry. Both axial and radial statistics are required to determine the changes in the evolution of the jet. The effect of background turbulence on the jet mixing and therefore entrainment into the jet will be studied by measuring the mass flow rate of the jet. The jet Reynolds numbers will be varied in the range of 5,300 to 10,600, because, as shown by Dimotakis (2000), there is a mixing transition at $Re \approx 1\text{-}2 \times 10^4$ above which the turbulent flow becomes better mixed. Therefore, the Reynolds number of 10,600 is initially chosen as it is above the mixing transition and it was also tested previously in our laboratory. It will be shown that at $Re = 10{,}600$ the jet did not completely destroy due to the effect background turbulence within our measurement range. Therefore, to further investigate the effect of background turbulence on the jet, the Reynolds number was reduced to 5,300.

The secondary objective of this work, which arose during the experiments, is to investigate the noise in the turbulence measurements made using acoustic Doppler velocimetry. To improve the turbulence statistics measured with an acoustic Doppler velocimeter/using acoustic Doppler velocimetry (both abbreviated ADV, herein), post-processing and noise-reduction methods will be tested on the data. An attempt to relate the ADV noise to the mean velocity, and estimate its effect on the turbulence statistics, will also be undertaken.

1.3 Organization of the Thesis

The rest of this thesis is structured as follows. Chapter 2 reviews the literature of i) the dynamics and mixing of a turbulent jet issuing into a quiescent background, ii) homogeneous isotropic turbulence generated by oscillating grid turbulence and random jet arrays, iii) the effect of background turbulence on the dynamics and mixing of a jet/plume, and iv) the measurement techniques, which include acoustic Doppler velocimetry and hot-film anemometry.

Chapter 3 explains the experimental setup. This includes the apparatus used to conduct the experiments such as the jet, the random jet array, and the filtration system in the water tank. In addition, the setup of the measurement apparatus, the ADV and the flying hot-film anemometer, and their traversing mechanisms, along with the data acquisition components and programs are described. Calibration of the flying hot-film is also explained in this chapter.

The results of the validation of flow measurements experiments are presented in Chapter 4. The benchmarking of the ADV and the flying hot-film anemometer in an axisymmetric turbulent jet issued into a quiescent background will be presented. The results are compared to those of the other studies.

The results and discussion of the experiments are presented in Chapter 5. The first section of this chapter (§5.1) attempts to improve the turbulence statistics measured with the ADV as well as to relate the ADV's Doppler noise to the mean velocity. The effect of background turbulence on the jet is presented in §5.2. A quantification of the background turbulence generated by the random jet array is first discussed in §5.2.1. Velocity statistics, spectra, along with estimates of the decay and homogeneity of the flow will be presented. This is followed by the results pertaining to the turbulent jet issued into the turbulent background in §5.2.2. The effect of two different levels of background turbulence on the mean velocities, RMS velocities, half-widths and the entrainment into the jet are investigated. Results for three different jet Reynolds numbers will be presented. Finally §5.3 provides a discussion of results.

Chapter 6, the final chapter of this thesis, presents the conclusions. The first section provides a summary of the thesis. Next, the novel contributions of this work are presented. Finally, recommendations for the future work are proposed.

Chapter 2

Literature Review

In this chapter, a review of the literature on the following topics is presented: i) turbulent jets, ii) homogeneous isotropic turbulence, iii) the effect of background turbulence on jets, and iv) acoustic Doppler velocimetry and hot-film anemometry.

2.1 Turbulent Jets

Turbulent jets are one of the most commonly studied free shear flows. They are a common occurrence, as well as serving as a typical model for more complex flows. The jet is best described in cylindrical coordinates. Here, the focus is on stationary, axisymmetric, turbulent jets, for which the azimuthal components are zero (as there is no swirl) and the statistics are only dependent on the axial and radial coordinates. The jet mean flow is predominantly in the axial direction and, due to the gradual spread of flow, the axial gradients are small compared to lateral ones. Therefore, the boundary layer equations are applicable for modelling its behaviour (Pope 2000). The (appropriately simplified) mean equations of conservation of mass and momentum are:

$$\frac{\partial\langle U\rangle}{\partial x}+\frac{1}{r}\frac{\partial\left(r\langle V\rangle\right)}{\partial r}=0\text{, and} \tag{2.1}$$

$$\langle U\rangle\frac{\partial\langle U\rangle}{\partial x}+\langle V\rangle\frac{\partial\langle U\rangle}{\partial r}=\frac{\nu}{r}\frac{\partial}{\partial r}\left(r\frac{\partial\langle U\rangle}{\partial r}\right)-\frac{1}{r}\frac{\partial}{\partial r}\left(r\langle uv\rangle\right) \tag{2.2}$$

where U is the axial velocity, V is the radial velocity, x is the axial direction, r is the radial direction, u is the fluctuating component of axial velocity, v is the fluctuating component of radial velocity, ν is the kinematic viscosity, and $\langle\cdot\rangle$ denotes averaging.

The jet is characterized by U_J, D, and ν, or the non-dimensional parameter called the Reynolds number, which is the ratio of inertial to viscous forces: $Re = U_J D/\nu$. U_J is the velocity of the fluid at the exit of the nozzle and D is the nozzle diameter of the jet (Pope 2000).

The profiles of the mean velocity and Reynolds stresses ($<u_i u_j>$) decay and spread as the downstream distance is increased. After the initial developing region, the jet becomes self-similar and independent of the jet's Reynolds number (Wygnanski and Fiedler, 1969). That means that properly non-dimensionalized quantities become independent of the downstream distance, and their radial profiles collapse into a single curve. However, the start of the self-similarity region depends on the quantity being measured as well as the initial conditions (Xu and Antonia, 2002). The mean axial velocity becomes self-similar sooner than higher-order statistics. In the self-preserving region, the mean velocity profile of the jet can be approximated by a Gaussian distribution (Fischer *et al.*, 1979; Turner, 1986) or a polynomial (Pope, 2000).

Self-similarity implies that the centerline mean velocity, as well as the width of the jet, scales with the downstream distance. Evidently, the inverse of the centerline mean velocity and the rate of spread of jet or half-width (where the velocity reaches half of that of the centerline velocity, denoted as $r_{1/2}$), vary linearly with the downstream distance. Therefore the local Reynolds number is independent of the downstream distance (Pope, 2000). To maintain self-similarity,

the turbulence statistics must also preserve the same properties. Therefore, the magnitude of the dimensionless turbulence quantities, such as the ratio of the RMS velocity and mean velocity (*e.g.*, $u_{rms}/\langle U \rangle$) should be constant and independent of the downstream distance (Tennekes and Lumley 1972).

The mean radial velocity component ($\langle V \rangle$), which is very small (less than 40 times smaller than the centerline mean axial velocity), can be determined from the continuity equation given the known axial velocity component. The mean radial velocity is positive in the jet, but due to entrainment of ambient fluid into the jet, it becomes negative at its edge (Pope, 2000).

As the jet develops downstream, the surrounding fluid is drawn radially into the jet through its conical surface. This process is known as entrainment (Ricou and Spalding, 1960). Turbulent jets entrain and mix large volumes of ambient fluid with the discharged fluid. Therefore, as the jet develops downstream, its mass flow rate increases (while its momentum flow rate remains conserved). The high entrainment rates and therefore a strong capacity to mix means the jet is an effective mechanism for the discharge of pollutants into the environment. The dilution of discharged fluid by entraining the ambient fluid reduces the detrimental effects of pollutants on the environment.

The parameters that govern the behaviour of the jet, such as entrainment and mixing, include its mass flow rate and momentum flow rate. The mass flow rate quantifies the amount of fluid moving across the jet cross-section per unit time and is given by: $m = \int_A \rho U dA$, where ρ is the density of the fluid, U is the axial velocity and A is the cross section area of the jet. The momentum flow rate measures the rate at which axial momentum is transported across the jet cross-section and is given by: $M = \int_A \rho U^2 dA$. Higher mass and momentum flow rates result in more entrainment and mixing. The Reynolds number is proportional to $M_I^{1/2}/\nu$, where M_I is the initial (specific) momentum flow rate of jet (Fischer *et al.*, 1979).

In the zone of flow establishment of an axisymmetric turbulent jet, there is large-scale entrainment by organized vortical structures shed from the discharging flow, similar to that seen in shear layers. Such structures, however, do not extend downstream for more than a few jet diameters where these vortex rings break down. The initial development region is followed by the near-field of the jet (where the jet becomes self-similar). In this region, two main entrainment mechanisms have been proposed: engulfment and nibbling. Engulfment is a large-scale inviscid process in which large volumes of ambient fluid are drawn into the shear flow by large eddies. Subsequent mixing is carried out by viscous diffusion of vorticity (*e.g.*, Townsend, 1956; Brown and Roshko, 1974). The flow visualization and measurements of the scalar concentration field by Dahm and Dimotakis (1987, 1990) confirms the existence of entrainment by engulfment and shows that the entrainment and mixing processes in the near-field of a turbulent jet can be characterized by scales approximately equal to the local large scales of the flow. The instantaneous concentration profiles from their work also show that the (unmixed) ambient fluid was transported deep into the jet. This is mentioned as further evidence for large-scale entrainment. Nibbling is a small-scale viscous process that occurs by small-scale eddies at the very thin interface (on the order of the Kolmogorov microscale, the smallest scale in the turbulent flow) between turbulent and non-turbulent flows. This interface or "laminar super-layer" plays a significant role in transmitting the vorticity to irrotational fluid by tangential viscous forces (and not by macroscopic shear forces), unlike the momentum transfer, which is dominated by velocity fluctuations (Corrsin and Kistler, 1955). Although there exists a debate as to the relative importance of the two processes, recent direct numerical simulations by Mathew and Basu, (2002) have shown nibbling to be the dominant entrainment process. In their simulations, they defined a vorticity threshold level. If the threshold was crossed, the fluid was part of the turbulent jet. If engulfment was the dominant mechanism, there should be areas in the jet with vorticity below the threshold level and the positions where the threshold was crossed should be distributed within the jet. However, as the threshold was mostly crossed at the interface, the nibbling is expected to be the

main entrainment mechanism. This study has also been corroborated experimentally by Westerweel *et al.* (2008), who found that nibbling at the interface is effected by small scale eddies and that the engulfed mass consists of less than 10% of the total entrained mass.

Regardless of the entrainment mechanism, as long as scale similarity exists (as is the case in a self-similar jet), the overall rate of entrainment can be predicted by characteristic (large or small) scales of the flow. However when the jet turbulence is not in equilibrium (*e.g.*, when turbulence in the ambient flow disrupts the jet structure and, consequently, the relation between the scales), the mechanism of entrainment needs to be re-investigated (Mathew and Basu, 2002). Note that most jets discharged into the environment do so into a turbulent background.

The mass and momentum flow rates of an axisymmetric jet issued into a quiescent background (with zero ambient pressure gradient) have been extensively studied, both theoretically and experimentally. Assuming self-similarity of the jet, it can be shown that the mass flow rate is proportional to $r_{1/2}(r_{1/2}U_{CL})$, where U_{CL} is the centerline velocity. Given these assumptions, the mean velocity of the jet decays as x^{-1}, and the half-width grows as x. Consequently, the mass flow rate of the jet increases linearly with downstream distance. The constant of proportionality in the fully developed region for the non-dimensionalized mass flow rate was estimated to be 0.32 by Ricou & Spalding (1961). (m/m_0=c×x/D, where m is the mass flow rate at a given downstream position, m_0 is the mass flow rate at the nozzle, c is the constant of proportionality, x is the downstream distance and D is the diameter of the nozzle.) The experimental results of Falcone & Cataldo (2003) and Crow and Champagne (1971) found c to be 0.297 and 0.292, respectively. The entrainment rate of the jet (c = dm/dx) decreases as the Reynolds number increases. This quantity becomes independent of the Reynolds number and asymptotes to a constant value at Re > 2.5×10^4 (Ricou & Spalding, 1961).

2.2 Homogeneous Isotropic Turbulence

Homogeneous, isotropic turbulence is fundamental to the study of turbulent flows. Although such a flow may not be identical to the industrial or environmental turbulence, which can be inhomogeneous, it represents a standard benchmark turbulent flow for scientific studies. To generate an approximately homogeneous, isotropic turbulent background with zero mean flow in the laboratory, either an oscillating grid or, more recently, a random jet array (RJA) have been employed. The reason for studying turbulence with negligible mean flow is to avoid the effects of (mean) advection on the flow. Therefore, the role of turbulence in both mixing and transport can be studied in isolation.

Oscillating grid turbulence is generated by a planar grid oscillating in the grid-normal direction. By the merging of the jet and wake structures produced behind the grid bars, shear-free turbulence is created downstream. On the other hand, the random jet array consists of an array of jets, which are turned on and off randomly and independently. The turbulent flow field is generated as the jets merge downstream of the random jet array. The turbulence generated by an oscillating grid turbulence system and a random jet array can be characterized by their turbulence parameters, such as the integral length scale (size of the largest eddies), as well as a variety of statistics pertaining to the velocity fluctuations (*e.g.*, u_{rms}, $<U>/u_{rms}$, *etc.*).

There have been many experimental studies of oscillating grid turbulence. To obtain an approximately homogeneous, isotropic velocity field with zero mean flow, optimal values of the geometrical parameters and oscillation frequencies have been suggested. The geometrical parameters include the grid mesh size and solidity (the ratio of the area of the bars to the total area of grid). Fernando and De Silva (1993) argued that Reynolds stress gradients can result in secondary mean flows and they therefore suggested that grids satisfying reflective-symmetry conditions (with respect to the walls) be employed to minimize the Reynolds stresses and thus significantly reduce secondary circulations so that $<U>/u_{rms} \leq$

0.1. The intensity of the turbulence is also a function of the stroke, frequency and mesh size. In the homogeneous region, the RMS velocities in the downstream and transverse directions decay as power law with distance from the grid with the exponents of -1. Consequently the turbulent kinetic energy power law decay exponent is -2 (Hopfinger and Toly, 1976). The ratio of vertical to horizontal RMS velocities, have been measured to be in the range 1.1-1.2 (De Silva and Fernando, 1994).

The main disadvantage of oscillating grid turbulence is that it is very difficult to achieve zero mean flow and secondary circulations are recognized as an intrinsic feature of such systems. (Thompson and Turner (1975) and McDougall (1979) reported $<U>/u_{rms}$ values of up to about 60%.) Moreover, sensitivity to the initial conditions and significant variability in the statistics (up to 20%) from one test to another are other disadvantages (McKenna and McGillis, 2004). Lastly, due to the oscillating grids' highly mechanical nature, they are difficult to build and to scale up for experiments requiring larger turbulent Reynolds numbers.

Other configurations and methods have been proposed to generate homogeneous, isotropic turbulence. A pair of oscillating grids was used by Srdic *et al.* (1996), which suffered from large mean flows. More recently, eight fans (Birouk *et al*., 2003) or synthetic jets (Hwang and Eaton, 2004) located at the corners of a cubic chamber and pointing towards its center have been employed. Though the desired flow is of a higher quality than that achieved by oscillating grid turbulence, it only exists in a small region in the center of the chamber and does not occur over a wide region of the flow as is the case in oscillating grid turbulence.

An alternate method for the generation of approximately homogeneous, isotropic turbulence with negligible mean flow is the random jet array (RJA), which has been developed by Variano *et al*. (2004) and Variano and Cowen (2008). It consists of a Cartesian array of jets (firing upwards) that turn on and off randomly so as to generate turbulence downstream of the array. The number of

jets which are on at a given time and the distribution of the duration of on and off times affect the flow. The optimal performance was achieved when on and off times were chosen from a normal distribution. There is negligible mean flow because i) the jet inlets are within the tank into which they expel their fluid, and ii) the random nature of the jet array decreases the probability of creating secondary flows. Their results showed that $<U_\alpha>/u_{\alpha rms}$ is smaller than 10% (in all directions), which is significantly lower than what is observed in oscillating grid turbulence. In addition, the flow is highly repeatable and reaches steady state rapidly. The flow field is homogeneous over a large region and the isotropy of the RMS velocities produced by the random jet array is of the same order as that observed in oscillating grid turbulence. Similar to the grid turbulence, the turbulence generated by the RJA decays as power law (in the homogeneous region) with distance from the jet array. The turbulent kinetic energy decays slightly faster in the RJA turbulence ($\sim x^{-2.3}$, where x is the downstream distance) compared to that of the grid generated turbulence ($\sim x^{-2}$).

2.3 The Effect of Background Turbulence on a Jet

Industrial wastes are typically discharged into the environment in the form of a jet. The dilution of the pollutant is relied upon to reduce the latter's adverse effects on the environment. The jet's dispersion depends on both the environmental and jet parameters. An understanding and characterization of such phenomena is crucial because the higher the initial dilution of the pollutants, the lower the impact on the environment. One of the main parameters is turbulence in the environment – it can highly influence the dynamics and mixing of the jet. The effect of homogeneous, isotropic turbulent background on an axisymmetric turbulent jet is the focus of this research.

Although many studies of a jet issuing into a quiescent ambient fluid exist, there have only been a few studies on the dynamics and mixing of the jet in the presence of background turbulence. There are two theories on the effect of background turbulence on the entrainment in the near-field of the jet. The first one

states that the entrainment of the jet decreases due to disruption of the jet structure by the external turbulence (*e.g.*, Hunt, 1994). The second theory supports the superposition of jet dilution and turbulent diffusion in the near-field region and therefore an increased entrainment in the presence of external turbulence (*e.g.*, Wright, 1994).

The first theory has been supported by certain studies. It is theoretically reasoned that an increased mass or momentum flow rate of a jet will increase the entrainment, while any tendency of the jet to break up into distinct eddies will decrease the entrainment (Hunt, 1994). Initially the entrainment velocity of the jet is much larger than the root mean square (RMS) velocity of the turbulent background. The external turbulence is entrained and does not vary the rate of spreading of the jet until the RMS velocities of the jet becomes of the same order as that of the ambient turbulence. At this point, the entrainment reduces significantly due to disruption of the self-similar structure of the jet. The dilution then occurs mainly due to turbulent diffusion at a rate dependent on the ambient turbulence levels. This was verified experimentally by Gaskin *et al.* (2004) for a jet in a shallow co-flow. They reject the theory of superposition of the dilution resulting from the jet driven entrainment and the background-turbulence-driven-entrainment, and confirm a reduction in the rate of dilution in the near-field once the jet self-preserving structure is disrupted. The entrainment is proportional to the characteristic velocity of the jet (Morton *et al.*, 1956) and therefore, the rate of dilution in the near-field decreases as the characteristic velocity is reduced due to the ambient turbulence.

Several studies on the effect of background turbulence (generated by an oscillating grid) on a jet/plume indicate an increased width growth and disruption of the jet/plume structure at higher background turbulence levels. In these studies, the jet/plume axis was perpendicular to the grid, therefore having background turbulence level increasing in the downstream direction of the jet/plume (*i.e.*, as jet/plume turbulence level decreased). A jet subjected to background turbulence was seen to have an increase in the rate of entrainment and rate of spreading, as

the background turbulence started to have a considerable effect on the jet structure (Law *et al.*, 2001). Guo *et al.* (1999) experimentally showed that the jet was destroyed by the turbulent background when the RMS velocity of the background turbulence reached 0.125 of the centerline jet velocity or exceeded about 0.44 times the RMS velocity of the incident jet (Guo *et al.*, 2005), the latter showing no dependence on jet Reynolds number. Ching *et al.* (1995) studied a plume in oscillating grid turbulence. Close to the plume exit, no significant effect of the background turbulence was observed. However once the convective velocity of the plume was on the order of the RMS velocity of the background turbulence, the plume started to break down, diluting rapidly while increasing its spreading angle (Cuthbertson *et al*., 2006). Final breakdown occurred when the convective velocity was less than about 1.6 times the RMS velocity of the turbulent background (Ching *et al.*, 1995). Wright (1994) found support for the theory of superposition of jet dilution and turbulent diffusion in the near-field region from examining jets released into open channel flows with increasing bed roughness (leading to increased turbulent intensities).

The effect of oscillating-grid generated turbulence on a wall jet boundary layer has also been studied (Tsai *et al*., 2007). The results showed that the size of the large-scale eddies grew while their rotation speed decreased which could suggest that the circulation was conserved. The irregularity of the flow pattern also increased. The maximum velocity of the wall jet decreased and its thickness increased in the presence of external turbulence. The fluctuations of the wall jet also increased and the largest increase was in the vicinity of the wall in the boundary layer. The background turbulence transports the jet outwards into the mixing layer. This results in a small decrease in friction on the wall.

2.4 Measurement Techniques

A literature review of the measurement techniques employed in this research is presented in this section. Acoustic Doppler velocimetry is first discussed, followed by a review of hot-film anemometry.

2.4.1 Acoustic Doppler velocimetry

In recent years, acoustic Doppler velocimetry (ADV) has been employed for the measurement of velocity, both in the field (oceans, lakes and rivers) and in the laboratory. Its advantages include: the capability of three-dimensional velocity measurements at moderately high sampling rates, the ability to measure in non-clean environments, the separation of the measurement volume and the sensor (minimizing any interference with the flow), and portability. These make the acoustic Doppler velocimeter a popular instrument for flow measurements, especially in the field.

The ADV consists of a probe, connected by either a fixed stem or a cable to the housing, which contains the electronics. The sampling volume is located approximately 50 mm below the probe, which minimizes the interference of the probe with the flow. The probe consists of a transmitter and three or four receivers, which are equally angled and symmetrically arranged around the transmitter. The ADV relies on the Doppler shift to measure the velocity of the particles suspended in the flow. In other words, the ADV transmitter sends ultrasonic pulses and the receivers collect the signals reflected off the particles in the sampling volume to infer the velocity of the fluid. The measured phase shift is converted into radial velocity by the Doppler relation:

$$U_r = c(d\Phi/dt)/4\pi f_{ADV},$$

where f_{ADV} is the ADV's operating frequency, c is the speed of sound, and $d\Phi/dt$ is the rate of change of the phase shift. The radial velocities are converted into orthogonal coordinates using a transformation matrix which depends on the angle between the transmitter and the receivers, and is obtained through a (manufacturer's) calibration of the ADV (Vectrino Velocimeter User Guide, 2004).

As a relatively new instrument, the ADV needs to be benchmarked in known flows to investigate its accuracy and sources of error. It has been found that the ADV accurately predicts the mean velocity and the Reynolds shear

stresses in bed shear dominated turbulence (*e.g.*, in rivers) (Voulgaris and Trowbridge, 1998; Hurther and Lemmin, 2008). However its accuracy in measuring turbulence quantities such as the normal components of the Reynolds stresses, turbulent kinetic energy, and the turbulent microscales has been questioned (Nikora and Goring, 1998; Voulgaris and Trowbridge, 1998; Cea *et al*., 2007; Hurther and Lemmin, 2008). Voulgaris and Trowbridge (1998) showed that (assuming the measured velocity in each beam consists of the true velocity and unbiased noise, $\langle u_i^2 \rangle = \langle u_{Ti}^2 \rangle + \sigma_i^2$, and the noise is identical for each beam, $\sigma_i = \sigma$) the quality of the variance ($\langle u_i^2 \rangle$ or u_{rms}^2) and the covariance ($\langle u_i u_j \rangle$) of the measured orthogonal velocities depends on the noise variance along each beam (σ^2) and the transformation matrix which is used to convert the velocities measured along the beams to orthogonal components. Based on the transformation, they showed that the noise contribution is $O(10^{-2}) \times \langle \sigma^2 \rangle$ to the covariance, $O(10^{-1}) \times \langle \sigma^2 \rangle$ to the variance of the vertical velocity and $O(10^{1}) \times \langle \sigma^2 \rangle$ to the variance of the horizontal velocities for a SONTEK ADV. (The direction of the horizontal and vertical velocities are shown in Figure 2.1.) Therefore, the effect of noise is more significant on the horizontal RMS velocities than on the vertical RMS velocity and the Reynolds shear stresses.

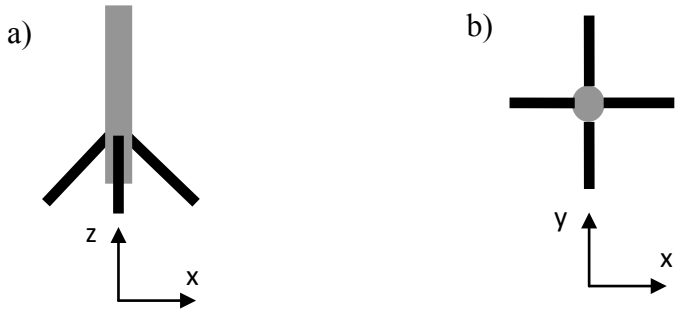

Figure 2.1 A Vectrino ADV probe with four receivers: a) side view, b) end view. Note that the velocity components in the x- and y- directions are referred to as horizontal velocities and the velocity component in the z-direction is referred to as the vertical velocity.

Voulgaris and Trowbridge (1998) divided the source of the noise into three categories:

(i) Sampling error related to the accuracy of the ADV's A/D board in resolving the changes in phase. This error is independent of the flow and depends on the pulse length, which is set by the velocity range.

(ii) Doppler noise, which is an intrinsic feature of all Doppler backscatter systems and is flow-related. This noise is due to (1) turbulence and particle scattering, (2) beam divergence, and (3) the finite residence time of the particles in the sampling volume.

(iii) Error due to mean velocity gradients in the sampling volume. This error becomes important in sharp velocity gradient flows such as boundary layers.

If there are enough acoustic targets in the sampling volume and the gradients of the mean velocities across the sampling volume are negligible, then the flow related contribution to noise is negligible. In this case, the most significant source of noise in ADV turbulence measurements is Doppler noise, which is inherent to the technique (Lohrmann *et al*., 1994). Doppler noise is a "white" noise, which does not influence the mean velocity. However it adds a positive bias to the high frequency range of the power spectrum, affecting the turbulence statistics (Dombroski and Crimaldi, 2007). Hurther and Lemmin (2001) characterized the Doppler noise as: i) having a flat spectrum over the frequency domain; ii) being unbiased ($<\sigma_i> = 0$), therefore not affecting the mean velocity; iii) being statistically independent of the true velocity fluctuations and true Doppler frequency; and iv) having statistically independent noise from one receiver to the next ($<\sigma_i\sigma_j> = 0$, $i \neq j$). (Furthermore, the relatively large sampling volume of the ADV can also limit its accuracy in turbulence measurements because smaller scales of a given flow may not be resolved by the ADV.)

To reduce the effect of Doppler noise, several post-processing filters have been proposed with the aim of improving the turbulence statistics measured by ADVs. These include the phase-space thresholding method of Goring and Nikora

(2002) and the despiking filters of Cea *et al*. (2007). In addition, Nikora and Goring (1998) presented a post-processing filter that removed Doppler noise from the ADV's measured velocities. To do so, they carried out velocity measurements with the ADV in a quiescent background and considered the signal measured therein as Doppler noise. Assuming the correlation between the velocity and the noise to be zero, they subtracted the measured noise from the measured velocity to estimate the true velocity. However, Lemmin and Lhermitte (1999) rejected this method remarking that the Doppler noise is an increasing function of the flow's mean velocity and velocity measurements in the quiescent background therefore do not predict the Doppler noise. Hurther and Lemmin (2001) presented a correction method for reducing the contribution of noise from the mean turbulence parameters. In this method, the normal Reynolds stress term can be estimated from the covariance of two quasi-instantaneous vertical velocities measured simultaneously in the same sampling volume, assuming that the noise signal is random and statistically independent. Therefore, the variance of the noise can be calculated (from vertical velocities) and removed from the variance of the horizontal velocity components based on the geometrical configuration of the probe, assuming that the receiver transducers are identical and ideal and, therefore, that the noise level is the same along each receiver beam ($<\sigma_i^2> = <\sigma^2>$).

2.4.2 Flying Hot-film Anemometry

Thermal anemometry is a well-established method for making turbulence measurements. Hot-film/wire sensors are electrically heated and infer the fluid velocity from the measured heat transfer from the sensor. Hot-film anemometry is usually used in liquid flows. Hot-films have sturdier construction compared to hot-wires (used in gas flows) and are electrically insulated. The hot-films are manufactured by depositing a thin layer of platinum or nickel ($\approx$ 0.1 μm) on thermally insulating substrates and coating it with a 1-2 μm thick deposited layer of insulating material (such as quartz). The impervious (quartz) coating offers

mechanical and chemical protection and also electrically insulates the hot-film. Hot-films come in different shapes and the most common are cylinders, wedges and cones. For cylindrical hot-films, the sensor diameter is about 25-70 μm and the length of the sensing element is 1-2 mm. The cold resistance of the hot-film varies between 5-15 Ω (Bruun, 1996).

Some of the advantages of hot-film anemometry include their: i) low cost, ii) high frequency response, iii) small measuring volume, iv) ability to measure velocity over a wide velocity range, v) high accuracy and signal-to-noise ratio (Bruun, 1996).

A hot-film probe is a part of a constant temperature anemometer circuit. A constant temperature anemometer uses a Wheatstone bridge and a high-gain differential amplifier in the feedback loop. When the hot-film sensor resistance changes (due to changes in its temperature due to heat transfer to the liquid), the amplifier in the feedback will sense the difference between the sensor and the reference resistance, and feed additional current to the top of the bridge to restore the sensor's resistance to its preset value (Bruun, 1995).

The non-dimensionalized heat transfer correlation for the hot-film probe is $Nu = A + BRe^n$, where Nu is the Nusselt number and A, B and n are constants. From this equation, a relation between the output voltage of the hot-film anemometry and the fluid velocity can be derived. The new equation is called King's Law: $E^2 = A + BU^n$, where E is the output voltage of the anemometer, U is the fluid velocity, and A, B and n are calibration constants. The value of n depends on probe type, method of calibration and the velocity range. For hot-films in water, in the velocity ranges of less than 20 cm/s n values are reported between 0.25-0.3, while for the velocities of 0.5-4 m/s the reported values of n evaluated are 0.4-0.45 (Bruun, 1995).

To obtain reliable measurements with hot-film anemometry, a few aspects should be considered. The formation of bubbles on the hot-film sensor can result in major calibration drifts. Therefore, the water should be allowed to stand so that

any dissolved gasses are released. Using a submerged return/filter water line in a water tank is also recommended instead of cascading in air. The bubble formation problem can be minimized by restricting the temperature difference between the water and the hot-film to 20 °C. The corresponding overheat ratio (ratio of the sensor's operating resistance to its cold resistance) is about 1.05-1.1 which depends on the film material (Bruun, 1995).

Temperature drift and contamination for hot-film probes should also be considered. These two often occur simultaneously and it is hard to separate their effects. The temperature difference between sensor and ambient fluid is about 20 °C for hot-film probes in water while this difference is about 250 °C for hot-wire probes in air. According to the response equation $E^2/R_{OP} = (A + BU^n)(T - T_a)$, where R_{OP} is the probe's operating resistance, T is the probe's temperature and T_a is the ambient flow temperature, a small change in water temperature results in a large shift in output voltage and therefore calibration of the hot-film. To minimize the problem: i) a large heat capacity e.g., a recirculation facility with a large storage tank can be used, or ii) a heating/cooling control system can be installed in the water tank to control the water temperature. However, frequent hot-film calibration is a more practical solution as it also accounts for the probe contamination. Probe fouling can occur due to build up of scale, algae, and minerals on the probe resulting in a drift in calibration and a loss of sensitivity. This problem can be minimized by using de-ionized water, a filtration unit and algaecide (Bruun, 1996).

Calibration is required for hot-film anemometry to find the relationship between the output voltage and the velocity of the liquid. Common calibration techniques include differential calibration and moving-probe calibration methods (Bruun, 1995). In the first method, pressure difference devices such as pitot tubes or calibration nozzles are used. Having the pressure difference, the velocity can be estimated using the Bernoulli equation, and the velocity can then be related to the anemometer voltage. In the moving-probe calibration, the probe is moved with a

constant velocity in stationary water. Moving the probe at various velocities, a relation between the velocity and voltage can be obtained.

Chapter 3

Experimental Setup

3.1 Experimental Facilities

The experiments investigated the effect of background turbulence on the dynamics and mixing of an axisymmetric turbulent jet by comparing the results of a jet released into a quiescent background with those of the jet issued into a turbulent background. The laboratory set up consisted of a jet mounted in a large water tank equipped with a random jet array to create the turbulent background. Traversing mechanisms were used to position the jet and to position and move the (velocity measurement) probe.

3.1.1 Water Tank

The experiments were conducted in a 1.5 m by 2.4 m by 0.9 m section of a (1.5 m by 6 m by 1 m) glass tank, filled with water and, open to the ambient air. It was located in the Environmental Hydraulics Laboratory of Civil Engineering and Applied Mechanics Department at McGill University. The tank consisted of a steel frame, glass walls and a glass bottom. The side walls were composed of

single panes of 1.905 cm thick tempered glass. The bottom consisted of two layers of 1.905 cm thick tempered glass panes, which had a total thickness of 3.81 cm.

3.1.2 Background Conditions

The tests were carried out in either i) a quiescent background, or ii) an approximately homogeneous, isotropic turbulent background with zero mean flow. The approximately homogeneous, isotropic, zero-mean-flow turbulence is generated by a random jet array (RJA) that is based on that of Variano *et al*. (2004) and Variano and Cowen (2008), but built to a larger scale in the 1.5 m by 2.4 m by 0.9 m section of the tank (Figure 3.1). Turbulence generated by an RJA creates a lower mean flow when compared to oscillating grid turbulence. The RJA consists of an array of 6×10 bilge pumps (Rule 25D, 500 GPH) mounted on a 1 m by 1.5 m vertical sheet of high density polyethylene (Figure 3.2.a). The pumps take in water radially at their base and discharge it axially from an outlet perpendicular to the plane of the RJA. As each pump's suction and discharge occur simultaneously, there is a zero net mass flow rate through a control volume surrounding the pumps (Variano and Cowen, 2008). An extension (0.15 m long) was attached to each pump to straighten the flow (Figure 3.2.b). The distance between the polyethylene sheet onto which the pumps were mounted and the exit of the extension was 0.24 m. The exit diameter of the jets of the RJA was 31.75 mm. The spacing of the pumps was uniform in the horizontal and vertical directions with a center to center distance (or mesh size, M) of 0.15 m. The reflectional symmetry condition with respect to the tank walls and free surface was employed (resulting in the spacing from the center of the jet outlets to the boundaries to be 0.075 m or 0.5M) to lessen the possibility of secondary circulations, in analogy with oscillating grid turbulence (Fernando and De Silva, 1993 and Variano *et al*., 2004 and Variano and Cowen, 2008). The RJA was operated by independently and randomly turning the pumps on and off. Downstream of the RJA, the jets merge, creating an approximately homogeneous isotropic turbulent flow with almost zero mean flow.

The jet array is controlled by LabVIEW. To find an optimum flow (in terms of low mean velocity, isotropy and homogeneity), two algorithms were tested in which each pump was independently and randomly turned on and off. In the first algorithm, the on and off times were determined from a normal distribution of adjustable mean and standard deviation (Variano and Cowen, 2008). A range of different average on times (μ_{on}), average off times (μ_{off}) and standard deviations (σ) for the first algorithm was tested optimize the RJA performance. The optimal parameters were found to be (μ_{on} , σ_{on}) = (12 , 4) s, and (μ_{off} , σ_{off}) = (108 , 36) s. On average, 10% of the pumps were on at a time. In the second algorithm, the state of a pump changed if a random number (between 0 and 1) that was generated every 0.4 seconds (for each pump) was greater than a certain threshold (0.98) (Mydlarski and Warhaft, 1996). Between these two algorithms, the flow produced using the first algorithm was superior, most notably because of its lower mean flow (at 110 cm downstream of the RJA, $\langle U \rangle / u_{rms} <$ 15% for the first algorithm, while $\langle U \rangle / u_{rms}$ was up to 50% for the second one). Therefore the first algorithm was used to control the RJA when a turbulent background was required.

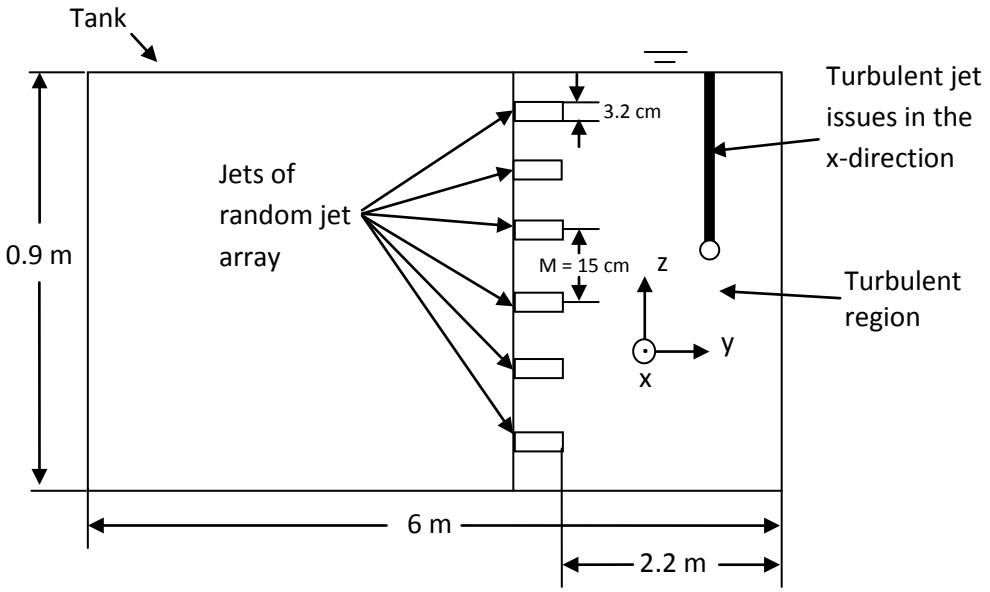

a) Side view

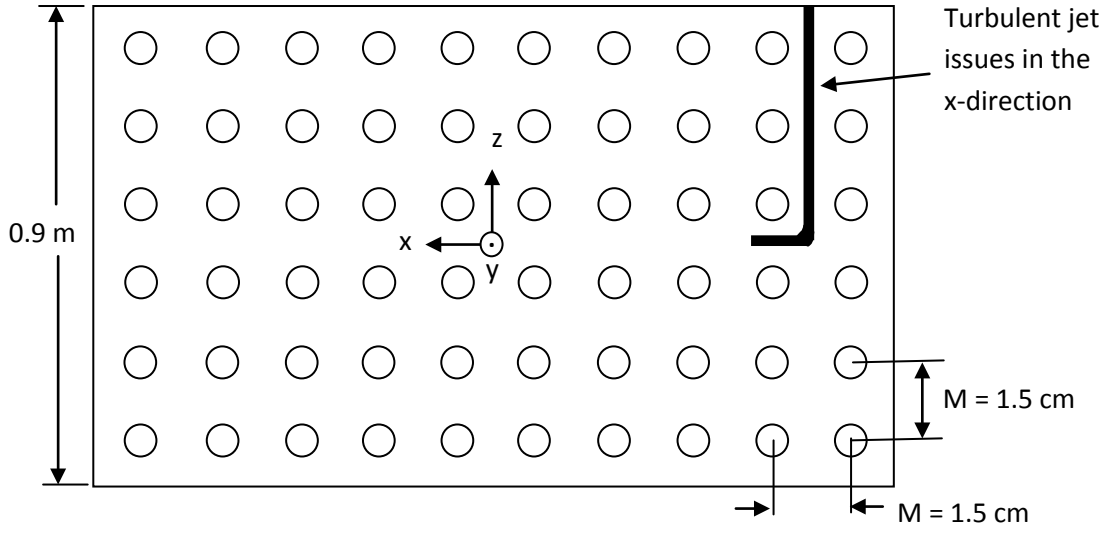

b) Front view

Figure 3.1 Schematic of the jet, the RJA and the tank. (a) side view. (b) front view. (Not to scale.)

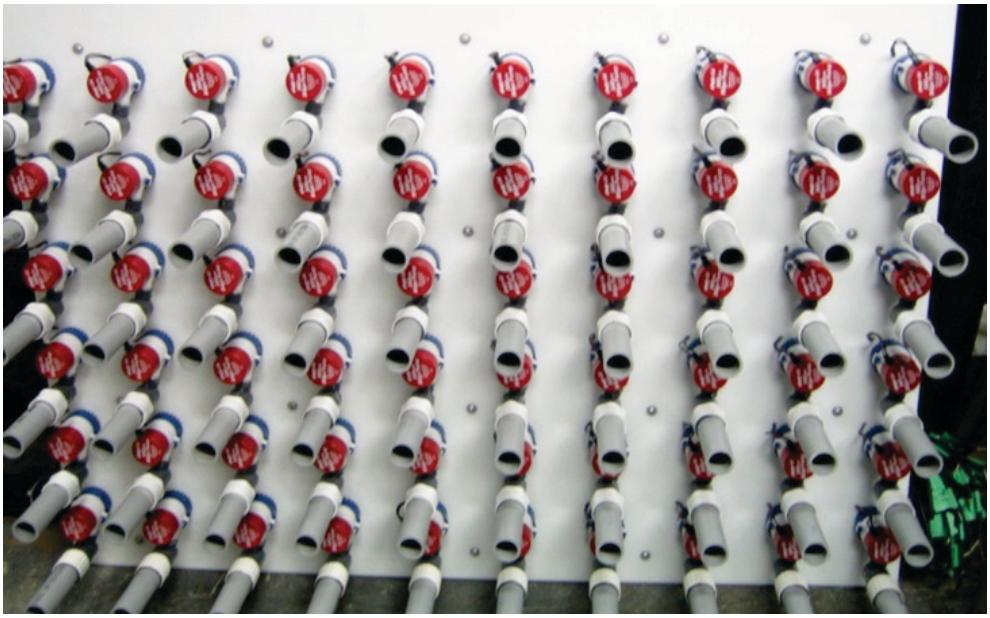

Figure 3.2.a The random jet array (RJA).

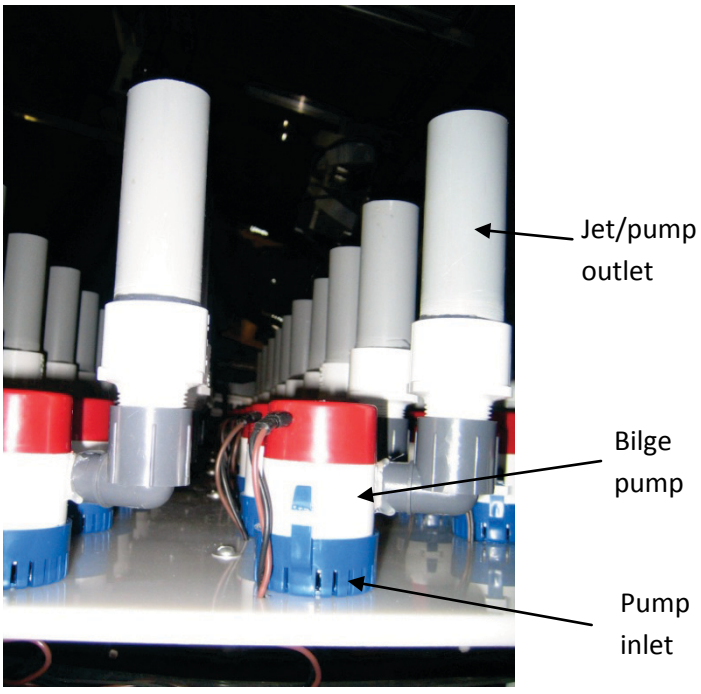

Figure 3.2.b A close-up of the RJA pumps.

3.1.3 Turbulent Jet Apparatus

The jet was mounted in the tank parallel to the plane of the RJA. It was supplied with water from a constant-head reservoir and several jet components controlled the flow. Traversing mechanisms were used to position the jet/probe precisely.

The constant-head reservoir was used as a (constant head) water supply to the jet to maintain a constant jet flow rate. It consisted of a (12 litre) spherical glass container located 2 m above the jet exit. Water was pumped (using a 1/3 hp Franklin Electric pump) continuously to an inlet at the top of the constant-head reservoir, while an overflow outlet at the top of the reservoir maintained the head (and therefore pressure difference) driving the jet. An outlet at the bottom of the reservoir directed water through plastic tubing, passing through a flow meter to the jet (made out of copper tubing) and finally into the tank as an axisymmetric jet.

The water supply to the constant-head reservoir was from different sources for the acoustic Doppler velocimetry and the flying hot-film anemometry measurement techniques. For the acoustic Doppler velocimetry measurements, neutrally buoyant glass particles were mixed with the water in the tank prior to an experiment to increase the signal to noise ratio. To avoid sending the particles to the flow meter, valves and the jet, the constant-head reservoir was supplied with clean water (instead of the tank water). A separate supply reservoir (a 35 litre cylindrical glass container) was continuously filled with clean water to pump the water to the constant-head reservoir. The excess water in the constant-head reservoir was sent back to the supply reservoir (Figure 3.3.a). To keep the water level in the tank constant, an overflow pipe was installed vertically in one of the drains (on the unused side) of the tank. The supply of water to the jet was simpler for the flying hot-film anemometry measurements (as no particles were needed in the tank water). In this case, the water for the constant-head reservoir was pumped

from the other side of the tank, behind the RJA. An overflow hose was sent back to the tank from the constant-head reservoir (Figure 3.3.b).

The water was transferred from the constant-head reservoir to the jet using several components. The bottom outlet of the constant-head reservoir was connected to 1.905 cm diameter PVC tubing which was later tapered to match the (1.27 cm) inlet diameter of the Omega FL50002A flow meter. The flow meter had an accuracy of 5%. The flow rate was varied between 2-4 litres/min, which corresponds to Reynolds numbers of 5,300-10,600 for an 8 mm diameter jet. A ball valve and a solenoid valve were used before and after the flow meter, respectively. The former controlled the flow rate, and the latter turned the flow on or off. The tubing was then tapered down to 8 mm to match the jet's tubing (copper pipe). The jet of circular cross section was mounted on a traversing mechanism and extended vertically for 1.6 m of which the lower 0.45 m was in the water. At 0.45 m below the water surface, a 90° bend caused the jet to extend horizontally for 0.12 m before its exit. At the exit of the pipe, the flow was fully-developed. The initial conditions at the jet exit might have an effect on the initial development region; however, the statistics in the self-similar region are not affected by the initial conditions (Ferdman *et al*., 2000 and Xu and Antonia, 2002).

The jet was positioned in the homogenous region of the background turbulence and two different levels of background turbulence were tested on the jet's evolution. The jet issued parallel to the plane of the RJA so that the turbulence generated by RJA was homogeneous along the axis of the jet. The jet was initially positioned at $y/M = 7.3$ ($y/M = 0$ is at the outlets of RJA), however, as will be shown in Figure 5.19a, the RMS velocity of the jet (at $Re = 10{,}600$) in the presence of background turbulence did not decay to the RMS velocity of background turbulence within the measurement range, and therefore, the jet was not fully destroyed. To investigate a more noticeable effect of background turbulence on the jet, the jet was also positioned at $y/M = 5.5$, which will be

shown in §5.2.1 to have maximum turbulent kinetic energy while remaining in the homogenous region of background turbulence.

For each jet experiment, the centerline of the jet was first determined. To start, the ADV or hot-film probe was visually aligned with the centerline of the jet. The radial profiles of the jet in the horizontal and vertical directions were then measured. The center of the jet was estimated by fitting a Gaussian distribution to the horizontal and vertical profiles, and the center was interpolated from the curve fit. On this basis, the probe was aligned again with the jet centerline. Subsequent radial measurements were carried out in small increments outwards from the centerline towards the edge of the jet.

Traversing mechanisms were required to move the jet and/or probe so that measurements could be carried out at several points in the radial and axial directions. During the ADV measurements, the jet was fixed and a Velmex traversing mechanism was used to precisely move the measurement apparatus horizontally and vertically along the jet radius (y- and z-directions) and also along the jet axis (x-direction). During the flying hot-film tests, the probe had to move at high velocities (up to 1.1 m/s). The position of the moving probe was also required. However, neither requirement could be achieved using the Velmex traversing mechanism. Therefore, the setup was changed for the flying hot-film experiments. In the new setup, the jet was mounted on the Velmex traversing mechanism and was moved along the y- and z-directions, while the probe only moved along the jet axis (x-direction) using a high-precision, Aerotech traversing mechanism that moved the probe at high speeds. (The Velmex and Aerotech traversing mechanisms will be explained in detail in sections 3.1.5 and 3.1.6, respectively.)

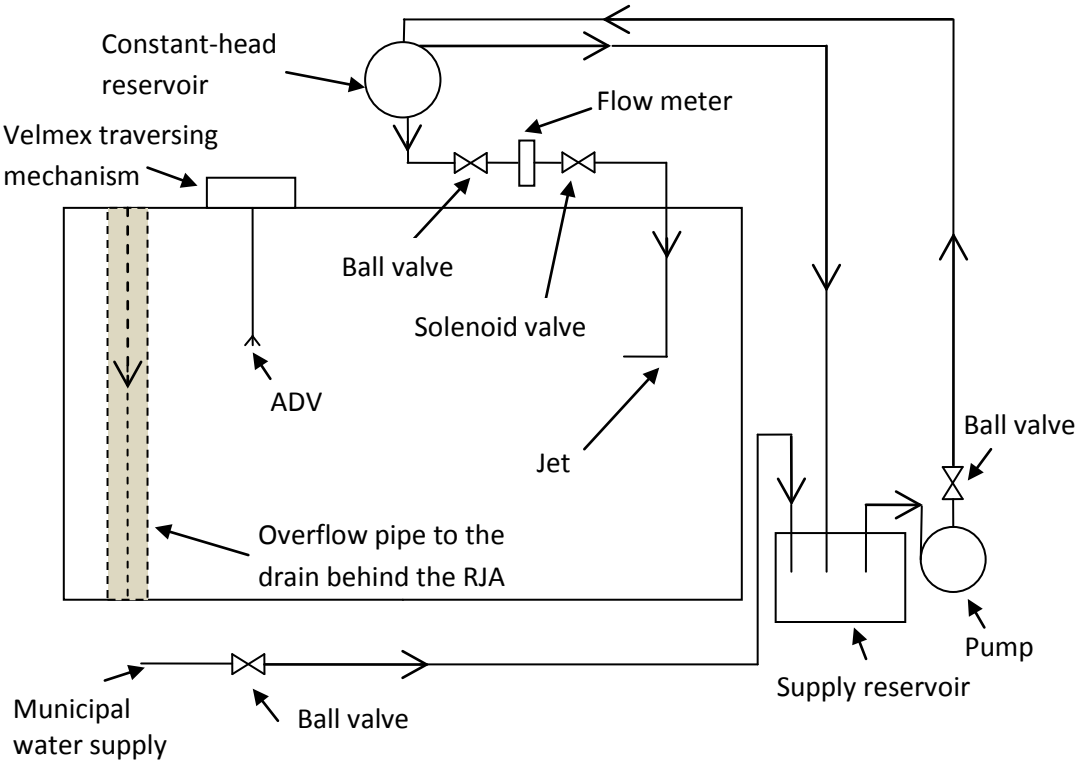

a) Jet setup for the ADV tests

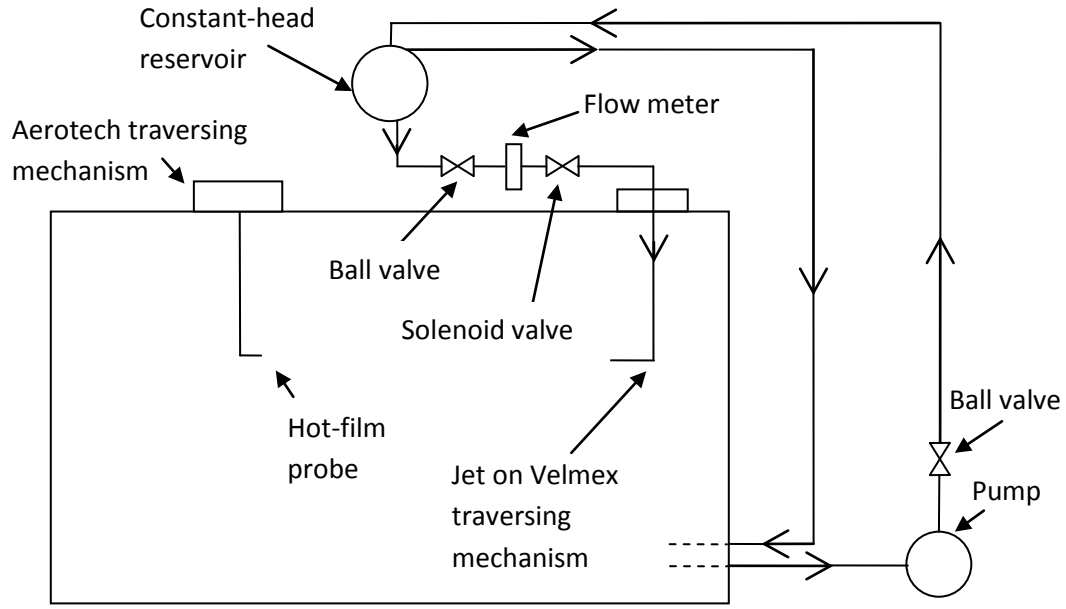

b) Jet setup for the flying hot-film tests

Figure 3.3 Jet setup for the a) ADV and b) flying hot-film tests. (Not to scale.)

3.1.4 Filters and Heater

The tank was filled with the water from the municipal water supply. For the ADV tests, filtering was not required as the ADV measurements required particles in the water. However, the hot-film anemometry measurements required clean water with a controlled water temperature. A Jacuzzi Laser Sand filter in series with a Hayward EC65A filter was used to filter the water upon entering the tank. Once the tank was full, the Hayward EC65A filter was used to continuously filter particles of size greater than 2 μm from the water in a recirculation loop (Figure 3.4). A 1 hp Club Piscine pool pump was used to circulate the water. The water was pumped from the outlets of the tank through the filter and then back to the inlets of the tank. Inlets and outlets were located at the bottom of the tank. Algaecide was also added to the water. The combination of filtration and algae inhibitor minimized the (hot-film) probe fouling during the flying hot-film experiments. The hot-film probe was also carefully cleaned with a fine brush and calibrated before and after each test. Furthermore, a heater consisting of a Chromalox heating element mounted in a stainless steel tube (located outside of the tank) was used to heat the water to room temperature. Two three-way valves were used to include the heater in the recirculation filtering loop. The heating element had a control box that was connected to a sensor inside the water. The desired temperature was set through the control panel. Once at room temperature, the water temperature did not change substantially (at most ±0.3 °C per 12 hour period). As mentioned earlier, the experiments were carried out in a 1.5 m by 2.4 m by 0.9 m section of the tank. The water in both sections of the tank was recirculated and filtered while the water was being warmed up. A pool broom connected to the pump was also used to clean the bottom of the tank. Before the start of an experiment, the valves to the experiment side of the tank were closed while the filtering was continued on the other section of the tank during a test. The water for the constant-head reservoir (which drove the jet) was taken from the non-experiment side of the tank. The temperature of the water was monitored and

recorded before and after each test using an Omega thermocouple that had an accuracy of ±0.1 °C.

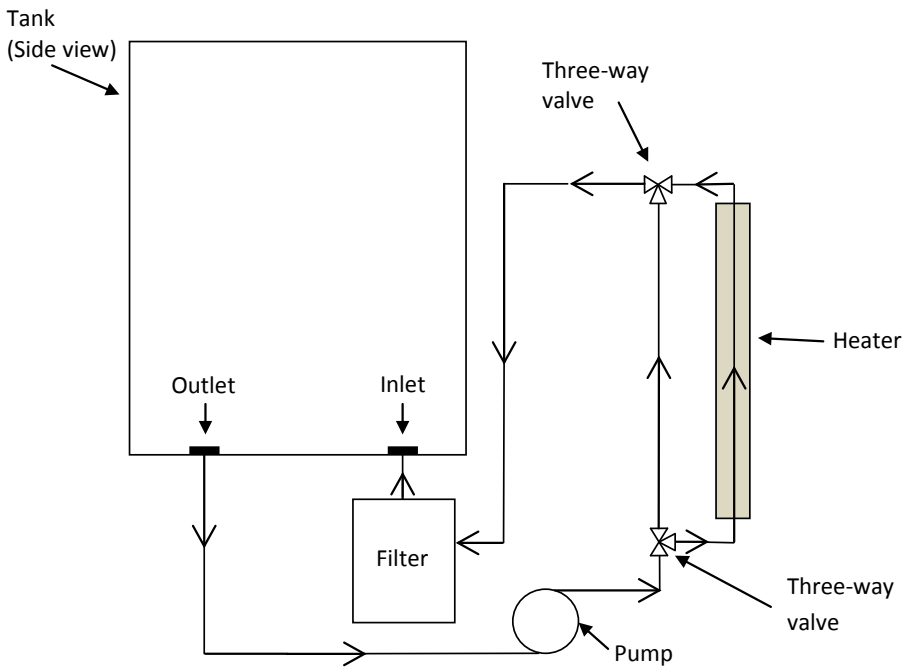

Figure 3.4 Recirculating filtration unit and the heater. (Not to scale.)

3.1.5 Acoustic Doppler velocimeter setup

The acoustic Doppler velocimeter was employed for velocity measurements in two sets of experiments. The first set of experiments was an attempt to benchmark the ADV and to relate the noise to the mean flow velocities, therefore increasing the accuracy of turbulence statistics measured by the ADV. In the second set, the velocity fields of the jet, the background turbulence, and the jet in background turbulence were measured.

The velocity field was measured by a Nortek Vectrino 10-MHz acoustic Doppler velocimeter. The ADV consists of a probe, a housing which contains the electronics, and a power and communication cable that connects the housing to a

serial port of a computer system. The Vectrino ADV probe was mounted on a cable connected to the main housing. The probe consisted of a central transmitter (which sent the acoustic pulses) surrounded by four receivers (which collected the signals reflected off the particles within the sampling volume). The housing contained the power transmitter, analogue-to-digital signal processor, power conditioner and the standard data recorder. The power and communication cable was used to supply the ADV with external DC power (12-48V) and was also used for 2-way serial communication between the ADV and an external computer. The accuracy of the velocity signal was 0.5% of the sampling range, selected to be ±10, ±30 or ±100 cm/s (depending on the flow being measured), which spanned the entire range of measured velocities. The sampling rate was set to 25 Hz (the maximum). The sampling volume of the ADV is located 5 cm below the probe and was set to its maximum volume of 0.26 cm^3 (which resulted in maximum signal-to-noise ratio). The 5 cm distance between the probe and sampling volume minimizes the flow interference by the probe. The power level of the ADV was also set to High to ensure maximum signal-to-noise ratio (SNR). The ADV was connected to a computer system from which the ADV parameters were set and the data were acquired through the Nortek Vectrino software.

As the ADV operates by measuring acoustic signals reflected off particles in the flow, neutrally buoyant glass particles (Potters Industries Sphericel hollow glass spheres) were added to the filtered water to increase the SNR of the ADV. The particle diameters were 9-13 μm. The specific gravity of the particles was 1.1. Once the tank was full, 20 g of particles were mixed with warm water in a container and were added to the tank's water. The concentration of particles was sufficient to keep the SNR high enough over a 12-hour period.

The particles may affect the flow. To determine their effect, the Stokes number (defined as the ratio of the response time of the particles to the characteristic time scale of the large-scale eddies) is calculated. If the Stokes number is sufficiently small ($St << 1$), the particles follow the fluid parcels closely and do not affect the velocity field (Raju and Meiburg, 1995). The

response time of a spherical particle is given by: $\tau_p = \rho_p d_p^2/18\mu$, where ρ_p is the density of particles (1100 kg/m^3), d_p is the diameter of particles (11 μm), and μ is the dynamic viscosity of water (Raju and Meiburg, 1995). Using this equation the response time of the particles is calculated to be 7.3×10^{-6} s. The characteristic time scale of the flow can be estimated from the integral time scale of the flow which can be obtained from the area under the temporal autocorrelation curve. The integral time scale of the jet during measurements was smallest at $x/D = 30$ (~ 0.03 s) and results in a Stokes number at the centerline of the jet at $x/D = 30$ of 2×10^{-4}. As St << 1, the large-scale velocity field is not expected to be affected by the particles. To verify this, two other types of particles ─ Nortek Company particles (8-13 μm and density of 1.1 g/cm^3) and Johnson's Baby Powder (specifications unknown) ─ which have been used by other researchers for the ADV velocity measurements were tested. However, the results showed that the velocity statistics were independent of the three different types of particles tested.

In the first set of experiments, to study the effect of mean flow on the ADV noise, the ADV was mounted on the Aerotech traversing mechanism (which could move the ADV at relatively high velocities). This was motivated by a discussion paper of Lemmin and Lhermitte (1999) which stated that the Doppler noise is a function of the flow's mean velocity. The traversing mechanism was positioned above the tank and parallel to the RJA to move the ADV at a constant speeds of 0-0.2 m/s. Measurements were made in: i) a quiescent background, ii) a quiescent background with the ADV moving at a constant speed (using the traversing mechanism), iii) homogeneous isotropic turbulence with no mean flow, and iv) homogeneous isotropic turbulence with an artificially generated mean velocity (by moving the ADV at a constant speed using the traversing mechanism).

In the second set of experiments, the measurements were made in: i) the background turbulence generated by the random jet array, which included homogeneity and decay tests, ii) an axisymmetric turbulent jet in quiescent background, and iii) an axisymmetric turbulent jet in a turbulent background. In

the second set of experiments, the ADV was mounted on the Velmex traversing mechanisms which was used to position the ADV vertically, horizontally and along the axis of the jet. The traversing mechanism was mounted on a C-channel which was located on top of the tank and parallel to the plane of the RJA and the axis of the jet. The Velmex traversing mechanism consisted of three Velmex BiSlide assemblies which moved the ADV in three directions and were controlled by a Velmex VXM-2 stepping motor controller. Each BiSlide assembly consisted of a motor which drove a lead screw, and therefore a carriage, on a track. Two limit switches were mounted on both ends of the track (for each Velmex BiSlide assembly) to avoid collisions between: i) the motor and the end walls of the track, and ii) the ADV probe and the tank side walls. The Velmex motor controller controlled by a LabVIEW program was used to move the traversing mechanism.

Before the start of each test, to increase the accuracy of the velocity measurements by the ADV, the velocity range was set and the quality of the data ensured by checking the signal to noise ratio (SNR) and correlation parameters. The velocity range of the ADV was set so that it spanned the entire range of measured velocities (based on the time series of the velocity observed using the Vectrino software). The minimum acceptable values of the SNR and correlation parameters specified by the manufacturer are 15 dB and 70%, respectively. If enough glass particles were mixed in the water, the SNR and the correlation would be high. In the background turbulence generated by the RJA, the SNR was greater than 20 dB and the correlation was 99% all the time. In the jet measurements, close to the jet exit ($x/D < 30$), the SNR and the correlation dropped significantly as the jet water did not contain particles. However, as the jet mixed and entrained ambient fluid (and therefore particles) farther downstream, the SNR and the correlation increased to higher than 20 dB and 70%, respectively. Therefore, jet measurements were only conducted at $x/D > 30$. In addition, the SNR and the correlation decreased significantly in the vicinity of the glass walls. Therefore, measurements close to the walls were avoided.

3.1.6 Flying hot-film anemometry setup

The flying hot-film was employed for velocity measurements of: i) the background turbulence generated by the random jet array, ii) an axisymmetric turbulent jet in a quiescent background, and iii) an axisymmetric turbulent jet in a turbulent background.

The presence of (and knowledge of the direction of) the mean velocity is required for stationary hot-film anemometry measurements, as the hot-film measures the heat transfer which is a scalar and does not account for the flow direction. When the mean flow is small compared to magnitude of the turbulent fluctuations, or when reversing flows are known to be present, hot-film measurements are not accurate. In our experiments this was true i) at the edges of the jet in quiescent background experiments, ii) in the random jet array flow, and, iii) in the jet in the presence of background turbulence. Therefore, the probe was moved at a constant speed using a traversing mechanism designed and built for this purpose to induce an artificial mean flow. The velocity of the traversing mechanism was chosen so that $u_{rms}/\langle U \rangle < 0.2$ - an upper limit for the applicability of Taylor's frozen flow hypothesis. This artificial mean velocity was later subtracted from the measured velocity data.

The flying hot-film anemometry setup consisted of a TSI 1210-20W hot-film sensor connected to a DISA 55M10 anemometer for velocity measurements, a Krohn-Hite filter (Model 3382) for the low-pass filtering of the data, an Aerotech high-precision linear traversing mechanism (which was used for moving the flying hot-film in the water), and a data acquisition unit (for use with the traversing mechanism) for recording velocity and position data simultaneously.

The Aerotech traversing mechanism consisted of a carriage (on which the hot-film probe was attached) running along a monorail and driven by a linear motor guided by a magnet track parallel to the monorail. The linear motor and the carriage (with a built-in encoder) had to be integrated for two reasons: i) the motor provided the driving force in the direction of movement (including the

friction of the carriage, the drag on the probe and probe holding rod, and the inertial force to accelerate and decelerate the assembly), while the carriage bore the normal load (due to the weight of the components connected to the carriage), and ii) the control system required the position feedback signal from the encoder integrated in the carriage.

The traversing mechanism was controlled by an Aerotech SOLOIST CP10 controller. The controller drove the linear motor which was attached to the carriage which bore the normal load of the measurement assembly. The carriage, which ran along the monorail (described below), had an integrated encoder which read the position data from the measuring strip integrated on the monorail and sent it back to the feedback of the controller. The position data was also sent to the data acquisition card.

The motor was an Aerotech BLMUC-143-A linear DC motor (Figure 3.5.a) which consisted of a moving forcer coil assembly (with Hall-effect devices) which drove the carriage (and therefore the hot-film probe) by providing horizontal force along a "U-channel" magnet track which provided a magnetic field for the forcer and guided the forcer along a line parallel to the monorail. A thermal sensor stopped the forcer in case of over overheating. The forcer coil assembly was a compact, reinforced ceramic epoxy structure and moved in the "U-channel" magnet track without contacting the channel (Figure 3.5.b). The non-contact forcer eliminated wear problems and maintenance. The "U-channel" magnet track consisted of 3 MTUC416 tracks in series with 52.0 mm x 20.8 mm cross section and 1248 mm in length in total. The motor could provide a continuous force of 39.8 N with no air supply. This force was increased to 58.0 N during the experiments by connecting a compressed air supply of 20 psi to the motor. The force was applied in the direction of movement and the motor thus did not bear normal loads.

The carriage with an integrated encoder driven along the monorail (by the Aerotech linear motor attached to the carriage) was an integrated linear distance measuring system which served to provide the position feedback of the (Aerotech

SOLOIST CP10) controller as well as to bear the normal load of the measurement assembly. This system was a Schneeberger Monorail AMSD-4A (Figure 3.6) which consisted of the linear bearing carriage to bear the normal load with an integrated differential digital encoder to read the position, and a monorail (parallel to "U-channel" magnet track) on which the carriage was traversed. The encoder sent the position feedback signal to the controller and the control system did not work without the encoder signal. To determine the absolute position of the carriage, there was a measuring strip fully integrated on the monorail which contained a fine incremental track with alternate N and S poles spaced at 200 μm intervals, and reference marks spaced at 20 mm. A relative movement between the encoder sensor on the carriage and the measuring scale changed the field strength which resulted in measurable change in electrical resistance. The resolution of the encoder was 1 μm. Occasional lubrication was required for the linear bearing in the carriage. Therefore, a grease nipple was installed in front of the carriage and grease was fed into the bearing while the carriage was moved slowly.

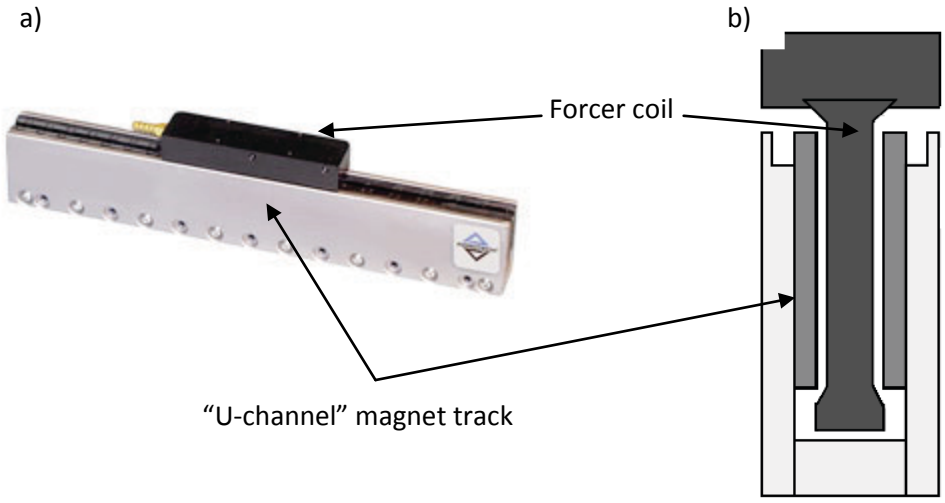

Figure 3.5 a) Aerotech BLMUC-143-A linear DC motor, b) Magnet track and forcer coil end view.

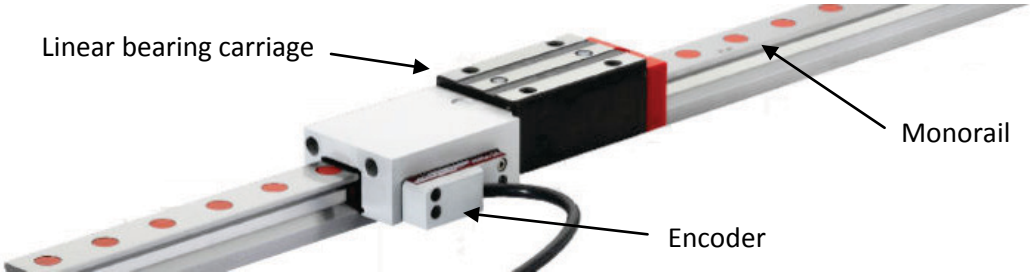

Figure 3.6 Schneeberger Monorail AMSD-4A.

The linear motor and the monorail were connected with a short length of aluminum C-channel connecting the forcer coil and the carriage together (Figure 3.7 and Figure 3.8.b) as it was screwed across the top of both components. Holes were drilled in it to make it lighter and reduce the load on the motor.

The magnet track and the monorail were mounted on an aluminum C-channel in parallel (Figure 3.7). The Velmex traversing mechanism that moved the jet in the new setup (instead of the ADV) was mounted on another C-channel. These two C-channels were parallel and spanned the tank width. They were fixed perpendicularly on top of two smaller vertical C-channels to which wheels were installed (Figure 3.7 and Figure 3.8). The assembly could then roll along the tank along the two guide rails installed on top of the longer sides of the tank. The traversing mechanisms were positioned on these two rails so that they were parallel to the plane of the RJA and could be moved manually along the tank and be positioned at a desired location downstream of the RJA without changing the relative position of the jet and the probe. Two limit switches were connected to both ends of the Aerotech traversing mechanism to avoid collisions of the probe with tank side walls.

The probe was attached to the traversing mechanism via a rod which was fixed to the same short length of aluminum C-channel which connected the forcer coil and the carriage together. The (probe holder) rod consisted of a 110 cm stainless steel circular cylinder rod of which the bottom 45 cm extended vertically into the water. To decrease the drag and to also reduce probe oscillations induced from vortex shedding, the bottom part of the probe holder rod was slid into a 45

cm stainless steel cylinder of an airfoil cross-section (length = 50 mm, width = 22 mm). Therefore, only the bottom 45 cm of the probe rod which had an airfoil cross-section was located in the water. The probe rod was in the middle of two C-channels which held the traversing mechanisms of the jet and the hot-film probe. To increase the rigidity of the probe holder, three long screws were threaded from the aluminum C-channel to a nut around the circular cylinder (Figure 3.8.a). To attach the probe to the rod, a hole was made in the front side of the airfoil bottom. A rod of circular cross-section of an internal diameter close to the external diameter of the probe (8 mm) was threaded horizontally at a 90° angle into this hole. The probe was later slid into the rod and was fixed in place. The distance between the sensor's tip to the rod of airfoil cross section was 18 cm. The probe cable was passed through the circular cylindrical rod.

An Igus plastic cable track was used to carry and protect the cables (Figure 3.8.b). It was fixed to the short length of aluminum C-channel (which joined the forcer coil and the carriage) and was moved with the carriage. The motor control signal cable, the motor power cable, the air line for cooling the motor, the encoder signal cable, and the hot-film probe cable were passed though the cable track. The motor power cable was directly connected to the controller. The motor control signal cable, the encoder signal cable and limit switches cables were connected to a terminal block which was connected to the feedback of the controller. The controller was connected to the USB port of a computer. The probe cable was connected to the input of the anemometer.

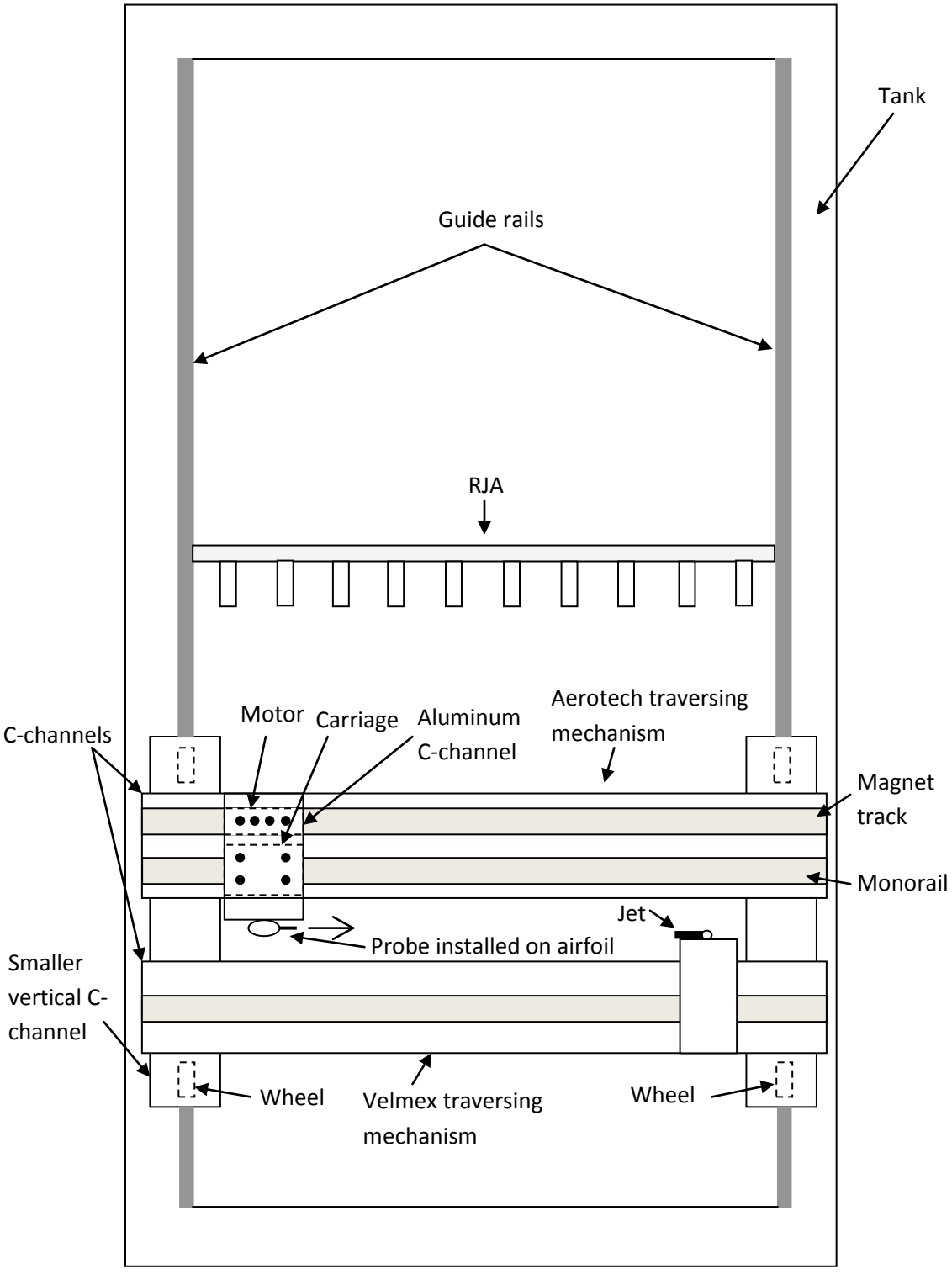

Figure 3.7 Top view schematic of the Velmex and Aerotech traversing mechanisms above the tank. (Not to scale.)

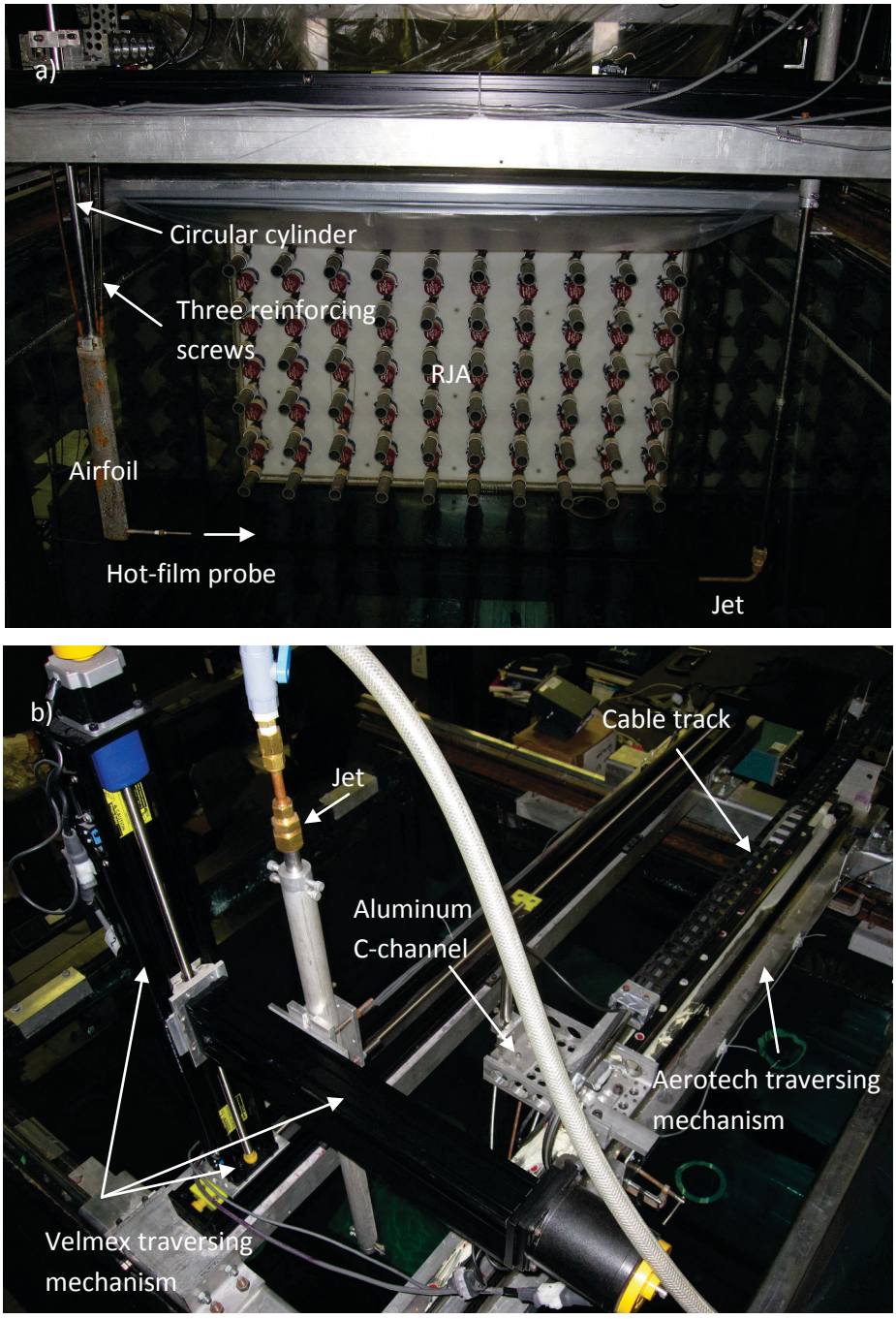

Figure 3.8 Views of the traversing mechanisms: a) side view, jet and probe, b) view from above.

The linear motor needed to be tuned before the start up of the system using an Aerotech software called the Soloist Digital Scope. The servo loop gains were set and the velocity, the velocity command, the velocity error, and the position error could be plotted in this software. Various gains were tested (by trial and error) to reduce the errors. By setting the proper servo loop gains, the position and velocity errors were minimized and the oscillation and the noise of the system were reduced.

The SOLOIST CP10 controller parameters such as acceleration, deceleration, velocity error, and position error threshold had to be set by the Soloist Configuration Manager software. This software had various sections including motor configuration, feedback configuration, motion configuration, fault handling etc. The 88 cm range of movement of the hot-film probe was limited by the tank walls and the jet. Due to this limited range of motion, maximum possible acceleration and deceleration rates were desirable; however the high values of acceleration at high velocities induced oscillations of the probe at the start of the movement. Therefore, for the measurements in the jet, the minimum acceleration and deceleration rates which allowed the probe to reach a constant speed over the desired measurement distance along the jet axis (which was from $x/D = 10$ to $x/D = 115$, where x was the downstream distance from the jet exit and D was the exit diameter of the jet nozzle) were chosen. The acceleration and deceleration were: 1 m/s^2 for measurements of the jet in a quiescent background and for measurements of the background turbulence generated by the RJA, 1.5 m/s^2 for the jet in the presence of background turbulence, and, 7 m/s^2 for the calibration tests. As the traversing mechanism speed was as large as 1.1 m/s in calibration tests, a high acceleration and deceleration rate of 7 m/s^2 was required to have a constant velocity range in each traverse. High acceleration at high speeds resulted in noticeable oscillations in the time series. Therefore, only the fraction of constant velocity range where the oscillations were damped was used in the calibrations. In addition, in such calibration cases, more than one pass was conducted to have enough data for convergence of the mean velocity.

The electronics inside the DISA anemometer and the Krohn-Hite filter of the hot-film anemometer were warmed up before the start of data acquisition by being turned on at least two hours before start of each test. The low-pass frequency of the filter was set to half the sampling frequency based on the Nyquist criterion. At the start of an experiment the anemometer needs to be set up. The anemometer was a constant temperature (or resistance) anemometer. For velocity measurements using hot-film anemometry, the temperature (or resistance) of the sensor should be higher than the ambient temperature (or sensor's resistance at the ambient temperature) to make velocity measurements possible. Hence, first the (cold) resistance of the sensor at the ambient temperature is found (R_{Cold}). Then the operating resistance (R_{op}) is calculated by applying an overheat ratio (OHR) to the cold resistance, *i.e.*, $R_{op} = R_{Cold} \times$ OHR. To find the resistance of the sensor, the cable resistance and internal resistance of the probe (provided by the manufacturer) should be subtracted from the sensor's measured resistance. The cable resistance of the anemometer was found by shorting the probe support before filling the tank. Then the hot-film sensor was mounted on the probe support and the tank was filled. After the water was warmed up to the room temperature using the heater, the resistance of the probe was measured at the temperature at which the experiments were conducted. The cable resistance and internal resistance of the probe were subtracted from the probe resistance to find the cold resistance of the hot-film sensor. An overheat ratio of 1.035-1.04 was applied to the cold resistance to get the operating resistance of the probe. Higher overheat ratios could not be used as they increased the voltage of the anemometer (at the highest velocities in an experiment, *e.g.*, probe moving at the jet centerline) to higher than 10 V which was the maximum input voltage of the data acquisition card. After setting the overheat ratio, the experiments were started.

During the hot-film experiments, when the motor was turned on, the noise at the high frequency end of the voltage (*i.e.*, velocity) spectrum increased. This was due to electromagnetic noise generated by the motor or the amplifier located in the SOLOIST CP10 controller. To decrease the noise, different solutions were

attempted. Ferrite beads (FBF-1) were installed on the power line of the motor, as was suggested by Aerotech. A Faraday Cage (an enclosure) was also made out of aluminum screen around the controller to contain potential noise from the amplifier located in the controller. These two solutions did not significantly reduce the noise on the spectrum. The traversing mechanism was then connected to the water tank using a wire to ground the system. Grounding the system reduced the noise by approximately half a decade in the spectrum (Figure 3.9). This electronic noise is not expected to affect the large-scale quantities measured in this study, as they are determined by the large (low-frequency) scales in the spectrum which are not significantly affected by the noise.

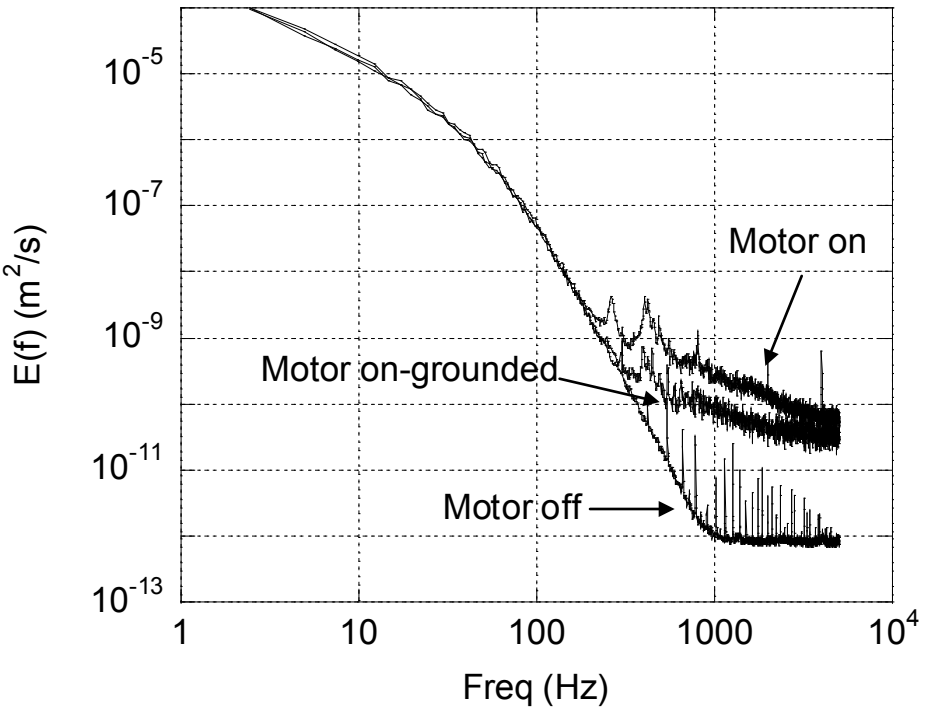

Figure 3.9 The effect of motor noise and grounding of the traversing mechanism on the spectrum of the jet in a quiescent background at $x/D = 30$.

3.2 Data Acquisition and Post Processing Programs

3.2.1 ADV Data Acquisition and Post-Processing Programs

The output data file of the ADV included velocity, signal to noise ratio, and correlation for each velocity component. The convergence of the data was checked and the number of data required for convergence was determined for each test. The length of each data block was 4096 samples. 25 blocks of data were recorded for measurements of the jet in a quiescent background, and 50 blocks of data were collected for measurements of the background turbulence and measurements of jet in the turbulent background. The data were acquired at frequency of 25 Hz which was the maximum sampling frequency of the ADV. Using a FORTRAN program, the data were analysed and their statistics were calculated.

During the experiments in which the ADV moved at a constant speed using the Aerotech traversing mechanism, the ADV continuously recorded data. The data was recorded (at frequency of 25 Hz) for 400 passes for the case in which the RJA was on, and for 100 passes for the quiescent case. A delay between passes was required so that the flow disturbance induced by the probe and probe holder disappeared. There was a delay of 35 s and 40 s between passes for quiescent and background turbulence cases, respectively. The output ADV data included constant velocity parts, corresponding to the ADV moving at a constant speed, and an approximately zero velocity part, which corresponds to the (delay) time when the ADV was not moving. For the data analysis, all constant velocity parts were first saved in a new file. Then the statistics of the data in the new file was calculated using a FORTRAN program.

3.2.2 Flying Hot-Film Data Acquisition Components and Programs

A field-programmable gate array (FPGA) card was used to collect data at a deterministic rate, with no delay and independent of the Windows operating system. This FPGA card (located in the computer) simultaneously collected the voltage and position data from the data acquisition modules via an expansion chassis which acted as a converter. The voltage data from the flying hot film anemometer and position data from the encoder were obtained with the National Instrument C-series data acquisition modules (located outside the computer). The analogue voltage output signal of the anemometer was converted to a digital signal by an analogue to digital, ±10 V, 16-bit, NI 9215 data acquisition module. The differential digital signal of the encoder was taken from the terminal block and sent to a differential digital input module (NI 9411). A CompactRIO R series expansion chassis (cRIO-9151) which housed the voltage module (NI 9215) and the position module (NI 9411) allowed using C-series module with the FPGA card. An R-series multifunction FPGA card (NI PCI-7830R) was programmed to simultaneously acquire both the voltage and the position from the expansion chassis.

LabVIEW FPGA programs ("virtual instruments") were developed in LabVIEW 8.2.1 for i) calibration, and, ii) controlling the data acquisition and the motion of the traversing mechanism during the experiments. Both programs had similar algorithms. Each program consisted of a main program ("Host") which controlled the motion of the traversing mechanism and also acquired data from an FPGA virtual instrument. In the FPGA virtual instrument, the voltage of the anemometer and the digital signal of the encoder were each acquired at the maximum sampling rate of 100 kS/s and 2 MS/s, respectively. The encoder's differential digital signals were also converted to position in the FPGA virtual instrument. Although the samples were acquired at different rates for the encoder and anemometer in the FPGA virtual instrument, they were acquired

instantaneously in the "Host" program with a sampling frequency of 1 kHz from the FPGA program — the maximum allowable sampling frequency in the "Host" program. To start all the passes of the motor from the same reference location, in the "Host" program, a command was first sent to the motor to move to "Home" which was a reference location where each pass started. The move command was then sent to the controller (by the "Host" program) and the data acquisition started at the same time. Data was acquired when the probe was moved towards the jet (the direction in which the probe was pointing), that is from downstream to upstream in the jet. The voltage from the anemometer and its corresponding position were saved in an output file.

Noise mostly affects the smallest eddies (which occur at the highest frequencies). Low-pass filtering was used to remove all the frequencies higher than the maximum frequency in the (turbulent) flow. To filter out high-frequency noise, a Krohn-Hite filter (Model 3382) was used for low-pass filtering of the output voltage of the hot-film anemometer measured in the background turbulence (generated by the RJA). The filter was connected to the data acquisition card, which sampled the data at the Nyquist frequency. According to the Nyquist sampling theorem, the sampling frequency should be twice the maximum frequency of the signal. Therefore, the low-pass frequency of the filter was set to 500 Hz as the sampling frequency was 1 kHz.

To covert the voltages to velocities, a relationship between the output voltage of the hot-film anemometer and the fluid velocity was required. The calibration tests were used to determine this relationship which is in the form of an equation called King's Law: $E^2 = A + BU^n$, where E is the output voltage of the anemometer, U is the fluid velocity, and A, B and n are calibration constants. Common calibration techniques include differential calibration and moving-probe calibration methods. In the first method, the pressure difference devices such as pitot tubes or calibration nozzles are used to estimate the velocity using the Bernoulli equation, and the velocity can then be related to the anemometer voltage. In the moving-probe calibration, the probe is moved with a constant

velocity in stationary water. A relation between the velocity and voltage can be obtained by moving the probe in a range of velocities. The latter method was employed here as the Aerotech traversing mechanism developed for flying hot-film tests could be used for a moving-probe calibration.

The drift in the hot-film's calibration was minimized by continuously filtering the water, using an algae inhibitor, and warming up the water to the room temperature prior to the calibration. Nevertheless, probe fouling and temperature change were two of the most significant sources of error during the flying hot-film experiments. It is also hard to estimate the separate contribution of each error. To minimize their effect, two calibrations, one immediately before and one immediately after each test were conducted. If any significant shift in the calibration (due to the water temperature change and/or probe contamination) was observed, the test was repeated. Otherwise the average voltage of two calibrations was used to determine the calibration constants. The uncertainty due to calibration shift will be discussed in the Appendix A.

To compare the electrical and mechanical noise on the spectra, the hot-film was moved at increasing velocities in a quiescent background. Figure 3.10 shows that the noise decreased as the velocity decreased. Therefore, the probe was moved at the lowest velocity possible, which was limited by the lowest allowable turbulence intensity ($u_{rms}/\langle U \rangle < 0.2$ - an upper limit for the applicability of Taylor's frozen flow hypothesis (Tennekes and Lumley, 1972)) of the flow. In the calibration to determine the relationship between the voltage and the velocity, the probe was moved at velocities ranging from 0.01 m/s to 1.1 m/s. For all other experiments, the probe was moved at a constant velocity of 0.1-0.3 m/s.

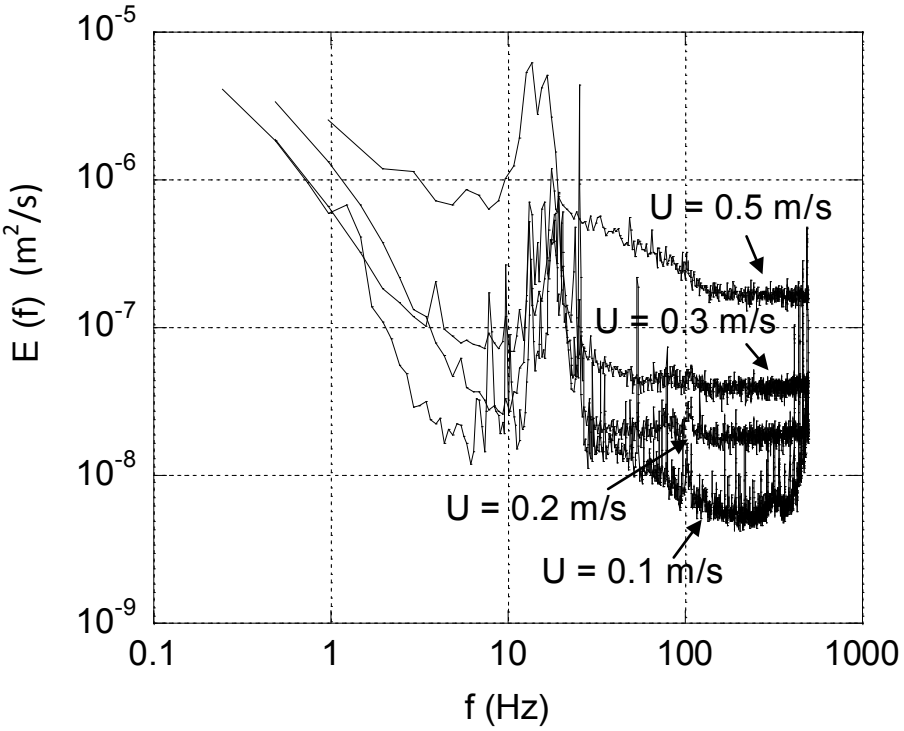

Figure 3.10 Noise spectra for various flying hot-film velocities measured in a quiescent background.

The flow disturbance caused by the movement of the airfoil and the hot-film probe was allowed to decay by having a "waiting time" between passes. This "waiting time" changed depending on the velocity of the traversing mechanism. The higher the velocity, the higher the disturbance. For the calibration tests, this time varied from 28 s for 0.01 m/s to 88 s for 1.1 m/s. The experiments of the jet in a quiescent background had a traverse velocity and "waiting time" of 0.1 m/s and 10 s, respectively; for the background turbulence generated by the RJA these were 0.1 m/s and 30 s; and for the jet in the presence of background turbulence these were 0.3 m/s and 20 s. These waiting times were determined by separate tests to find the time required for the disturbance to damp.

3.2.2.1 Flying Hot-Film Post-Processing Programs

Analysis of the output data of the flying hot-film system was performed using post-processing FORTRAN programs developed in-house. The output data

consisted of both encoder position and anemometer output voltage. In each probe traverse there was an acceleration phase, a constant velocity phase and a deceleration phase. The acceleration phase was accompanied by oscillations of the probe. Therefore, only the section of the data in the constant velocity range where the oscillations were damped was used in the analysis.

In the calibration program used to determine the constants for the King's Law curve fit relating voltage to velocity, the average voltage (E) corresponding to the constant velocity range was calculated for each probe velocity (U). Then the average of the E^2 found from the calibrations before and after an experiment was calculated for each velocity. At the next step, the averaged E^2 was plotted versus U and the King's Law curve fit was used to find the calibration constants. A typical result is given in Figure 3.11. The value of n was mostly between 0.35-0.4. According to Bruun (1995), for hot-film sensors, in velocity ranges of less than 20 cm/s, n values are reported between 0.25-0.3, while for the velocities of 0.5-4 m/s the values of n evaluated were 0.4-0.45.

A program was developed to analyse the background turbulence data. As the turbulence generated by the random jet array was approximately homogeneous, the voltage corresponding to the constant velocity range for each pass was deemed a block of data. All the voltage data blocks were saved in one file using a FORTRAN program. Later, using the calibration constants in another FORTRAN program, the statistics such as moments and spectra were calculated.

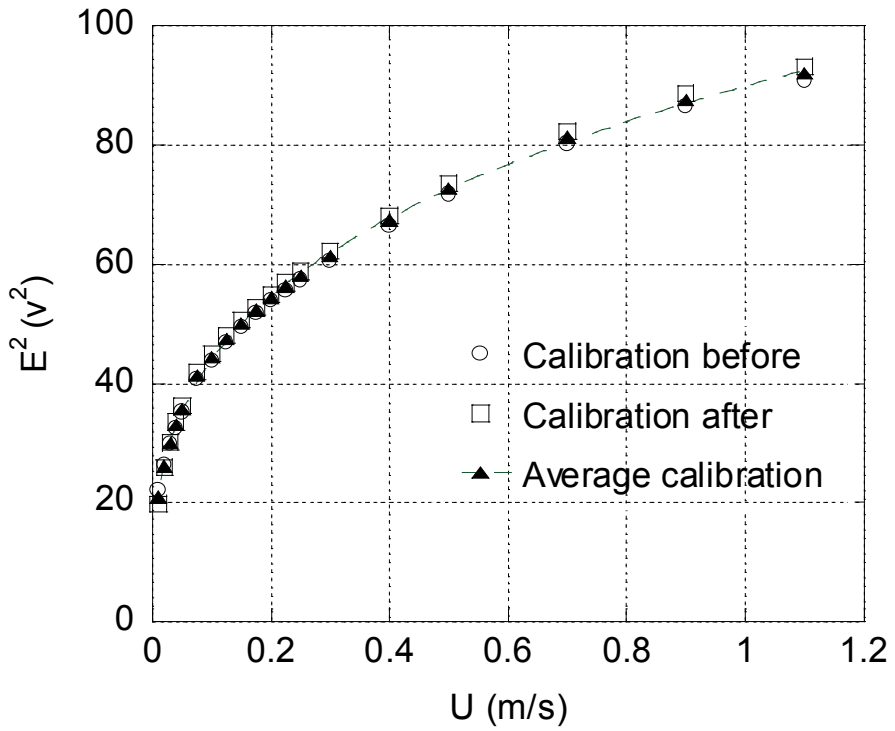

Figure 3.11 Sample average calibration curve calculated based on calibration tests conducted before and after each experiment.

The data acquired from the jet measurements in the quiescent and turbulent backgrounds were analysed in another program. The output voltages were available at intervals of 1 μm along the jet axis from x/D = 10 to x/D = 115 (x was the distance downstream of the jet, and D was the exit diameter of the jet nozzle). There was only one output voltage data corresponding to each x/D for each pass of the traversing mechanism. Therefore, the number of data points for each x/D was the same as the number of the passes of the traversing mechanism during an experiment. To analyse the data, first, all the voltages corresponding to each x/D was stored in a separate output file. Then in another program, the statistics of all the files corresponding to various x/Ds downstream of the jet were calculated using the calibration constants.

Tests were conducted prior to the experiments to determine the number passes required for statistical convergence of the data. The results showed that the number of passes required for the statistical convergence of the data measured in

the jet in quiescent, background turbulence generated by the RJA, and the jet in the presence of background turbulence were 1000, 300, and 1200, respectively.

Chapter 4

Validation of Flow Measurements

Experimental results pertaining to the benchmarking of the acoustic Doppler velocimeter and the flying hot-film anemometry apparatus are presented in this chapter.

The measurements were conducted in an axisymmetric turbulent jet issuing into a quiescent background. The jet's Reynolds number was 10,600 — chosen to be above the mixing transition (Dimotakis, 2000).

Axisymmetric turbulent jets have been experimentally studied by Ricou & Spalding (1961), Wygnanski and Fiedler (1969), Panchapakesan and Lumley (1993) and Hussein et al. (1994) and more recently by Webster et al. (2001), Fukushima (2002) and Ying et al. (2004). Here the axial and radial variations of mean velocities, spreading rate, entrainment rate, and RMS velocities of the axisymmetric turbulent jet issuing into a quiescent background measured by both the ADV and the flying hot-film anemometer are compared with the results of more established works of Ricou & Spalding (1961), Wygnanski and Fiedler (1969), Panchapakesan and Lumley (1993) and Hussein et al. (1994). The results will also be compared with measurements by stationary hot-film anemometry

along the centerline of the jet. Note that radial profiles (and therefore the spreading rate) cannot be accurately measured using stationary hot-film anemometry because of the large turbulence intensities (and therefore flow reversals) at the edges of the jet.

4.1 Mean Velocity Statistics

Figure 4.1 shows the downstream evolution of the mean axial centerline velocity ($U_J/\langle U_{CL}\rangle$, where U_J is the nozzle exit velocity) of the turbulent jet (Re = 10,600) plotted as a function of x/D (where D is the exit diameter of the nozzle). The stationary and flying hot-film anemometer, and ADV data are presented and compared with the data of Wygnanski and Fiedler (1969), Panchapakesan and Lumley (1993) and Hussein et al. (1994). For clarity's sake, only the best linear fit was given for the data of Panchapakesan and Lumley (1993). As theoretically predicted, the inverse of the mean velocity varies linearly with the downstream distance in the self-similar region, i.e., $\langle U_{CL}(x)\rangle / U_J = D \times B / (x - x_0)$, where x_0 is the virtual origin and B is a constant. Using a linear least-squares fit to the above equation with the same virtual origin as Hussein *et al.* (1994) (x_0/D = 4), decay constants (B) of 5.9, 5.9 and 5.7, were obtained for the stationary hot-film ($30 \leq x/D \leq 90$), flying hot-film ($15 \leq x/D \leq 90$) and ADV ($30 \leq x/D \leq 75$) data, respectively. The decay constant is compared to that of the other measurements in Table 4.1. A comparison shows that this quantity is approximately independent of the Reynolds number. However, because the value of the decay constant is sensitive to the virtual origin, for the present work, B was calculated using the virtual origins of i) Panchapakesan and Lumley (1993) (x_0/D = 0), ii) Hussein et al. (1994) (x_0/D = 4), and iii) the value obtained using a simultaneous least-square fit of both B and x_0 to the present data. As it can be seen in the table, the measurements of stationary hot-film anemometer, flying hot-film anemometer and ADV are consistent with those of the other studies. This confirms the accuracy of both acoustic Doppler velocimetry and flying hot-film anemometry for mean flow measurement (at least up to $x/D \approx 90$).

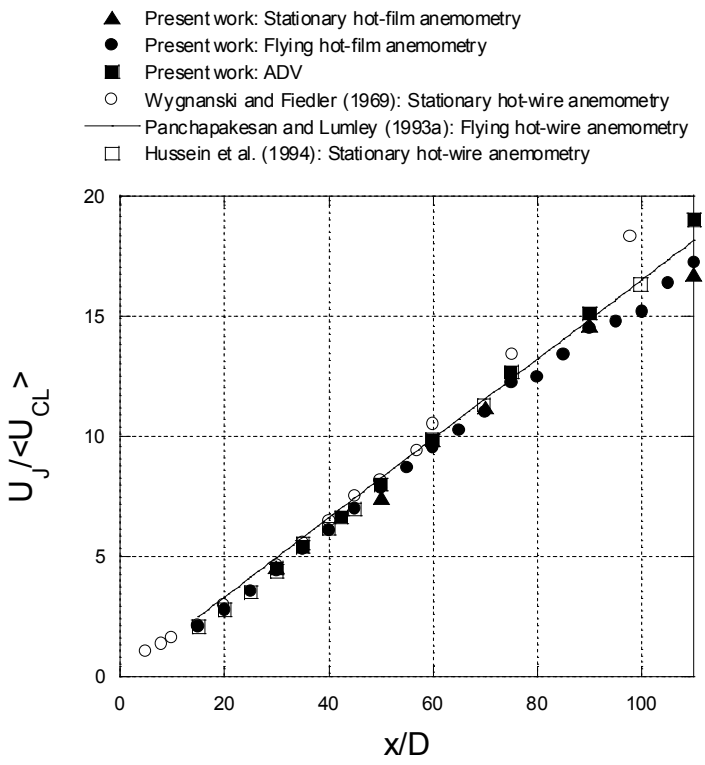

Figure 4.1 Downstream evolution of the centerline axial mean velocity of an axisymmetric turbulent jet at *Re* = 10,600 measured by stationary hot-film anemometry, flying hot-film anemometry and acoustic Doppler velocimetry. The data of Wygnanski and Fiedler (1969), Panchapakesan and Lumley (1993) and Hussein *et al.* (1994) are also included.

	Present work: stationary hot-film anemometry			Present work: flying hot-film anemometry			Present work: ADV			Wygnanski and Fiedler (1969): stationary hot-wire anemometry $x/D < 50$	Wygnanski and Fiedler (1969): stationary hot-wire anemometry $x/D > 50$	Panchapakesan and Lumley (1993): flying hot-wire anemometry	Hussein *et al.* (1994): stationary hot-wire anemometry	Hussein *et al.* (1994): laser-Doppler anemometry
Re	10,600			10,600			10,600			100,000		11,000	95,500	95,500
x_0/D	0	4	4.18	0	4	2.89	0	4	5.5	3	7	0	4	4
B	6.29	5.92	5.90	6.34	5.94	6.05	5.99	5.66	5.43	5.7	5	6.06	5.9	5.8
S	-			0.101			0.099			0.084		0.096	0.102	0.094

Table 4.1 The velocity decay constant (*B*), and spreading rate (*S*) for an axisymmetric turbulent jet.

In the self-similar region, the appropriately normalized mean velocity profile, results in the self-similar profile of the jet. As the jet width grows linearly with the downstream distance, the radial position can be normalized by the downstream distance. Therefore, a plot of $\langle U(r)\rangle/\langle U_{CL}\rangle$ versus r/x results in a universal profile of the jet that is not a function of downstream distance nor the Reynolds number in the self-similar region of the jet. The radial profile of axial mean velocity measured at $x/D = 35$ is presented in Figure 4.2. It was not possible to extract the raw data of Panchapakesan and Lumley (1993) — a curve fit to their data is shown in this graph. The mean velocity profiles measured using the flying hot-film anemometer and the ADV are in good agreement with those measured by Wygnanski and Fiedler (1969), Panchapakesan and Lumley (1993) and Hussein et al. (1994), with the flying hot-film data being slightly closer to that of the previous works near the jet centerline ($r/x = 0$).

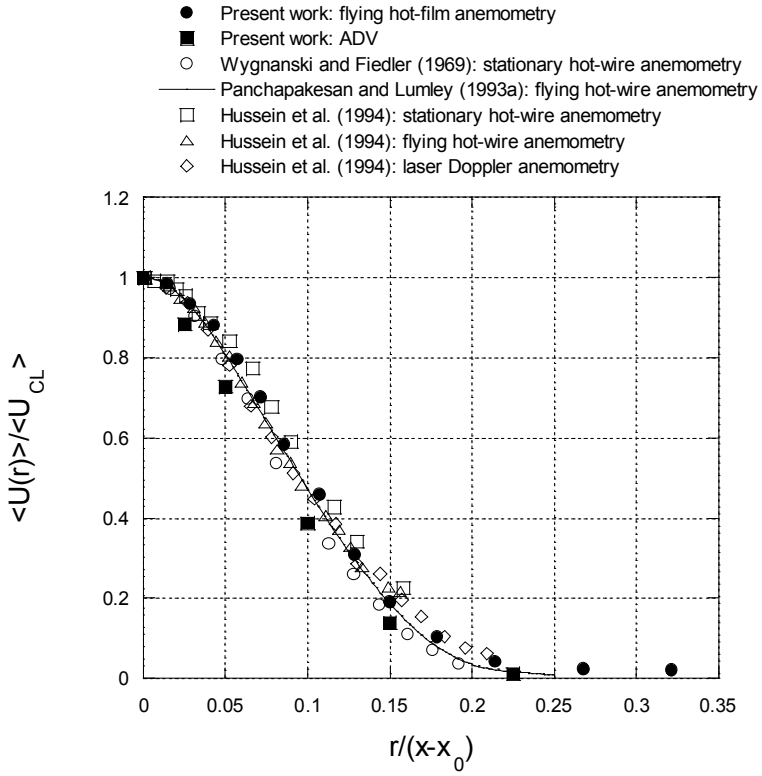

Figure 4.2 Radial profiles of the mean axial velocity for an axisymmetric turbulent jet for $Re = 10{,}600$. $x/D = 35$, $x_0 = 0$.

The mean radial velocity profiles measured by the ADV at x/D = 35 and 75 are shown in Figure 4.3. Similar to the mean axial velocity, $\langle V(r)\rangle/\langle U_{CL}\rangle$ plotted as a function of r/x should have a universal profile in the self-similar region. However, the magnitude of the radial velocities is small compared to the axial velocities. ($\langle V(r)\rangle$ is less than 40 times smaller than $\langle U_{CL}\rangle$ (Pope, 2000).) The mean radial velocity profiles have also been measured by Fukushima (2002) and Ying et al. (2004). Wygnanski and Fiedler (1969), Panchapakesan and Lumley (1993) and Hussein *et al.* (1994) do not present raw data for the mean radial velocity. In these studies, the $\langle V(r)\rangle$ data is calculated from the mean axial velocity profile using the continuity equation. In addition to our raw data, we also present the profile of the mean radial velocity calculated from the measured mean axial velocity in Figure 4.3. As observed in this figure, the ADV predicts the mean radial velocities relatively accurately, compared to previous estimates of $\langle V(r)\rangle$ obtained from the continuity equation. As would be expected, the agreement is better with the radial profiles obtained from the continuity equation using mean axial velocities measured herein (by the ADV and the flying hot-film anemometer). The profile agrees better at x/D = 75. This may be due to the fact that the jet fully reached a higher degree of self-similarity by x/D = 75. Note that, the radial velocity is negative at the edge of the jet. This indicates that the ambient fluid is entrained into the jet at its edges (Pope, 2000).

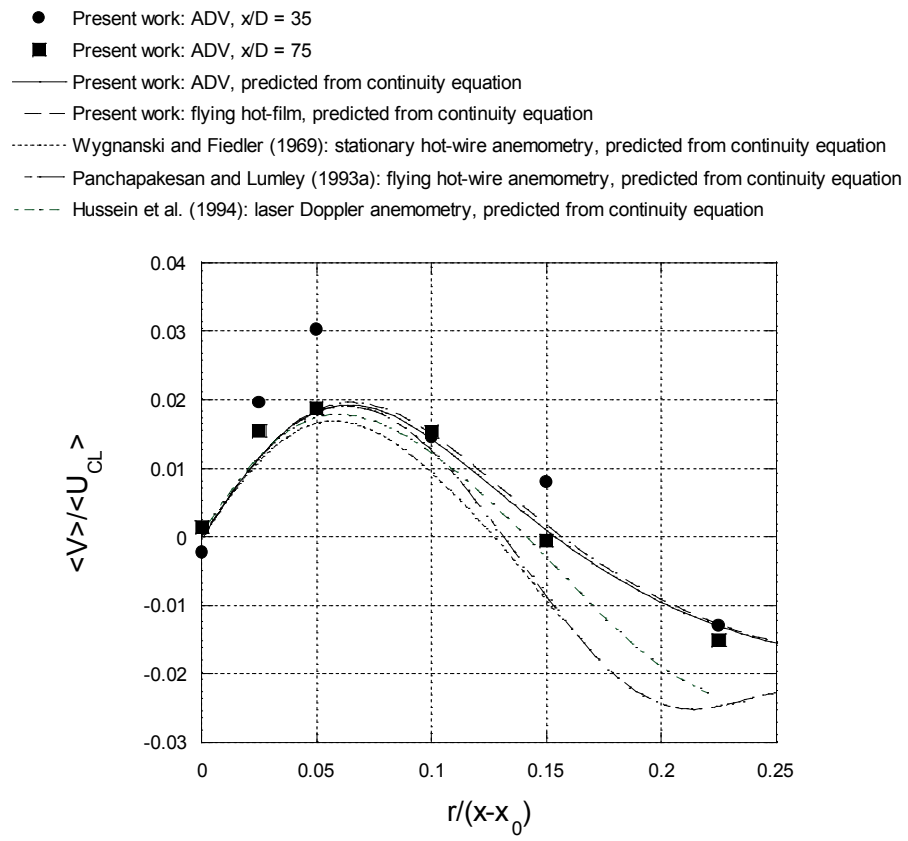

Figure 4.3 The mean radial velocity profile of an axisymmetric turbulent jet for Re = 10,600. x/D = 35 and 75, x_0 = 0. Note that the solid and dashed lines are the profiles obtained from the axial mean velocity profile using the continuity equation.

The half-width ($r_{1/2}$) of the jet is defined as the radial position at which the mean velocity reaches half its centerline value. $r_{1/2}$ is plotted as a function of downstream distance in Figure 4.4. Individual data points were not given in Panchapakesan and Lumley (1993) and Hussein *et al*. (1994) studies. As is theoretically predicted, it can be observed that the jet in a quiescent background grows linearly with the downstream distance in the self-similar region. Empirically stated, $r_{1/2} = S\ (x - x_0)$, where S is called the spreading rate. The spreading rate for the flying hot-film anemometry data is found to be 0.101 ($15 \leq x/D \leq 60$). For the ADV data, it is 0.099 ($30 \leq x/D \leq 75$). These spreading rates are consistent with those of the other studies (see Table 4.1). For $x/D > 60$, an increase in the slope of the data measured by the flying hot-film is observed. This is attributed to the low sensitivity of the flying hot-film apparatus at low

velocities. Table 4.1 shows that the spreading rate also appears to be independent of the Reynolds number.

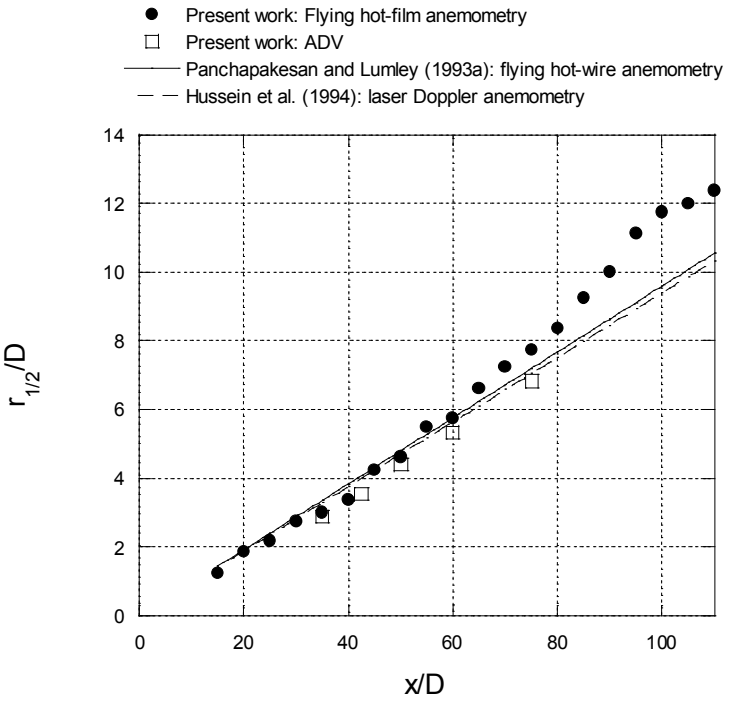

Figure 4.4 Downstream evolution of the half-width of an axisymmetric turbulent jet at Re = 10,600.

By integrating the area under the radial profiles of the mean axial velocity data, mass flow rates were calculated. The downstream evolutions of the mass flow rate (normalized by the mass flow rate at the nozzle exit, m_0), measured by the flying hot-film and ADV, are plotted in Figure 4.5, and are presented in Table 4.2. The jet entrainment rates (*i.e.,* the slope of the curve, dm/dx) are 0.34 and 0.42 for the ADV and flying hot-film, respectively. Ricou & Spalding (1961) and Panchapakesan and Lumley (1993) reported an entrainment rate of 0.32 ($m/m_0 = 0.32 \times (x - x_0)/D$, with $x_0 = 0$) for a round turbulent jet. The entrainment rate measured by the flying hot-film is 0.36 in the range $15 \leq x/D \leq 60$. However, the slope increases after $x/D = 60$, due to the low sensitivity of the hot-film at low velocities. If the virtual origin (x_0) of the curve fits to the data is forced to zero

(similar to Ricou & Spalding (1961)), entrainment rates of 0.30 and 0.38 (0.33 for $15 \leq x/D \leq 60$) are obtained for the ADV and flying hot-film, respectively.

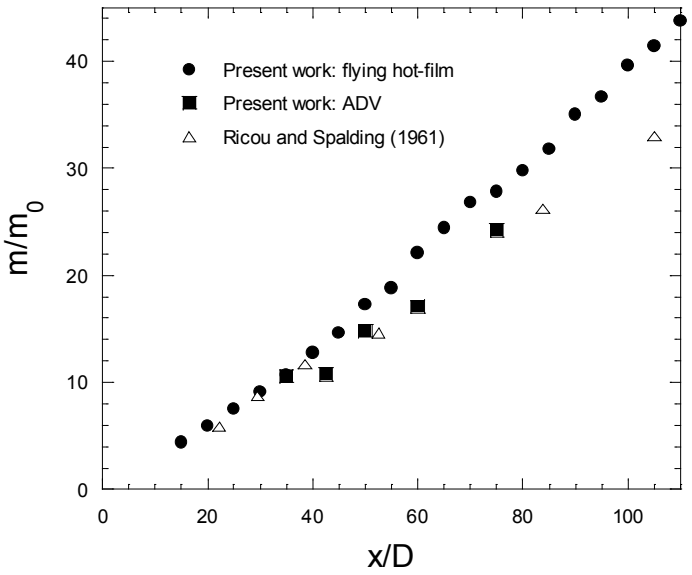

Figure 4.5 The downstream evolution of the mass flow rate of an axisymmetric turbulent jet (Re = 10,600).

		ADV	Flying hot-film anemometry	Flying hot-film anemometry	Ricou and Spalding (1961)	Panchapakesan and Lumley (1993)
Equation	Measurement range	$35 \leq x/D \leq 75$	$15 \leq x/D \leq 110$	$15 \leq x/D \leq 60$	$24 \leq x/D \leq 418$	Not given
$m/m_0 = dm/dx \times (x - x_0)/D$	dm/dx	0.34	0.42	0.36	-	-
$m/m_0 = dm/dx \times x/D$	dm/dx	0.30	0.38	0.33	0.32	0.32

Table 4.2 The entrainment rate for an axisymmetric turbulent jet. dm/dx is also presented for $m/m_0 = dm/dx \times x/D$ similar to Ricou and Spalding (1961).

4.2 RMS Velocity Statistics

Figure 4.6 plots the RMS axial velocity normalized by the mean velocity ($u_{rms}/\langle U_{CL} \rangle$) at the jet centerline. Note that only a curve fit was given for the data of Panchapakesan and Lumley (1993), and only the value of $u_{rms}/\langle U_{CL} \rangle$ in the self-similar region was presented by Hussein *et al*. (1994). Similar to the mean velocity, the RMS velocity decays as x^{-1}. Therefore, RMS velocities normalized

by mean velocities at the centerline should asymptote to a constant in the self-similar region. Although some variations in this quantity have been observed in the literature, no systematic dependence on the Reynolds number has been found (Pope 2000). Wygnanski and Fiedler (1969), and Hussein *et al*. (1994) measured $u_{rms}/\langle U_{CL}\rangle$ to be approximately 0.28 in the self-similar region, whereas Panchapakesan and Lumley (1993) measured a value of 0.24. In the present study, $u_{rms}/\langle U_{CL}\rangle$ at the centerline of the jet in the self-similar region is measured about 0.35 when measured using the ADV, while $u_{rms}/\langle U_{CL}\rangle$ measured by both stationary and flying hot-film anemometry is 0.27. The comparison shows that the ADV significantly overestimates $u_{rms}/\langle U_{CL}\rangle$ compared to the flying hot-film and other studies. As the mean velocity along the centerline is predicted relatively accurately by the ADV, the overestimated values of $u_{rms}/\langle U_{CL}\rangle$ must be due to abnormally large RMS velocities. In addition, the RMS velocities measured with the ADV reach self-similarity farther downstream when compared to the flying hot-film. Furthermore, $u_{rms}/\langle U_{CL}\rangle$ increases more from x/D = 30-110 for ADV ($0.25 \leq u_{rms}/\langle U_{CL}\rangle \leq 0.35$) as compared to the flying hot-film anemometry ($0.25 \leq u_{rms}/\langle U_{CL}\rangle \leq 0.27$) and the results of Panchapakesan and Lumley (1993).

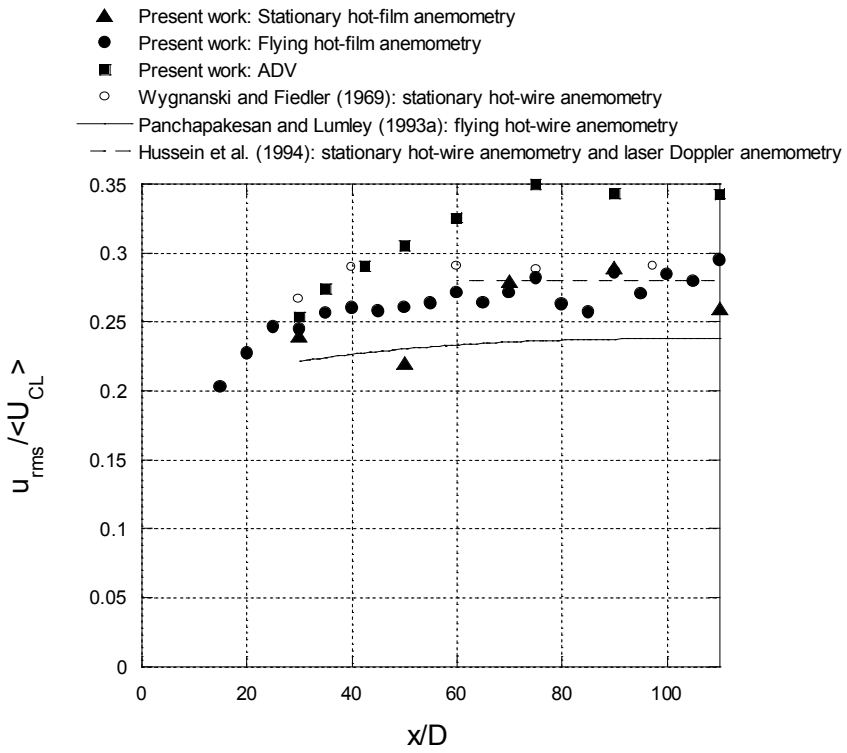

Figure 4.6 Downstream evolution of the axial RMS velocity at the centerline of the jet.

RMS radial velocities normalized by the mean velocity ($v_{rms}/\langle U_{CL}\rangle$ and $w_{rms}/\langle U_{CL}\rangle$) when measured by ADV at the jet centerline are shown in Figure 4.7. Only a curve fit was given for the data of Panchapakesan and Lumley (1993), and only the values of $v_{rms}/\langle U_{CL}\rangle$ and $w_{rms}/\langle U_{CL}\rangle$ in the self-similar region were presented by Hussein *et al*. (1994). By symmetry, v_{rms} and w_{rms} should be the same at the centerline of an axisymmetric jet, however ADV measurements yield $v_{rms}/\langle U_{CL}\rangle$ of about 0.3 and $w_{rms}/\langle U_{CL}\rangle$ of about 0.19 in the self-similar region. The RMS radial velocity normalized by the mean velocity at the centerline is estimated to be 0.25, 0.19 and 0.21 by Wygnanski and Fiedler (1969), Panchapakesan and Lumley (1993) and Hussein *et al.* (1994), respectively. Therefore, only $w_{rms}/\langle U_{CL}\rangle$ measured by the ADV agrees well with the results of other studies. The comparison of the RMS velocities measured by the ADV with those of the flying hot-film, Wygnanski and Fiedler (1969), Panchapakesan and Lumley (1993) and Hussein *et al.* (1994) shows that the ADV overestimates u_{rms}

and v_{rms} which are measured along the x- and y-directions of the probe. On the other hand, w_{rms} measurements (along the z-direction of the probe) are found to be relatively accurate. This is in agreement with the ADV measurements of Ming *et al.* (2008) in an axisymmetric turbulent jet. They reported $u_{rms}/\langle U_{CL}\rangle$ and $v_{rms}/\langle U_{CL}\rangle$ values (0.34 and 0.28, respectively) for $0 < x/D < 47$ which are similar to those presented here. However, their estimate of $w_{rms}/\langle U_{CL}\rangle$ was about 0.11. The lower RMS values in Ming *et al.* (2008) could be attributable to the flow not having become self-similar as the farthest downstream distance in their measurements was $x/D = 47$, while the present ADV measurements show that the RMS velocity normalized by the mean velocity reaches self-similarity around $x/D = 70$. The high error in u_{rms} and v_{rms} can be explained by the geometrical configuration of the ADV probe, which has higher noise in the x- and y-directions compared to the z-direction (Voulgaris and Trowbridge, 1998). The ADV noise will be discussed in detail in Chapter 5. The comparison of RMS velocities measured in this study and those of the other studies implies that only hot-film anemometry and the z-component of acoustic Doppler velocimetry are reliable for the measurement of turbulent fluctuations.

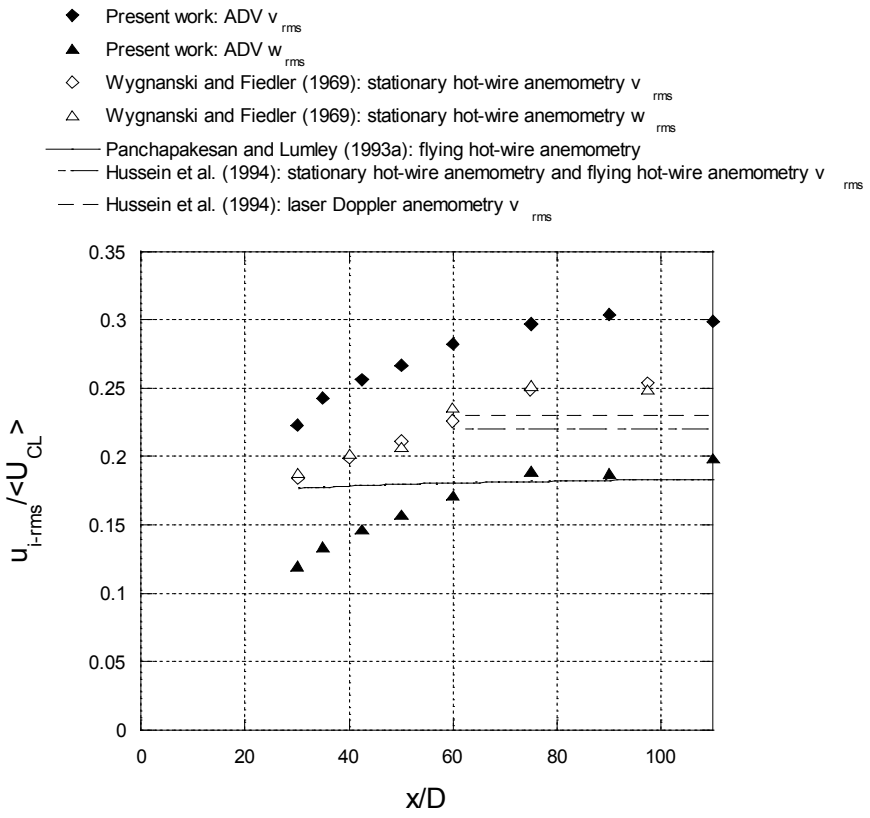

Figure 4.7 Downstream evolution of the RMS radial velocities at the centerline of the jet.

The normalized radial profile of the RMS axial velocity measured at x/D = 35 with the flying hot-film at Re = 10,600 is presented in Figure 4.8. It was not possible to extract the raw data of Panchapakesan and Lumley (1993) — a curve fit to their data is shown in this graph. As it can be seen in this figure, the present measurements agree well with those of Panchapakesan and Lumley (1993), and are slightly smaller than those measured by Hussein *et al*. (1994). Note that the Reynolds number of the present flow is almost identical to that of Panchapakesan and Lumley (1993) and approximately 9 times smaller than that of Hussein *et al.* (1994), which may explain the better agreement with the data of Panchapakesan and Lumley (1993).

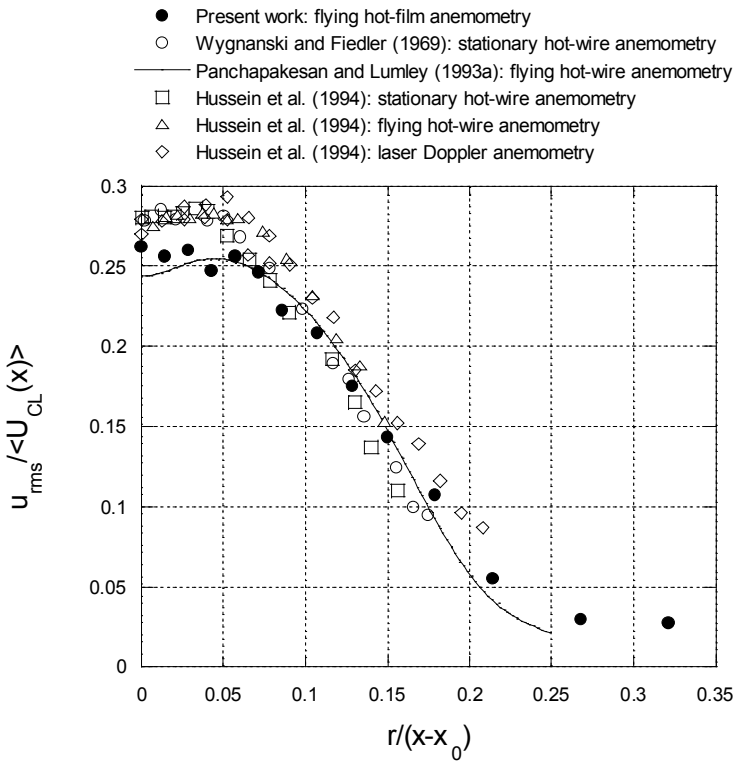

Figure 4.8 Axial RMS velocity profile of an axisymmetric turbulent jet for Re = 10,600. x/D = 35, x_0 = 0.

4.3 Conclusions

The results presented in this chapter validate the use of flying hot-film anemometry to estimate the mean and RMS velocities. The results also validate the use of ADV for the mean velocities (measured in all three directions) and the RMS velocity (measured in the z-direction, w_{rms}, only). In addition, ADV has shown itself to be more accurate than the flying hot-film anemometer at low velocities (far downstream and near the edges of the jet). Therefore, in the subsequent measurements herein, the flying hot-film will be used for measurements of the mean and RMS axial velocities. On the other hand the ADV will be used to measure: i) the mean radial velocities, and ii) the mass flow rate and the half-width, which particularly require accurate mean velocity measurements in the edges of, and far downstream in, the jet. In addition, the ADV (z-component) will be used along with the flying hot-film for the

measurements of the RMS velocities in the background turbulence, as only one velocity component of this flow can be measured by the flying hot-film.

Chapter 5

Results and Discussion

In Chapter 4, the measurements of i) the mean and RMS velocities using the flying hot-film anemometer, and ii) the mean velocities in all directions and the RMS velocity measured along the z-direction of the probe (w_{rms}), for the ADV, were validated. It was also shown that the ADV overestimated the RMS velocities measured along the x- and y-direction of the probe. The first section of this chapter is an attempt to improve the overestimated turbulence statistics measured with the ADV, as well as to relate the ADV's Doppler noise to the mean velocity. The second section presents the results pertaining to the effect of background turbulence on the jet. This section includes measurements of the velocity-field of the jet in the presence of background turbulence using the flying hot-film anemometer and the ADV. The final section of this chapter discusses the results.

5.1 Effect of Noise on Turbulence Measurements Using Acoustic Doppler Velocimetry

It was shown in Chapter 4 that the horizontal RMS velocities (measured along the x- and y-direction of the probe) measured by the ADV in the jet were overestimated when compared to i) stationary and flying hot-film anemometry measurements, and ii) the accepted values in the literature. Consequently, we try to improve upon the RMS velocities (measured by the ADV along the axis of the axisymmetric jet) using post-processing and noise-reduction methods in §5.1.1. Because the Doppler noise is expected to be a function of the mean velocity (Lemmin and Lhermitte, 1999), an investigation of the relationship between Doppler noise and the mean velocity is undertaken in §5.1.2 (including an attempt to eliminate the effect of the former). To this end, the measurements are made in i) a quiescent background, ii) a quiescent background with the ADV translating at a constant speed using a traversing mechanism, iii) homogeneous isotropic turbulence with no mean flow, and iv) homogeneous isotropic turbulence with an artificially generated mean velocity by translation of the ADV at a constant speed using a traversing mechanism.

5.1.1 Post-Processing and Noise-Reduction Methods

In this subsection, post-processing and noise-reduction methods presented in the literature for flows measured by ADV will be applied and tested using the previously-discussed turbulent jet flow. We will also propose a noise-reduction method for improving the RMS velocities measured along the axis of the jet.

The de-spiking filters of Goring and Nikora (2002) (phase-space thresholding method modified by Wahl (2002) which is used in the SONTEK data analysis software, WinADV) and Cea *et al*. (2007) were tested on the current jet data. However, they did not reduce the RMS velocities significantly as the signal quality was high in the present laboratory flow. They were therefore not beneficial

in correcting the spurious RMS velocity measurements discussed in the previous chapter.

We subsequently applied the noise-reduction method of Hurther and Lemmin (2001). In general, other noise-reduction filters, detect spikes (which usually result from a low quality signal) and eliminate them, or remove data with low signal-to-noise ratio and/or correlation. However, Hurther and Lemmin (2001) deal with the noise problem more fundamentally. In their method, the Doppler noise is estimated from the two quasi-instantaneous vertical velocities (measured simultaneously in the same sampling volume) and then subtracted from the other velocity components. The Nortek Vectrino ADV used in this research measures two quasi-simultaneous vertical velocities along the z-direction of the probe. To find the Doppler noise, the covariance of the two vertical velocities ($<w_1 w_2>$) was first calculated. As the noise signals of the two vertical velocities can be reasonably assumed to be uncorrelated, the covariance is noise-free (Hurther and Lemmin, 2001). Therefore, the covariance is the same as the true variance (*i.e.*, $<w_1 w_2> = <w_{T1}^2> = <w_{T2}^2>$). Assuming the correlation between the velocity and the noise to be zero, the covariance was subtracted from the measured variance (which includes the effects of Doppler noise) to find the variance of the noise for the w-component of the velocity ($<w_{Measured}^2> - <w_1 w_2> = <\sigma_w^2>$). If the receiver transducers are identical and ideal, then we can assume that the noise variance is the same along each receiver beam. Using the transformation matrix, the variances of the noise were then calculated for the u and v velocity components. Subsequently, the variance of the noise was subtracted from the variances of the u and v velocities to find the true variances (and therefore RMS velocities). The results are presented and compared with the uncorrected RMS velocities in Figure 5.1 and Figure 5.2. It can be seen that the noise-reduction method improves the data. u_{rms} and v_{rms} decreased by up to 15% at some points, while w_{rms} did not change significantly, as expected. Although the RMS velocities measured by the ADV were improved using the noise-reduction method of Hurther and Lemmin (2001), they nevertheless remained larger than

those measured by the present flying hot-film anemometer measurements and previous studies.

Velocity spectra of all three velocity components measured using ADV at the jet centerline and $x/D = 110$ are shown in Figure 5.3. As can be seen, the u and v spectra have a higher noise floor. In addition, the v and the w spectra should collapse due to axisymmetry of the jet. However, the v spectrum (artificially) exhibits more turbulent kinetic energy because of the presence of noise. In another attempt to improve the jet RMS velocity, we estimated the noise in v_{rms} by subtracting the velocity spectrum of w (assumed to have negligible noise) from the velocity spectrum of v, which results in the noise spectrum for v_{rms} (shown in Figure 5.4). The variance of the noise in y-direction was then converted to that of the x-direction using the ADV transformation matrix (assuming that the noise is the same along each receiver beam). The noise was then subtracted from u_{rms}. The results presented in Figure 5.1 show that $u_{rms}/\langle U \rangle$ calculated by this method, agrees well with the stationary hot-film data, flying-hot-film data and those of the other previous studies. This method can be used to find the true RMS velocities i) in axisymmetric flows, or ii) in any flow, if two spectral measurements are made using two different ADV probe orientations.

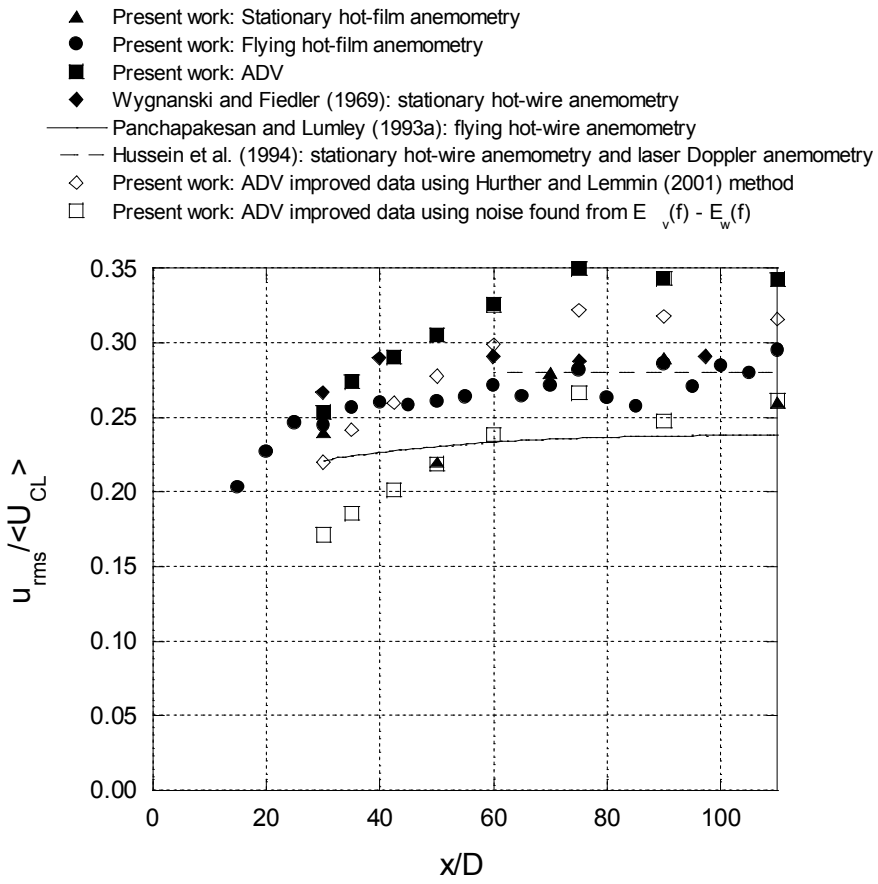

Figure 5.1 Axial RMS velocities at the centerline of the jet measured by the ADV after applying i) the noise-reduction method of Hurther and Lemmin (2001), and ii) the noise-reduction method proposed in this work to the data.

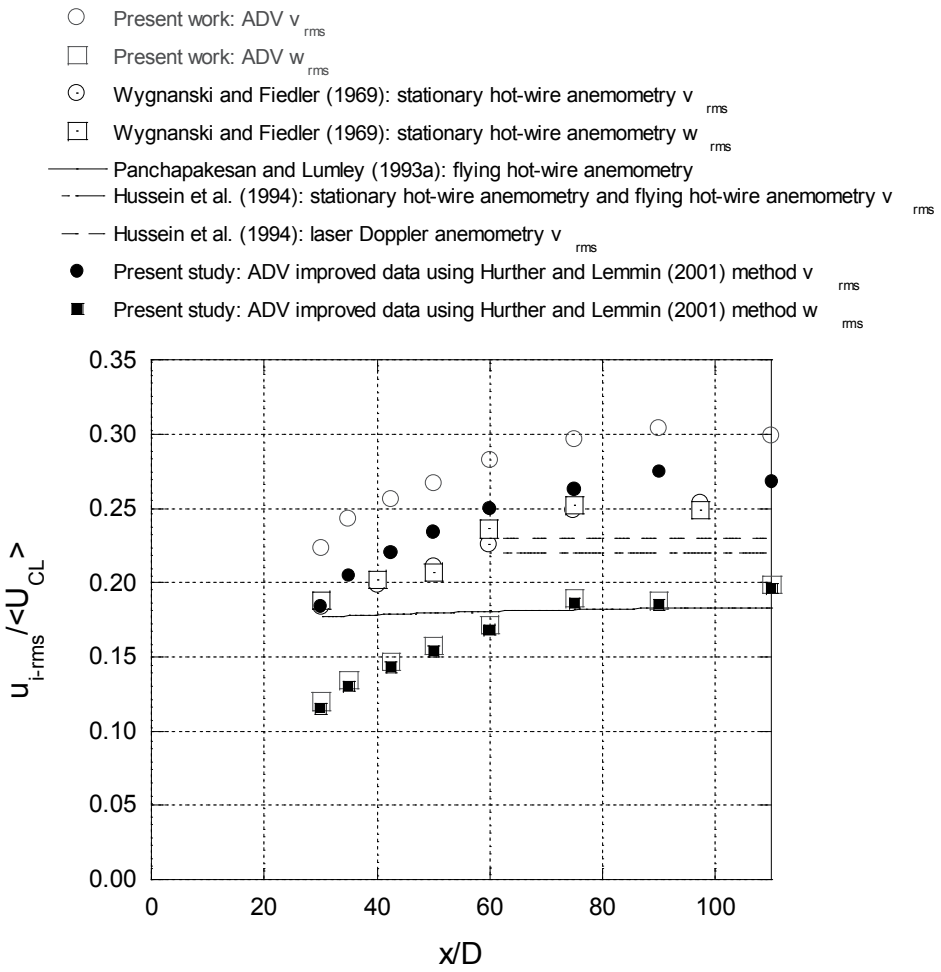

Figure 5.2 Radial RMS velocities at the centerline of the jet measured by the ADV after applying the noise-reduction method of Hurther and Lemmin (2001) to the data.

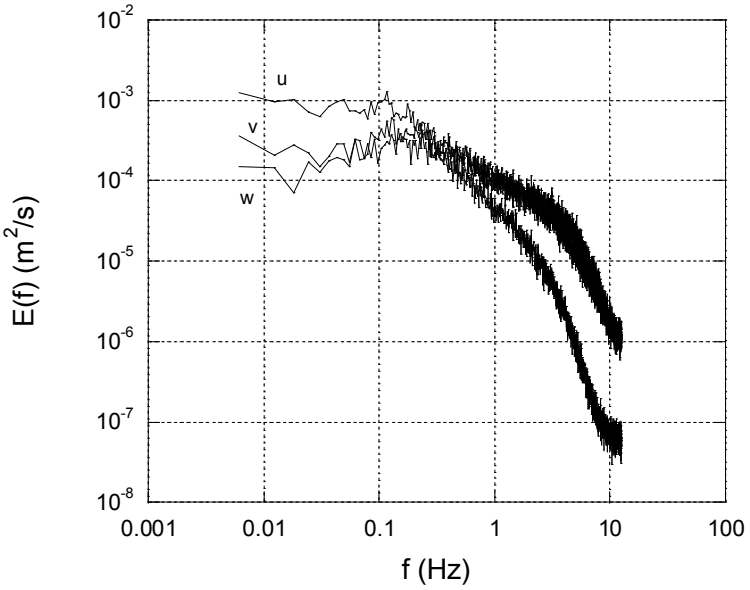

Figure 5.3 Velocity spectra of the jet centerline measured by ADV at $x/D = 110$.

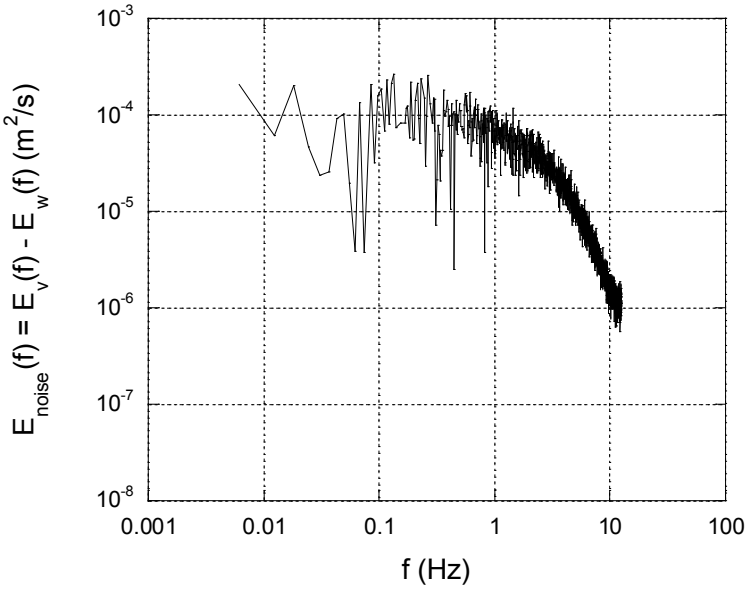

Figure 5.4 ADV noise spectrum of the jet at $x/D = 110$ obtained from subtracting $E_w(f)$ from $E_v(f)$.

5.1.2 Relationship between Doppler Noise and Mean Velocity

To improve the precision of turbulence statistics measured by the ADV, we attempted to find a relationship between the Doppler noise and the mean velocity to, therefore, reduce the noise from the turbulence statistics for a given mean velocity. This was motivated by the work of Lemmin and Lhermitte (1999), which will be explained below.

Nikora and Goring (1998) presented a post-processing filter that subtracted the Doppler noise from the ADV's measured velocities. To do so, they carried out velocity measurements with the ADV in a quiescent background and considered the signal measured therein as Doppler noise. Assuming the correlation between the velocity and the noise to be zero, they subtracted the measured noise from the measured velocity to estimate the true velocity. However, Lemmin and Lhermitte (1999) rejected this technique, remarking that the Doppler noise is an increasing function of the flow's mean velocity and velocity measurements in the quiescent background therefore do not accurately predict the Doppler noise. Here, we attempt to find a relationship between the Doppler noise and the mean velocity, and subsequently subtract the noise from the (over-estimated) RMS velocities.

A further series of experiments was conducted using the ADV in turbulent and non-turbulent backgrounds to investigate the relation between the Doppler noise and the mean velocity. The experiments were carried out in approximately homogeneous, isotropic, zero-mean-flow turbulence generated by the RJA and in a quiescent background. For both background conditions, the ADV was either kept stationary or moved at a constant speed by the Aerotech traversing mechanism (described in Chapter 3). The traversing mechanism speeds were 10 cm/s and 20 cm/s – values similar to the jet centerline velocities measured in the first set of experiments (at $x/D = 75$ and $x/D = 42.5$, respectively).

The results of these experiments are summarized in Table 5.1. As the pulse length (which is determined by the ADV's velocity range) contributes to the noise (Voulgaris and Trowbridge, 1998), the same velocity range (±0.3 m/s) was chosen for all the tests in this set of experiments. The velocity measured by the ADV in the quiescent background is presented in the first three columns of this table. In the first column, the velocity measured by the stationary ADV is shown. The second and third columns present the velocity statistics corresponding to the experiments in which the ADV was translated at constant speeds of 10 cm/s and 20 cm/s, respectively, in the y-direction. The RMS velocities in a quiescent background should ideally be zero; therefore the measured RMS velocities are attributable to the different sources of experimental error. The RMS velocities shown in the first three columns are relatively small. Relative to the mean velocity, the RMS velocities are less than 3% for the cases in which the ADV was moved at a constant speed. The results in this table also indicate no clear dependence of the noise on the mean velocity. Although the RMS velocities increased when the ADV traversing velocity increased from 10 cm/s to 20 cm/s, the RMS velocities were lower when the ADV was translated at 10 cm/s than for the stationary ADV. This may be due to increased noise from a reduced signal because the glass beads may be driven out of the measurement volume when there is no flow (and not replaced with beads from elsewhere in the flow).

Similar experiments were carried out in a turbulent background generated by the random jet array to investigate the effect of mean flow on the noise in the presence of homogenous turbulence in the background. The results are presented in the last three columns of the table. Similar to the measurements in the quiescent background, no clear relation can be observed between the RMS velocities and the mean velocity of the flow. In other words, the measured RMS velocities in a turbulent flow with no-mean velocity do not significantly differ from those measured in the same flow when imposing a constant mean velocity by translating the ADV. Hence, the Doppler noise does not appear to be a monotonic function of mean velocity, for the range of velocities studied herein, in contrast with the argument of Lemmin and Lhermitte (1999).

Finally, subtracting the velocity variances measured with the ADV moving at a constant speed in quiescent background from the measured jet and background turbulence velocity variance (assuming zero correlation between the velocity and noise signals), reduced the RMS velocities (or variance squared) by less than 1%. This is significantly less than our observed error in the ADV measurements made on the axis of a turbulent jet or in a turbulent background. This suggests that either the Doppler noise is a function of other parameters (which were not accounted for here), or there are other intrinsic sources of error in acoustic Doppler velocimetry.

cm/s	Without background turbulence			With background turbulence		
ADV velocity	0	10	20	0	10	20
$<U>$	-0.03±0.42	0.00±0.01	0.01±0.01	0.12±0.02	-0.03±0.45	-0.08±0.19
$<V>$	-0.17±0.26	9.68±0.03	19.25±0.35	0.13±0.06	9.78±0.06	19.43±0.21
$<W>$	-0.41±0.51	-0.16±0.02	-0.17±0.24	-0.24±0.02	-0.27±0.01	-0.38±0.01
u_{rms}	0.47±0.08	0.25±0.01	0.33±0.01	2.47±0.01	2.32±0.03	2.44±0.04
v_{rms}	0.30±0.14	0.22±0.01	0.37±0.01	1.81±0.02	1.65±0.04	1.69±0.04
w_{rms}	0.19±0.06	0.15±0.01	0.27±0.01	1.50±0.02	1.45±0.01	1.46±0.06

Table 5.1 Velocity statistics measured by the ADV in: column 1) a quiescent background, column 2 & 3) a quiescent background with the ADV translating at a constant speed in the y-direction using a traversing mechanism, column 4) homogeneous isotropic turbulence with no mean flow, and column 5 & 6) homogeneous isotropic turbulence with an artificially generated mean velocity by translating the ADV at a constant speed in the y-direction using a traversing mechanism.

5.2 Effect of Background Turbulence on an Axisymmetric Turbulent Jet

In Chapter 4, we validated our measurements of i) the mean and RMS velocities for the flying hot-film anemometer, and ii) the mean velocities in all directions and the RMS velocity measured along the z-direction of the probe (w_{rms}), for the ADV. In addition, the ADV was shown to be more accurate for the measurement of low mean velocities (*i.e.*, far downstream and near the edges of the jet) than flying hot-film anemometry. Therefore, in this section, the flying hot-film will be used for measurements of mean and RMS axial velocities in the jet and the horizontal transverse velocities of the background turbulence. The ADV will be used to measure i) the mass flow rate and the half-width (which require radial profiles of the mean axial velocity at all downstream locations), ii) the mean radial velocities in the jet, and iii) the downstream and the vertical transverse velocities of the background turbulence (which are not measured by the flying hot-film anemometer because it only allows for measurements in one direction).

The remainder of this section is structured as follows. Statistics of the background turbulence (measured by acoustic Doppler velocimetry and flying hot-film anemometry) will be presented in §5.2.1. Measurements of an axisymmetric turbulent jet at three Reynolds numbers issuing into different levels of background turbulence will follow in §5.2.2.

5.2.1 Turbulent Background

The random jet array produced a turbulent background flow that was approximately isotropic and with zero-mean flow. Figure 5.5 shows a schematic of the RJA as well as the coordinate system used herein. A summary of the RJA performance is presented in Table 5.2. The statistics are presented at 82.5 cm and 110 cm "downstream" of the RJA (y/M = 5.5 and y/M = 7.3, respectively, where M is the mesh size, *i.e.*, the distance between the jets of the RJA). In this table,

$\langle U \rangle$, $\langle V \rangle$, and $\langle W \rangle$ are the respective mean velocities in the horizontal transverse, downstream, and vertical transverse directions. u_{rms}, v_{rms} and w_{rms} are the RMS velocities in the same respective directions. S ($\equiv \langle u_\alpha^3 \rangle / \langle u_\alpha^2 \rangle^{3/2}$) and K ($\equiv \langle u_\alpha^4 \rangle / \langle u_\alpha^2 \rangle^2$) are the skewnesses and kurtoses of the velocity fluctuations (u_α = u, v or w) in each direction. (Angular brackets denote average quantities.) The turbulent kinetic energy per unit mass is defined as $\frac{1}{2}(\langle u^2 \rangle + \langle v^2 \rangle + \langle w^2 \rangle)$. Due to the symmetry of the RJA, the statistics in the x and z directions should be identical. In Table 5.2, the statistics in the x-direction (horizontal transverse) were measured with the flying hot-film anemometer. This is because the experimental setup only allows movement of the hot-film probe (and therefore measurements) in x-direction. The statistics in the y- and z-directions (downstream and vertical transverse, respectively) were measured using (the z-component of) the ADV. Note that the statistics for the vertical transverse at y/M = 5.5 were not measured.

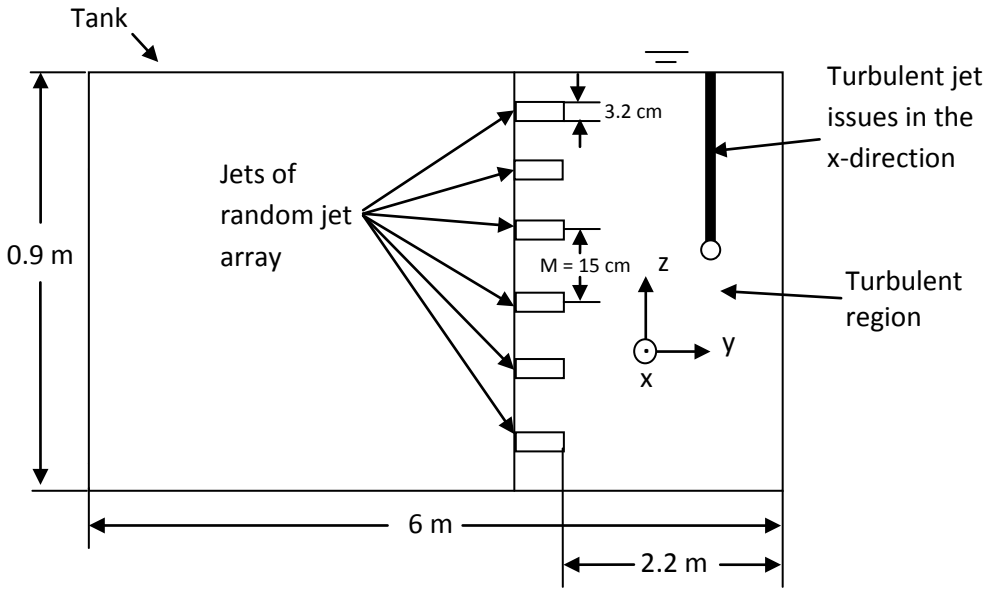

a) Side view

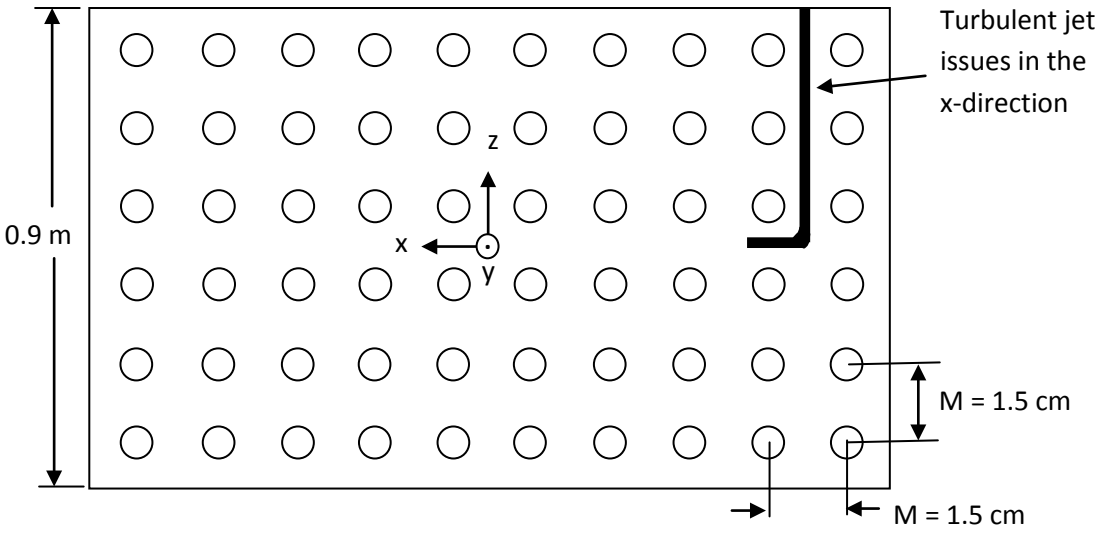

b) Front view

Figure 5.5 Schematic of the jet, the RJA and the tank. (a) side view. (b) front view. (Not to scale.)

Downstream distance [y/M]	u_α	$\langle U_\alpha \rangle$ [cm/s]	$u_{\alpha\,rms}$ [cm/s]	$\frac{\langle U_\alpha \rangle}{u_{\alpha\,rms}}$	Anisotropies			S	K	$\frac{1}{2}\langle u_i u_i \rangle$	ℓ [cm]
					$\frac{u_{rms}}{u_{\alpha\,rms}}$	$\frac{v_{rms}}{u_{\alpha\,rms}}$	$\frac{w_{rms}}{u_{\alpha\,rms}}$				
5.5	u	0.61±0.05	2.31±0.03	0.27±0.02	1	1.23	–	0.39±0.09	5.42±0.62	9.33±0.06	2.6
	v	0.31±0.13	2.84±0.04	0.11±0.04	0.81	1	–	1.18±0.06	4.6±0.40		
	w	–	–	–	–	–	–	–	–		
7.3	u	0.03±0.18	1.53±0.02	0.07±0.08	1	1.36	0.97	0.07±0.16	4.51±0.01	4.44±0.15	2.8
	v	-0.30±0.17	2.08±0.14	-0.15±0.10	0.73	1	0.72	1.43±0.12	5.73±0.66		
	w	0.10±0.10	1.49±0.05	0.07±0.07	1.03	1.40	1	-0.18±0.08	4.05±0.21		

Table 5.2 Background turbulence conditions at y/M = 5.5 and y/M = 7.3 (M = 15cm). Note that u is measured with the flying hot-film and v and w are measured with the z-component of the ADV. The statistics for w at y/M = 5.5 were not measured, so the turbulent kinetic energy ($\frac{1}{2}\langle u_i u_i \rangle$) was calculated as $\frac{1}{2}(\langle u^2 \rangle + \langle v^2 \rangle + \langle u^2 \rangle)$, due to the symmetry of the RJA. ℓ is the integral length scale calculated from the spatial autocorrelation of u.

From the table, it can be observed that the zero-mean flow assumption is generally valid for this flow, as the mean velocities normalized by their respective RMS velocities are generally small ($<U_\alpha>/u_{\alpha\ rms} << 1$). These values are comparable with those obtained by Variano *et al*. (2004) and Variano and Cowen (2008). The small mean flow measured herein is also significantly lower than that generally found in quasi-isotropic turbulence generated by oscillating grids (up to 60%) (Fernando and De Silva, 1993; Thompson and Turner, 1975; McDougall, 1979).

For an isotropic flow, the ratios of the RMS velocities should be 1. The results in Table 5.2 indicate that the flow is close to being isotropic at the measurement locations (especially in the transverse plane), though not perfectly isotropic. The flow generated by oscillating grids is typically characterized by anisotropy ratios between 1.1 and 1.2 (Hopfinger and Toly, 1976).

The observed $O(1)$ skewness of the fluctuating downstream velocity indicates that the probability density function (PDF) of the downstream velocity is asymmetric, with a greater chance of positive fluctuations than negative ones. This is a feature of spatially decaying turbulence (Variano and Cowen, 2008). That being said, the skewnesses of the u and w velocity fluctuations indicate that their PDFs are almost perfectly symmetric. The kurtosis of all velocity components are greater than 3, indicating that the probability of large fluctuations is somewhat greater than that of a Gaussian distribution.

Velocity spectra of the downstream and transverse velocity components (measured with the ADV at y/M = 5.5 and 7.3) are plotted in Figure 5.6. All three spectra are similar, with each having a moderately large inertial subrange. Figure 5.6b) (which plots the spectra at y/M = 7.3) shows that the spectrum of the downstream velocity component is higher in the energy containing range (low frequencies) when compared to that of the transverse one, consistent with the larger RMS values given in Table 5.2. However, the spectra are similar in the inertial subrange and dissipation range.

Velocity spectra of the horizontal transverse velocity component measured with the flying hot-film at y/M = 5.5 and 7.3 downstream of the RJA are plotted in Figure 5.7. In contrast with the Eulerian temporal spectra measured with the ADV and shown in Figure 5.6, the flying hot-film anemometer measured Eulerian spatial spectra, which required the use of Taylor's frozen-flow hypothesis in their calculation.

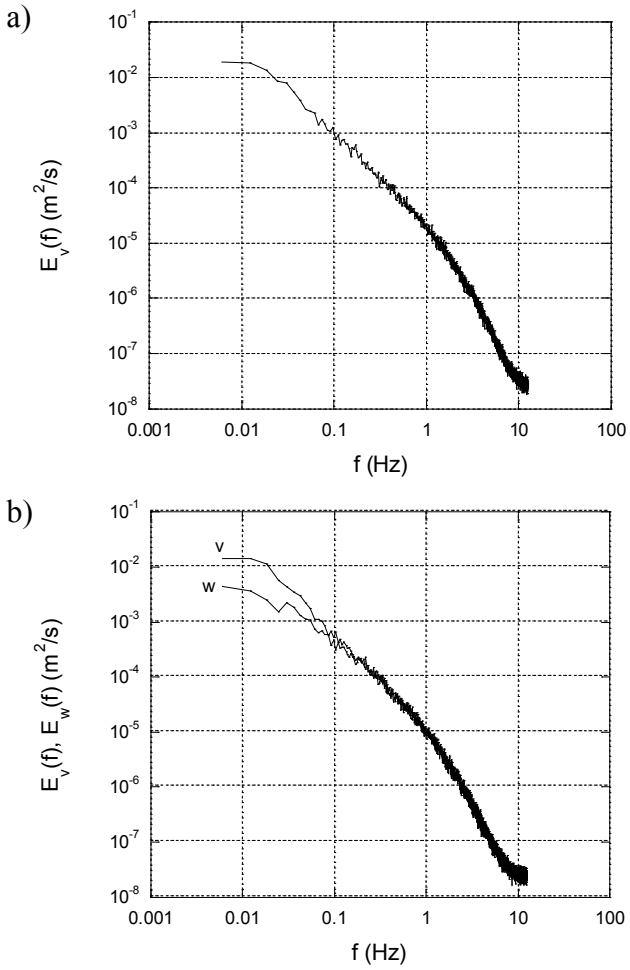

Figure 5.6 Velocity spectra measured by ADV in the turbulent background. (a) Spectrum of the downstream velocity component (v) at y/M = 5.5, (b) Spectrum of the downstream (v) and the vertical transverse (w) velocity components at y/M = 7.3. Note that the vertical transverse velocity (w) was not measured at y/M = 5.5.

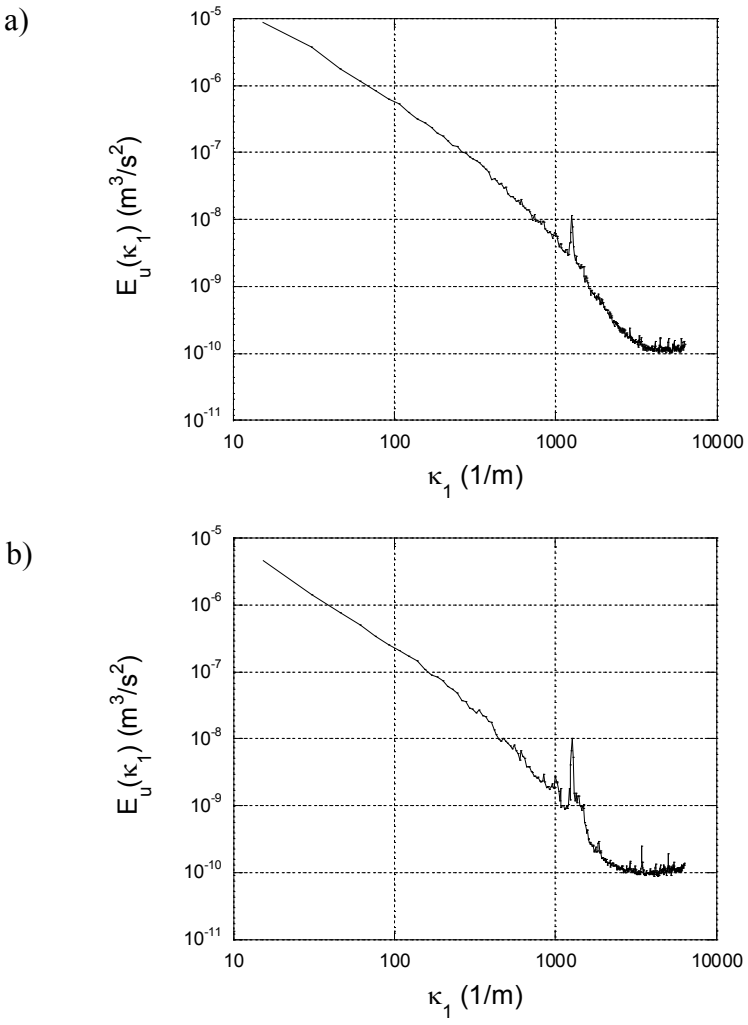

Figure 5.7 Velocity spectra measured by flying hot-film anemometry in the turbulent background. κ_1 is the longitudinal wavenumber (estimated using Taylor's hypothesis as: $\kappa_1 = 2\pi f/\langle U_1 \rangle$, where $\langle U_1 \rangle$ is the mean velocity along the horizontal transverse direction.). (a) Spectrum of the horizontal transverse velocity component (u) at y/M = 5.5, (b) Spectrum of the horizontal transverse velocity component at y/M = 7.3.

The downstream decay of the background turbulence was determined by measuring the velocities along a transect orthogonal to the plane of the RJA, for different positions – *i.e.*, different (x/M, z/M). Results are shown in Figure 5.8, which plots the downstream decay of the vertical transverse (w_{rms}, measured with the ADV) and the horizontal transverse (u_{rms}, measured with the flying hot-film) RMS velocities. It is clear that, far enough away from the grid, the RMS velocities, and therefore turbulent kinetic energy, become independent of the

transverse location, as the four curves collapse for y/M > 6. This implies that the turbulence becomes axisymmetric about the y-axis. In this region, a log-law version of this plot indicates that the RMS velocities measured with the ADV and the flying hot-film decay as $\sim y^{-1.31}$ and $\sim y^{-1.37}$, respectively, slightly faster than the y^{-1} dependence observed in oscillating grid turbulence. Note that the downstream distance is normalized by the centre to centre distance between the RJA pump outlets (M = 15 cm).

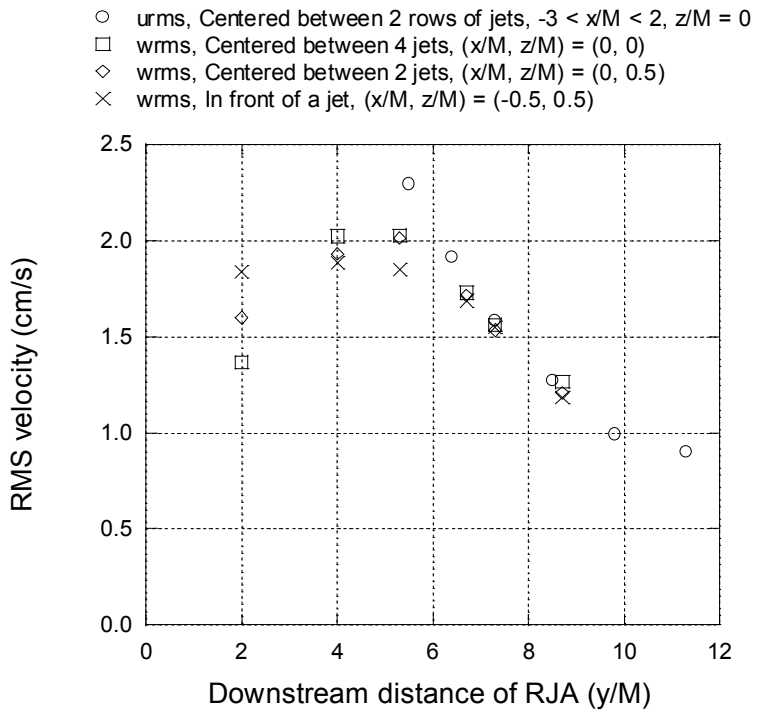

Figure 5.8 Decay of the RMS velocities in the background turbulence as a function of downstream distance from the RJA.

Although the flow decayed in the y-direction, the symmetric configuration of the random jet array should result in a two-dimensional flow (away from the boundaries and far enough downstream). (Figure 5.8 has already provided evidence supporting this hypothesis.) To verify the flow's homogeneity in these directions, measurements of the turbulent background velocity field were acquired in vertical planes. The ADV measurements were conducted at y/M = 7.3, along four transects, two horizontal, which passed through: a) z/M = 0, and b) z/M = 1.5,

and the other two vertical, which passed through: c) x/M = 0, and d) x/M = -1.5 (Figure 5.9). The homogeneity results measured by ADV are shown in Figure 5.10. Figures 5.10a) and 5.10b) show that the RMS velocities were approximately homogeneous in the horizontal direction, and Figures 5.10c) and 5.10d) show that the RMS velocities were approximately homogeneous in the vertical direction. The homogeneity was also confirmed by the flying hot-film measurements which were conducted at y/M = 5.5 and y/M = 7.3 along the horizontal transect, which passed through: z/M = 0 (Figure 5.11). The flow is clearly not homogeneous in the y-direction due to the decay of the turbulence away from the RJA. Consistent with Figure 5.8, the flow's homogeneity increases with larger downstream distance. (This decay could be eliminated over a central part of the flow by the construction of another RJA that would be placed in the tank facing the existing one. By symmetry, the two decaying flows would now "cancel" one another, at least near the centre of the flow field, away from both RJAs.)

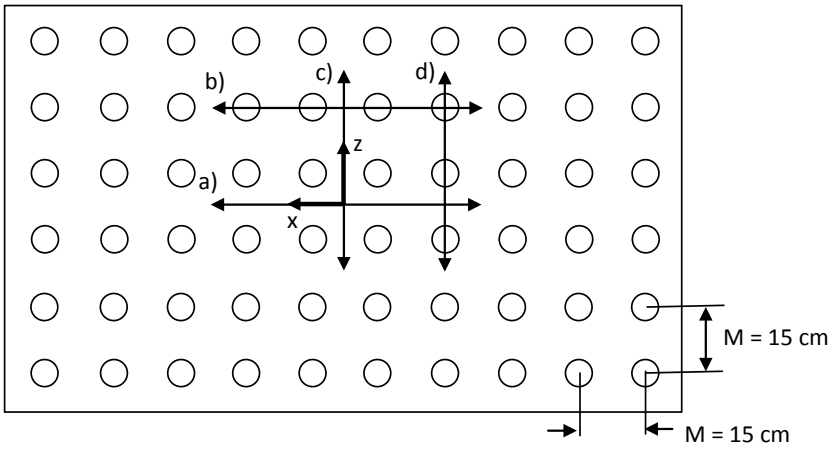

Figure 5.9 Front view schematic of the RJA which shows the four transects along which the homogeneity measurements were conducted.

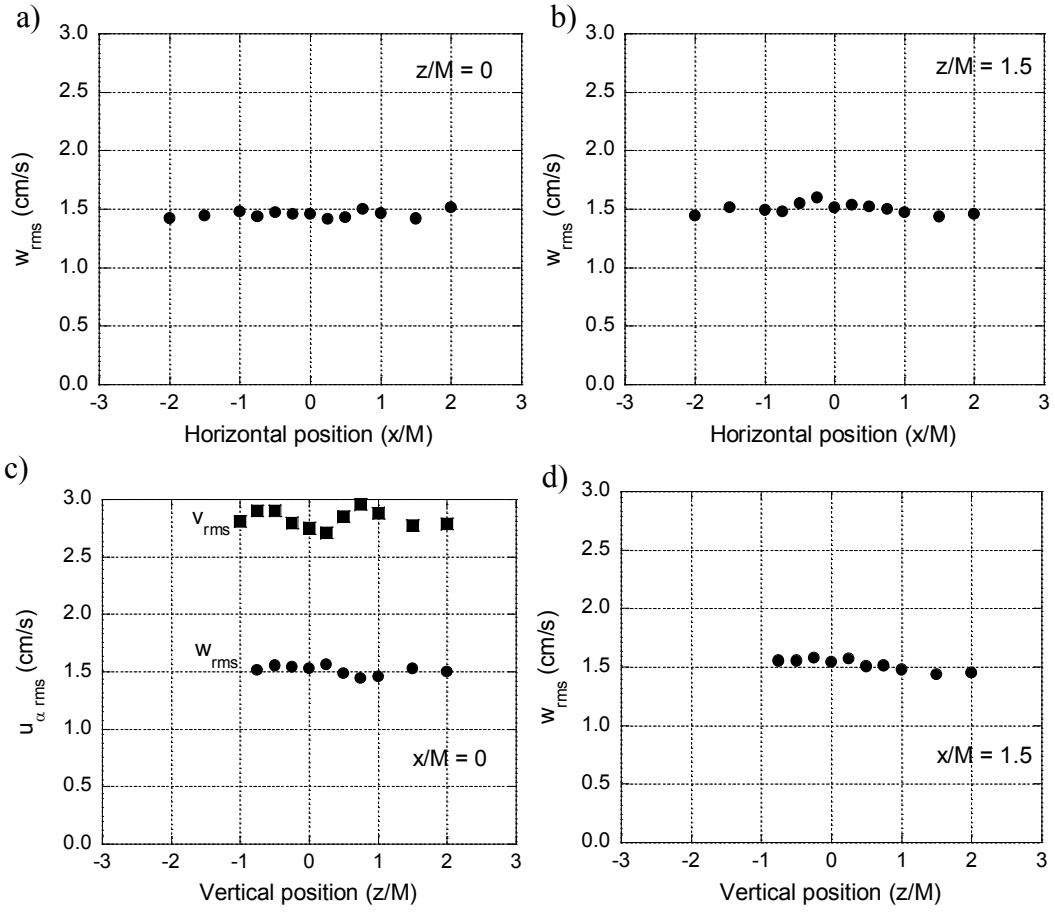

Figure 5.10 Horizontal and vertical homogeneity measured by the ADV at *y*/M=7.3. (a) RMS velocities along a horizontal line passing through *z*/M = 0 (b) RMS velocities along a horizontal line passing through *z*/M = 1.5. (c) RMS velocities along a vertical line passing through *x*/M = 0. (d) RMS velocities along a vertical line passing through *x*/M = -1.5.

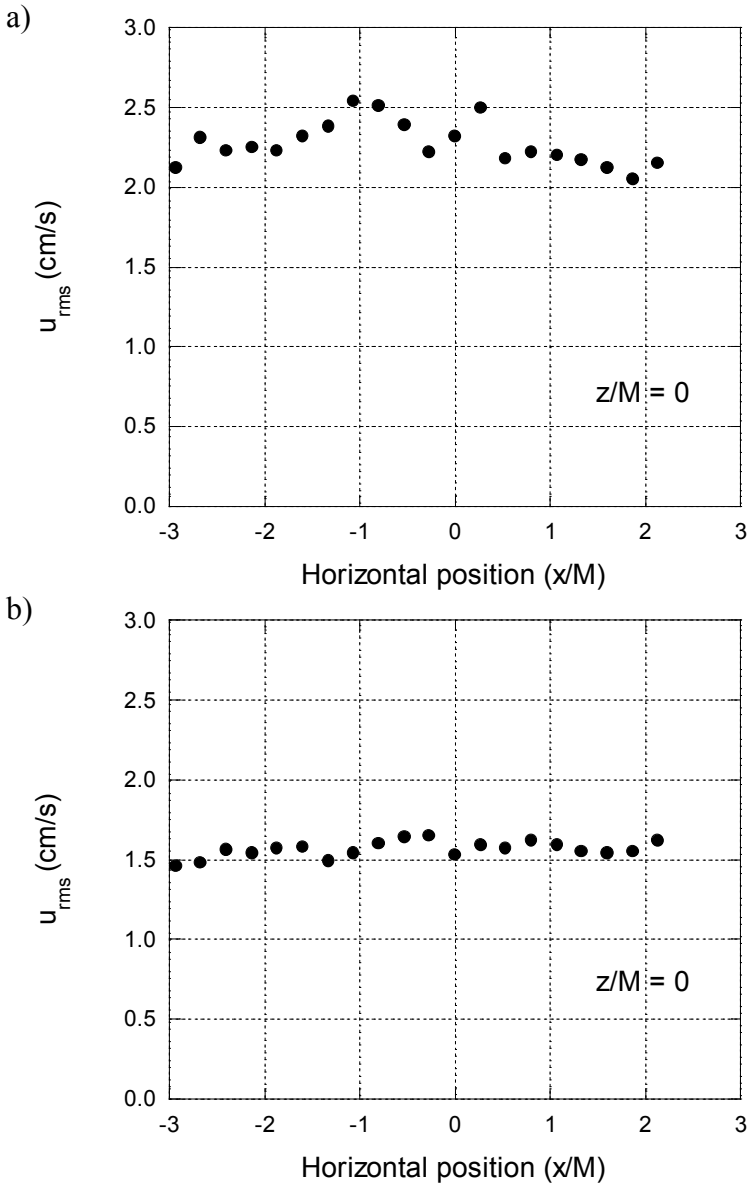

Figure 5.11 Horizontal homogeneity measured with the flying hot-film along a horizontal line passing through passing through z/M = 0 at (a) y/M = 5.5, and (b) y/M = 7.3.

5.2.2 Turbulent Jet Emitted into a Turbulent Background

In this section, the statistics of an axisymmetric turbulent jet issuing into a turbulent background with zero mean flow will be presented. The mean axial and RMS axial velocities presented herein were measured with the flying hot-film anemometer. The evolution of the jet half-width and mass flow rate require fine resolution in regions of small jet velocities (*i.e.*, at the edges of and far downstream in the jet). Therefore, the ADV (which was shown in Chapter 4 to better resolve small mean flows) was used to measure these two quantities. Furthermore, the mean radial velocity in the jet could also be measured by the ADV.

Measurements of a jet in the presence of background turbulence were performed at two different turbulence levels: TKE = 4.44 cm^2/s^2 and 9.33 cm^2/s^2. In the rest of this chapter, these will be referred to as the low and high levels of TKE, respectively. The jet at a Reynolds number of 10,600 was initially chosen as it was above the mixing transition (Dimotakis, 2000). To further investigate the effect of background turbulence on the jet's parameters, especially the breakup location and decay exponents, the Reynolds number of the jet was reduced to 5,300, so that these occur within the measurement range. It will be shown that the jet breaks up early at Re = 5,300. Therefore, the jet Reynolds number of 5,800 will also be investigated. Therefore, the results will be presented for three Reynolds numbers of 10,600, 5,800 and 5,300.

Figure 5.12 plots the downstream evolution of the centerline mean axial velocity of a turbulent jet (normalized by the nozzle exit velocity) issuing into a quiescent flow and into the low and high levels of background turbulence for three jet Reynolds numbers. It is seen in Figure 5.12 that the background turbulence causes an accelerated decay of the jet centerline velocity. Figure 5.13 plots the log-log version of the centerline mean axial velocity. As can be seen in these figures, in the presence of background turbulence, the jet decays faster as the level of background turbulence increases from the low-TKE, to the high-TKE,

and in the presence of background turbulence, $<U_{CL}>/ U_J$ does not vary as x^{-1} (which is the case for a jet in a quiescent background). Figure 5.13 shows that, in the presence of background turbulence, the jet decay is initially governed by a power-law. The power-law region is followed by a faster logarithmic decay. The decay constants (determined only from the power-law decay region) for the three Reynolds numbers are given in Table 5.3. In addition, the centerline mean velocity of the jet at the low level of background turbulence reaches zero at downstream distances of x/D = 90, 60 and 45 for Re = 10,600, 5,800 and 5,300, respectively. However, the centerline mean velocity for the higher level TKE reaches zero earlier, at x/D = 80, 50 and 30 for Re = 10,600, 5,800 and 5,300, respectively. The point where the jet centerline velocity reaches zero is indicative of the location at which the jet no longer "exists." For the case of a jet in the background turbulence at Re = 5,300, the measured mean velocities appear to fall to negative values far downstream. This may be due to experimental error, which could be caused by a combination of drift in the hot-film calibration and inaccuracies related to the subtraction of the (moving) probe's translational velocity.

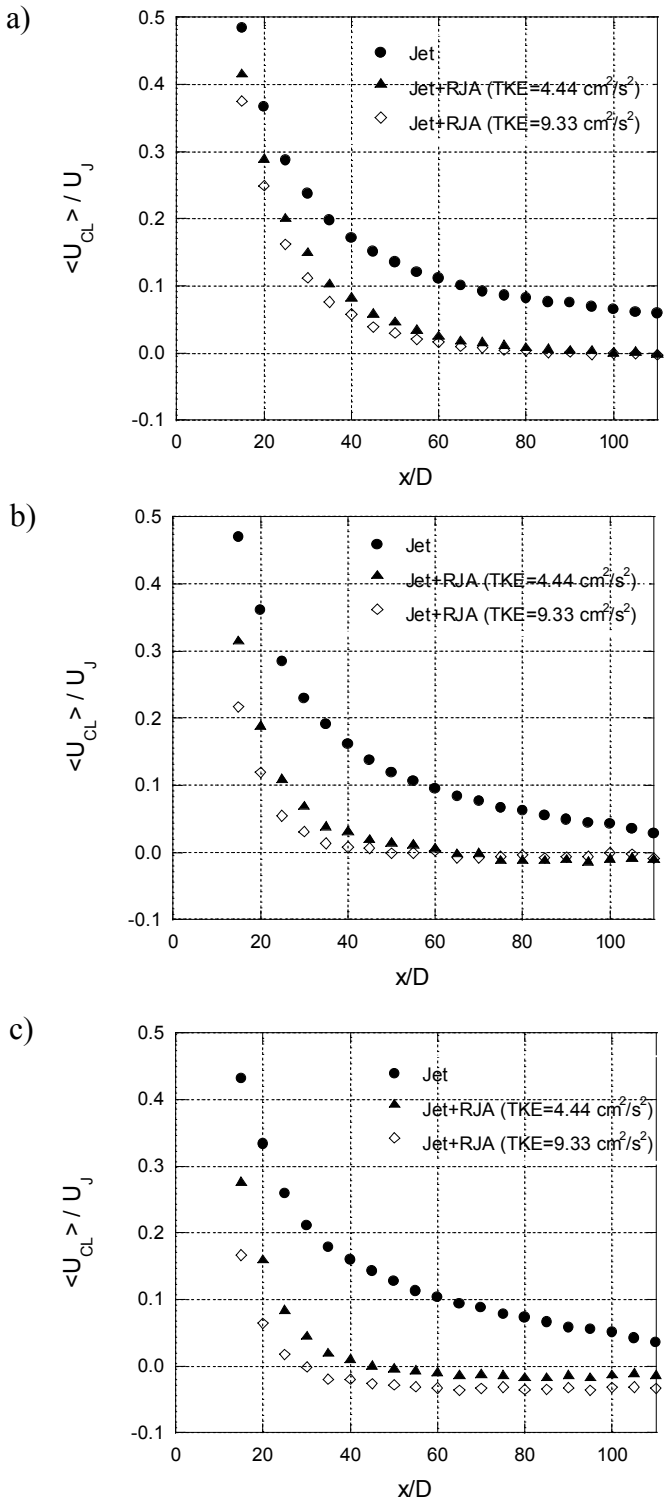

Figure 5.12 The effect of background turbulence on the downstream evolution of the mean axial velocity of an axisymmetric turbulent jet: a) Re = 10,600, b) Re = 5,800, and c) Re = 5,300. Linear-linear coordinates.

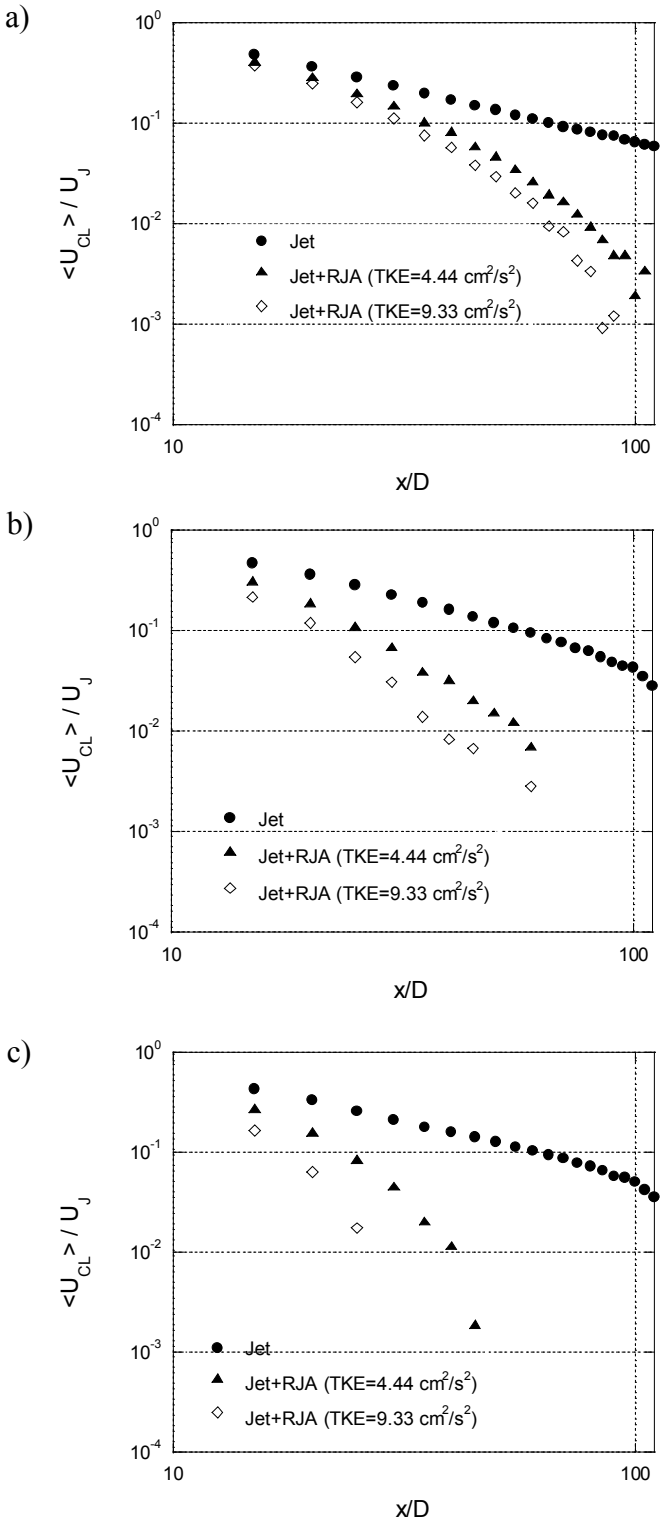

Figure 5.13 The effect of background turbulence on the downstream evolution of the mean axial velocity of an axisymmetric turbulent jet: a) 10,600, b) 5,800, and c) 5,300. Log-log coordinates.

	Jet in quiescent	Jet+RJA (TKE = 4.44 cm^2/s^2)	Jet+RJA (TKE = 9.33 cm^2/s^2)
Re = 10,600	$x^{-1.06}$	$x^{-1.83}$, for $x/D \leq$ 50	$x^{-2.13}$, for $x/D \leq$ 50
Re = 5,800	$x^{-1.17}$, for $x/D \leq$ 60	$x^{-2.50}$, for $x/D \leq$ 45	$x^{-3.38}$, for $x/D \leq$ 40
Re = 5,300	$x^{-1.06}$, for $x/D \leq$ 60	$x^{-2.57}$, for $x/D \leq$ 30	$x^{-4.34}$, for $x/D \leq$ 25

Table 5.3 Decay constants for jet in both quiescent and turbulent backgrounds.

The mean axial velocity profile was measured along the radius of the jet in quiescent and turbulent backgrounds. The radial profiles of the jet at Re = 10,600 at x/D = 20, 30, 40 and 50 are shown in Figure 5.14. It can be seen that the ambient turbulence results in more rapid decay of the jet with lower mean velocities across the radial profile. The decay becomes more noticeable farther downstream. Figure 5.15 shows the mean axial velocity profile at Re = 5,800. We can see that after x/D = 30 the jet profile is distorted and is relatively flat when in the presence of background turbulence, indicating that the organized jet structure has been destroyed. Radial profiles were not measured at Re = 5,300 due to lack of time given the closure of Environmental Hydraulics Laboratory for renovations.

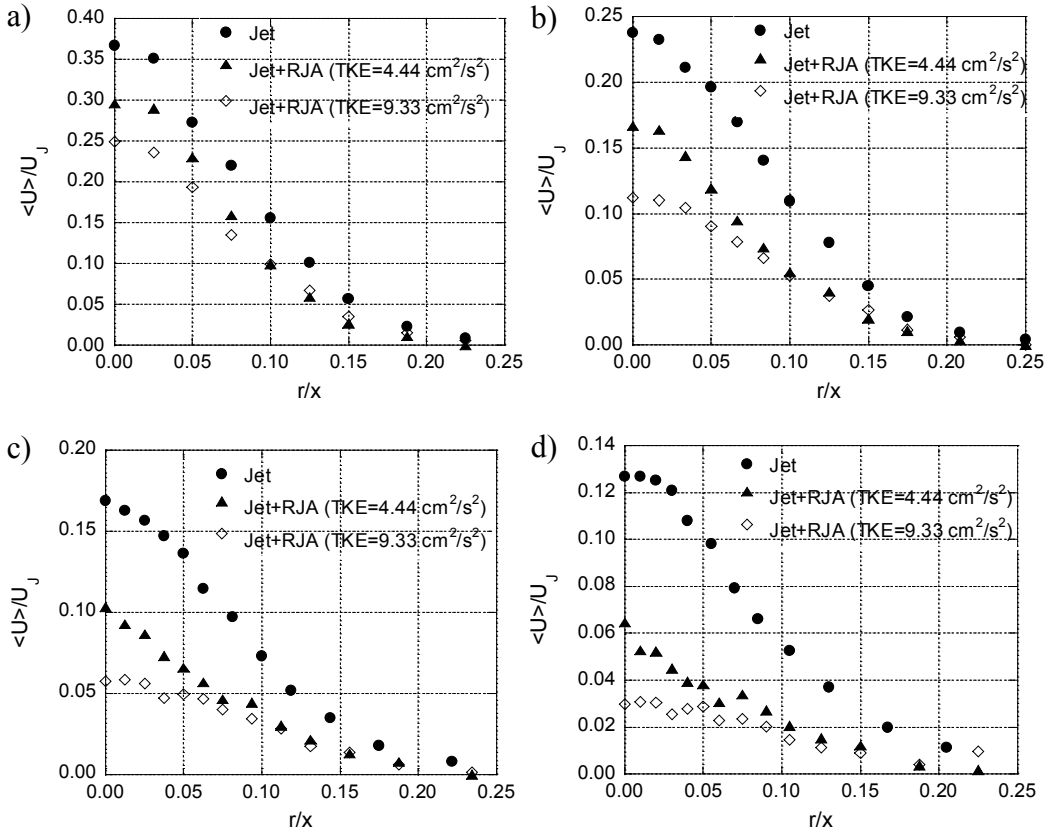

Figure 5.14 The effect of background turbulence on the mean axial velocity profile of an axisymmetric turbulent jet at *Re* = 10,600: a) *x*/*D*=20, b) *x*/*D*=30, c) *x*/*D*=40, and d) *x*/*D*=50.

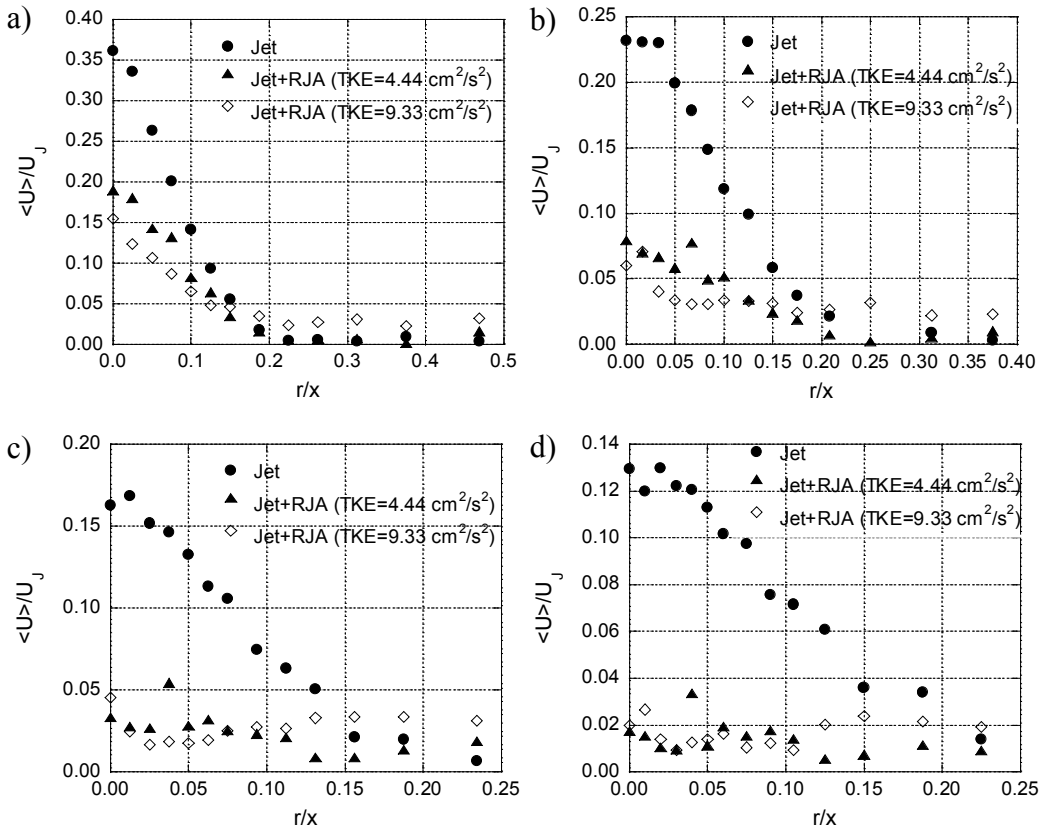

Figure 5.15 The effect of background turbulence on the mean axial velocity profile of an axisymmetric turbulent jet at *Re* = 5,800: a) *x*/*D*=20, b) *x*/*D*=30, c) *x*/*D*=40, and d) *x*/*D*=50.

Figure 5.16 shows the mean radial velocity (V) profile measured along the radius of the jet in quiescent and turbulent backgrounds. Radial profiles at x/D = 35, 42.5, 50, 60 and 75 are presented. The measurements were only conducted at Re = 10,600 using the ADV. In contrast to the mean axial velocities, the mean radial velocities increase in the presence of background turbulence (most notably closer to the edges of the jet). In addition, the jet is wider in the presence of background turbulence, as already observed for the mean axial velocity profile and to be quantified below. The mean radial velocities at the edges of the jet (in a quiescent background) are negative. In the presence of background turbulence, the mean radial velocities become less negative at the edges (where the negative radial velocities result in entrainment into the jet), however the negative velocity regions cannot be seen in the profiles of $x/D \geq 50$ as the measurements were only conducted up to r/x = 0.3 (which was not far enough in the radial direction). Negative radial velocities at the edges of the jet in the presence of background turbulence indicate that the fluid is being entrained into the jet. Therefore, the mass flow rate is expected to increase with the downstream distance in the presence of the background turbulence. However, less negative velocities result in lower entrainment into the jet, as will be shown in measurements of mass flow rate in Figure 5.18. In addition, the radial velocities do not significantly change close to the centerline in the presence of background turbulence, in contrast with the radial velocities away from the centerline which increase in the presence of ambient turbulence. The difference between the radial velocities at the edges of the jet in the presence of background turbulence and the radial velocities at the edges of the jet in quiescent background also increases from x/D = 35 to x/D = 75. Furthermore, the high-TKE background results in higher radial velocities, especially close to the edges of the jet, when compared to the low-TKE background.

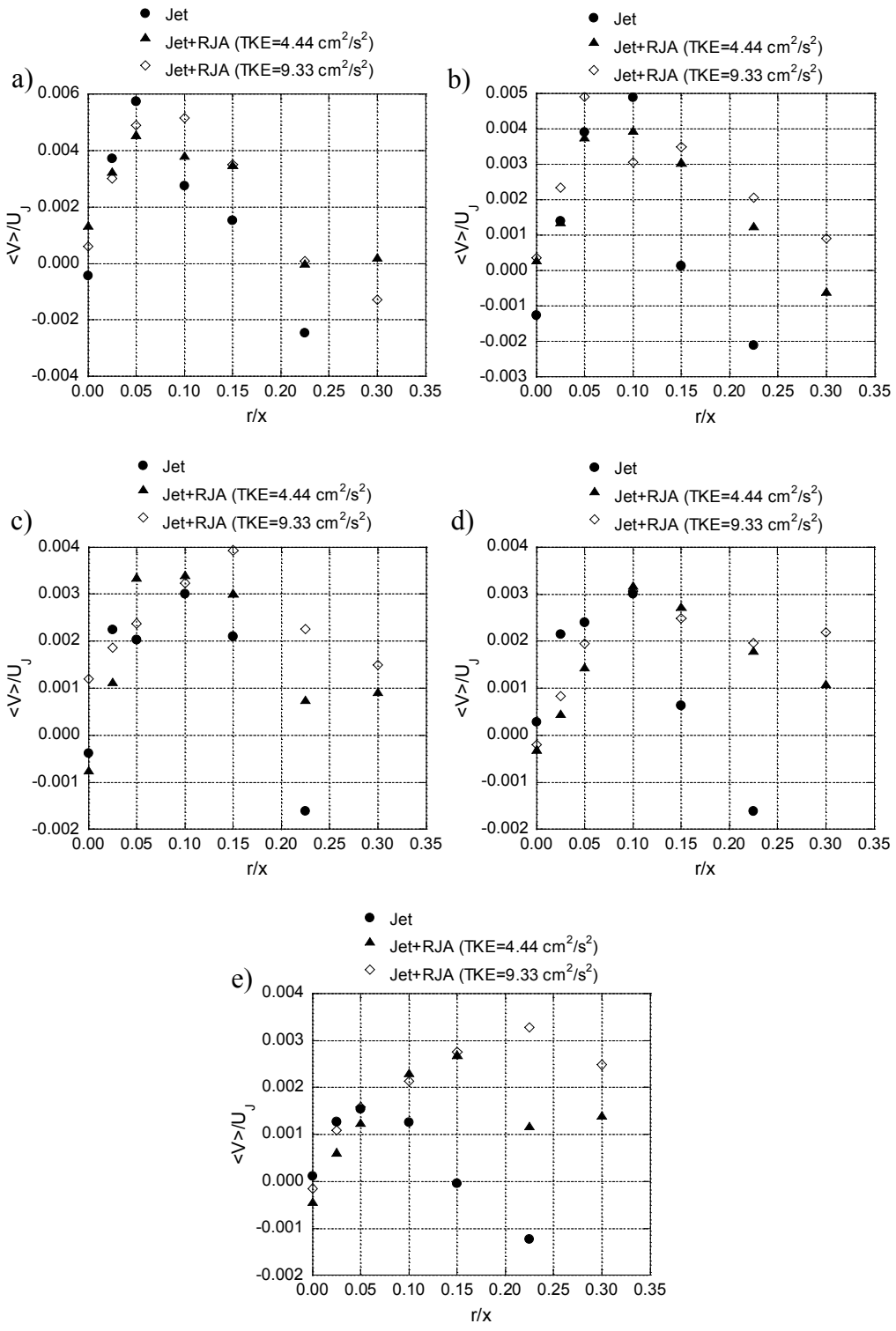

Figure 5.16 The effect of background turbulence on the mean radial velocity profile of an axisymmetric turbulent jet at *Re* = 10,600: a) *x*/*D*=35, b) *x*/*D*=42.5, c) *x*/*D*=50, d) *x*/*D*=60, and e) *x*/*D*=75.

The downstream evolution of the half-width of the jet in quiescent and turbulent backgrounds is shown in Figure 5.17. The measurements were only conducted at Re = 10,600 using the ADV. The solid and dashed lines in these graphs correspond to the integral length scales of the background turbulence for the low- and high-TKE cases, respectively. The integral length scales of the background turbulence were measured by the flying hot-film anemometry. The jet in a quiescent background grows linearly with the downstream distance, as predicted. However, in the presence of background turbulence, the jet becomes moderately wider, and as the level of background turbulence increases, the width of the jet also increases. Furthermore, the evolution of the jet half-width in the presence of external turbulence is no longer linear and exhibits power-law growth as $\sim x^{1.5}$ and $\sim x^{1.7}$ for the low and high-TKE backgrounds, respectively. The length scale of the jet is smaller than that of the background turbulence at $x/D \leq 35$ (not shown). At x/D = 35, they become of similar magnitude. Farther downstream, the length scale of the jet grows and becomes almost one order of magnitude larger than that of the background turbulence (at x/D = 75). Therefore, it is expected that the effect of length scale of the background turbulence on the jet is more noticeable closer to the jet exit ($x/D \leq 35$), and reduces with increasing downstream distance.

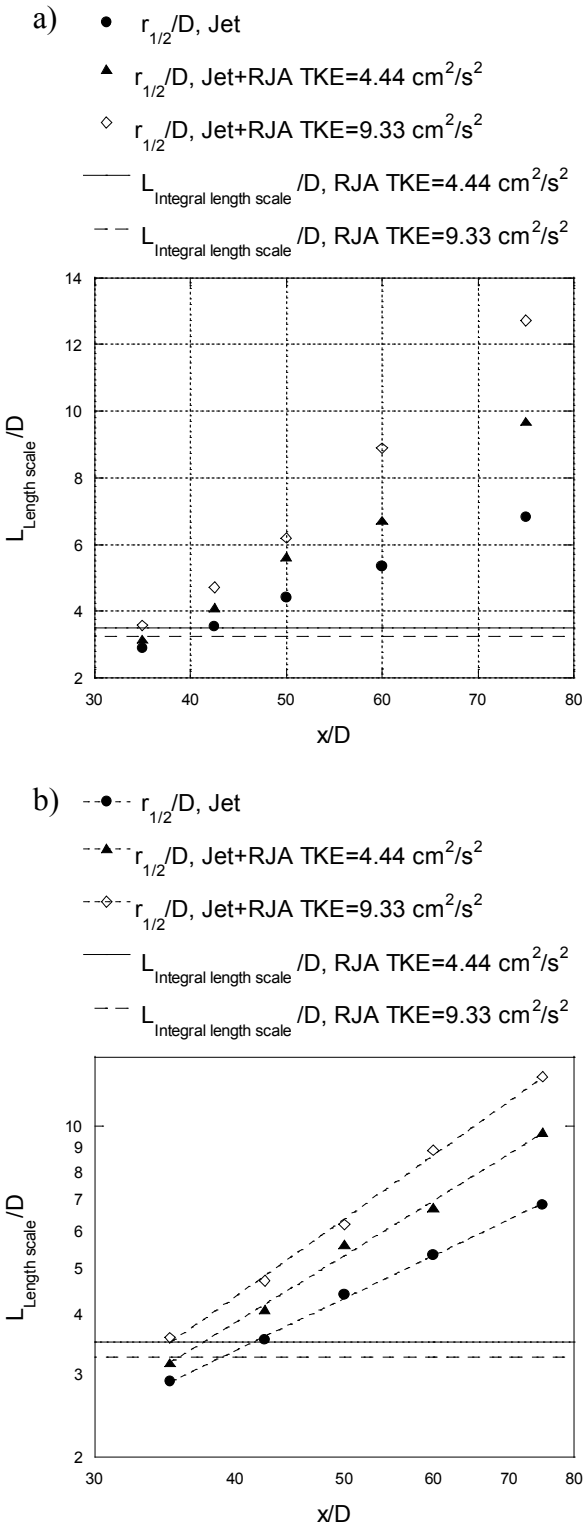

Figure 5.17 The effect of background turbulence on the downstream evolution of the half-width of an axisymmetric turbulent jet (*Re* = 10,600). a) Linear-linear coordinates. b) Log-log coordinates.

As mentioned earlier, the background turbulence decreases the mean axial velocity of the jet. If entrainment is proportional to the characteristic velocity of the jet (Morton *et al.* 1956), then a decrease in centerline velocity would imply a decrease in the rate of entrainment. Applying this argument to the present results would imply that ambient turbulence should result in a decrease in the (near-field) jet entrainment. This can be verified by calculating the mass flow rate based on the axial velocity profiles.

By integrating the area under the mean velocity profiles, mass flow rates were calculated. The downstream evolutions of the mass flow rates (normalized by the mass flow rate at the nozzle exit, m_0), measured in quiescent and turbulent backgrounds by ADV, are plotted in Figure 5.18. We observe that the presence of background turbulence serves to decrease the mass flow rate of the jet (at a given downstream distance), from which it can be inferred that the entrainment is also reduced. This suggests that the background turbulence may break up the large-scale jet structure, decreasing entrainment by engulfment.

The measured jet entrainment rate (*i.e.,* the slope of the curve) in a quiescent background is 0.34. In the presence of background turbulence, our experiments indicate that the entrainment rate of the jet remains constant for a given level of background turbulence (for the limited experimental conditions studies herein). However, the entrainment rate in the presence of background turbulence is lower than that in a quiescent background, and its magnitude appears to decrease with increased intensity of the background turbulence – the rate of entrainment decreases from 0.19 (for the low-TKE background) to 0.16 (for the high-TKE).

The entrainment rate is proportional to the entrainment velocity (U_α, the velocity at the edges of the jet) and the width of the jet. The entrainment velocity is related to the centerline mean velocity by the entrainment coefficient, α, *i.e.*, $U_\alpha = \alpha\langle U_{CL}\rangle$. The width of the jet can also be estimated by its half-width. As $dm/dx = 2\pi\, r_{½} U_\alpha = 2\pi\, r_{½}\langle U_{CL}\rangle\alpha$, and dm/dx is constant for the jet in both quiescent and turbulent backgrounds, therefore $\alpha \propto 1/(r_{½}\langle U_{CL}\rangle)$. Subsequently, the entrainment

coefficient (in the power-law decay region) of the jet at Re = 10,600 in low- and high-TKE backgrounds is proportional to $x^{0.3}$ and $x^{0.4}$, respectively.

Lastly, it is worth mentioning that the effect of a turbulent background on the mass flow rate of a jet is observed farther upstream when the turbulent kinetic energy of the background flow is increased. At x/D = 35, the values of m/m_0 for the quiescent background and the low-TKE background are similar, whereas m/m_0 for the high-TKE background is already much smaller than that observed for a jet in a quiescent background (at the same downstream position). We hypothesize that the effects of the background turbulence on the jet are most significant when the RMS velocities of the background turbulence are larger than the RMS velocities of the jet.

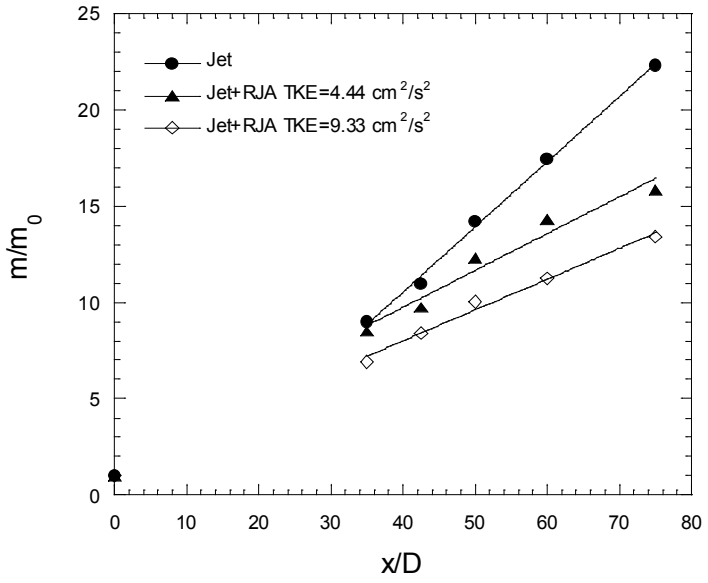

Figure 5.18 The effect of background turbulence on the downstream evolution of the mass flow rate of an axisymmetric turbulent jet.

The effect of background turbulence on the RMS axial velocity of the jet at Re=10,600, 5,800 and 5,300 when issued in two different turbulence levels is plotted in Figure 5.19. The solid and dashed lines in these graphs correspond to the RMS velocity of the background turbulence for the low- and high-TKE cases,

respectively. It is expected that the effect of background turbulence on the jet should be a function of the relative magnitude of i) the RMS velocities, and ii) the integral length scales, of the jet and background turbulence. These results show that the RMS axial velocity of the jet increases in the presence of a turbulent background. In addition, the effect of external turbulence seems to be higher close to the jet exit, (*i.e.*, the percentage difference between the RMS velocity of the jet in the quiescent and turbulent backgrounds decreases with the downstream distance). As was shown earlier, the integral length scale of the jet is less than that of the RJA close to the jet exit, *i.e.*, $x/D \leq 35$, but grows larger than that of the RJA with downstream distance. Therefore, the RMS velocity field is more strongly affected near the jet exit where the integral length scale of the jet is lower than (or similar to) that of the background turbulence. Furthermore, the RMS velocities of the jet in the high-TKE background are higher compared to those of the jet in low-TKE background close to the jet exit, *i.e.*, $x/D \leq 35$ for Re = 10,600, and $x/D \leq 15$ for Re = 5,800 and 5,300. This trend changes in the near-field (after the initial development region of the jet) where the RMS velocities of the jet in the low-TKE background are higher than those of the high-TKE background, *i.e.*, $40 \leq x/D \leq 100$ for Re = 10,600, and $20 \leq x/D \leq 45$ for Re = 5,800 and 5,300. This is in contrast with the notion of superposition of the jet and background turbulence. Finally, far downstream (where the measured RMS velocities are close to those of the background turbulence), the RMS velocities of the jet in the high-TKE background are higher than those of the low-TKE background. Where the RMS velocities of the jet are equal to the RMS velocities of the background turbulence, it is expected that the jet does not exist and the turbulence measured was that of the background turbulence. Furthermore, it can be observed that the RMS velocities decrease to background turbulence levels at a point farther downstream than where the mean velocity reached zero. Given that the jet RMS velocities being measured farther downstream than the mean velocities indicates that all that remains is a volume of turbulent flow with no mean velocity and therefore no jet structure. As can be seen in Figure 5.19a), the jet is not totally destroyed by the background turbulence within the measurement range for the higher Reynolds

number jet. However, at lower Reynolds numbers, the RMS velocities asymptote to the RMS velocities of the RJA indicating that the jet was destroyed by the background turbulence within the measurement range.

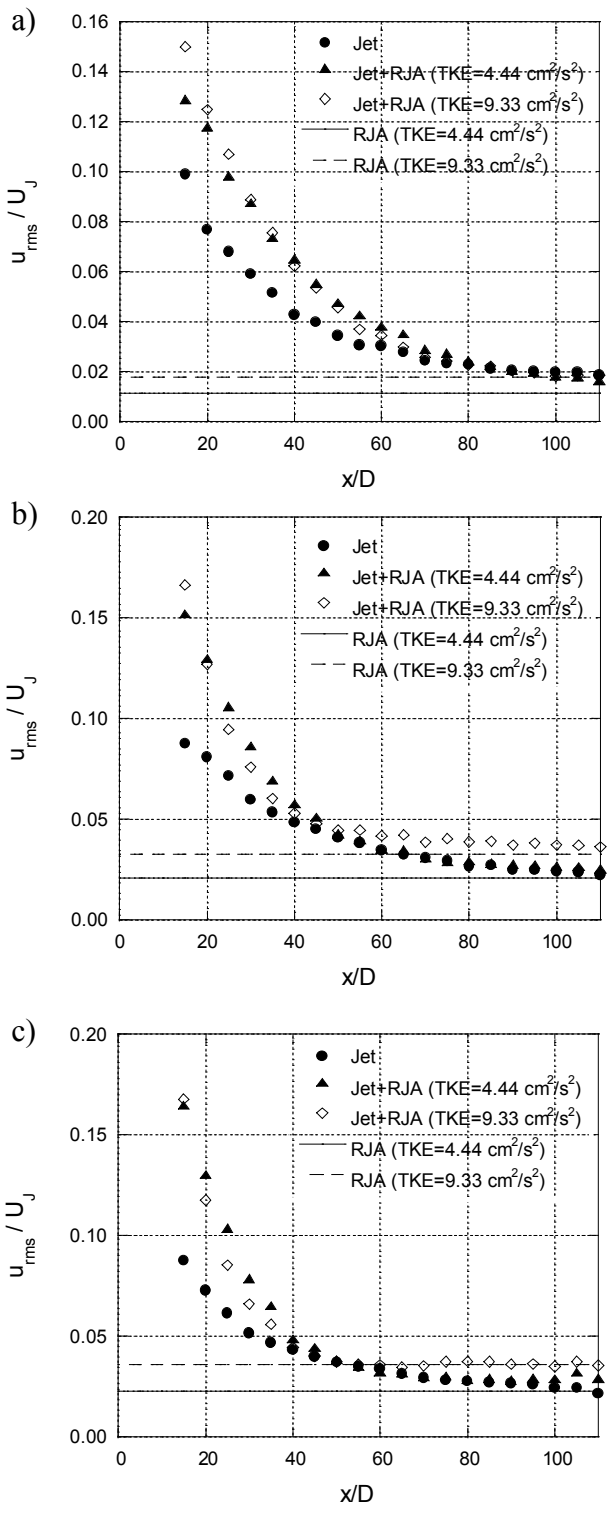

Figure 5.19 Downstream evolution of the RMS axial velocities at the centerline of the jet (normalized by the exit velocity of the jet, U_J) in quiescent and turbulent backgrounds: a) 10,600, b) 5,800, and c) 5,300.

Figure 5.20 and Figure 5.21 show the RMS axial velocity profiles measured along the radius of the jet in quiescent and turbulent backgrounds at *Re* = 10,600 and Re = 5,800, respectively. Radial profiles are presented at x/D = 20, 30, 40 and 50. It can be seen that the RMS velocities increase in the presence of background turbulence. The RMS velocities of the jet issued in the high-TKE background are higher than those of the jet in the low-TKE flow, at $x/D \leq 35$ for *Re* = 10,600 and $x/D \leq 15$ for *Re* = 5,800 (not shown) and at the edges of the jet (where the background turbulence is dominant). Downstream of these initial regions, the RMS velocities of the jet are higher for the low-TKE. Finally, when the jet structure is disrupted and the external turbulence is dominant, *e.g.*, $x/D \geq 50$ for *Re* = 5,800, the RMS velocities measured in jet in high-TKE are higher.

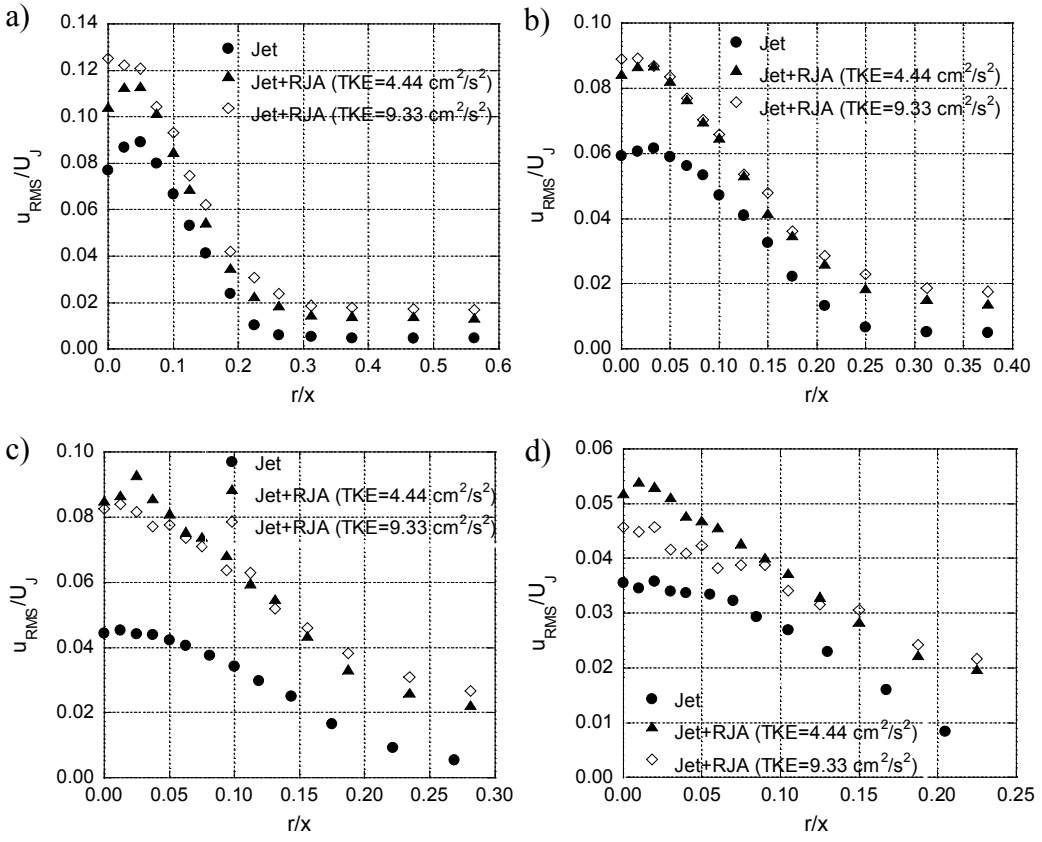

Figure 5.20 The effect of background turbulence on the RMS axial velocity profile of an axisymmetric turbulent jet at *Re* = 10,600: a) x/D=20, b) x/D=30, c) x/D=40, and d) x/D=50.

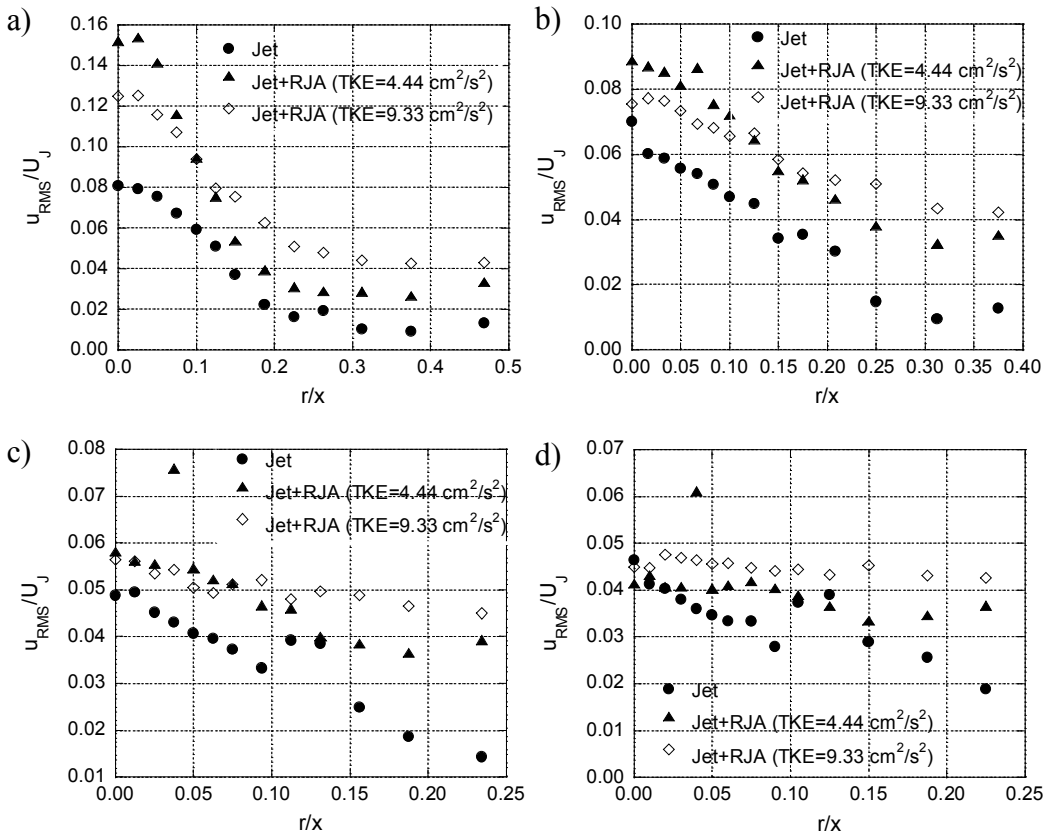

Figure 5.21 The effect of background turbulence on the RMS axial velocity profile of an axisymmetric turbulent jet at *Re* = 5,800: a) *x*/*D*=20, b) *x*/*D*=30, c) *x*/*D*=40, and d) *x*/*D*=50.

The profile of the local turbulence intensity ($u_{rms}/\langle U(r)\rangle$) at x/D = 30 for *Re* = 10,600 is plotted in Figure 5.22. The turbulence intensities increase in the presence of background turbulence (as expected from the lower mean axial velocities and higher RMS axial velocities presented earlier). The turbulence intensities of both the jet in a quiescent background and the jet in the background turbulence increase from the centerline toward the edge of the jet, as does the difference in turbulence intensities between the jet in quiescent and turbulent backgrounds.

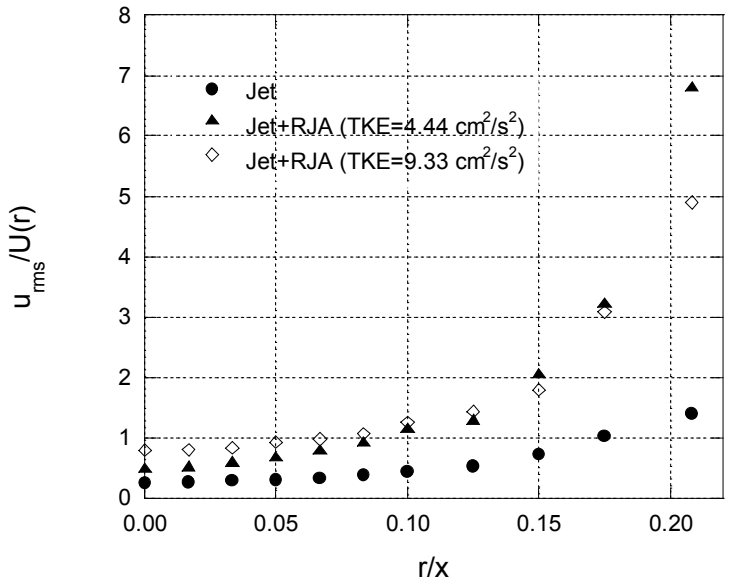

Figure 5.22 The effect of background turbulence on the profile of the local turbulence intensities $x/D = 30$, $Re = 10{,}600$.

5.3 Discussion

5.3.1 Acoustic Doppler Velocimetry

For the flows considered herein, the ADV is a relatively accurate instrument for mean velocity measurements. The RMS velocities measured along the x- and y-directions of the probe (or u and v horizontal velocity components) are significantly overestimated while the vertical RMS velocity, which is measured in the z-direction of the probe, agrees well with other studies. Among the noise-reduction methods suggested in the literature, that of Hurther and Lemmin (2001) improved the turbulence statistics, however the corrected RMS velocities measured by the ADV were still higher than those measured by well established turbulence measurement techniques. We also presented a method for improving the turbulence statistics. This method improved the data and can be used in the axisymmetric flows or if measurements with the probe in two different orientations are conducted. However, in general further work needs to be done to improve the accuracy of the turbulence statistics measured with the ADV. In

addition, the turbulence statistics measured with the ADV should not be used without post-processing. Although, the vertical velocity measured by the ADV is relatively accurate, and thus the z-direction of the probe can be used to measure correct turbulence statistics, orienting the probe so that the z-direction of the probe is aligned against the direction of the flow, *e.g.* along the jet axis, may result in a significant flow disturbance.

5.3.2 Relationship to Previous Studies

Hunt (1994) theoretically reasoned that an increased mass or momentum flow rate of a jet will increase entrainment, while any tendency of the jet to break up into distinct eddies will decrease the entrainment. Ambient turbulence disrupts the jet structure and hence is expected to decrease the entrainment into the jet. This hypothesis was confirmed experimentally by Gaskin *et al.* (2004) for a plane jet in a shallow co-flow with increased turbulence in the co-flow produced by placing ribs across the channel bed. Measurements of concentration and velocity both indicated a decrease in entrainment in the presence of ambient turbulence as in the present study. The background flow in this study was more complex as the ribs created a turbulent intensity which fluctuated about the mean (with one standard deviation being 15% of the mean value) along the jet. In addition, mean flow advection was present and the shallowness of the channel affects the jet structure.

There exist a few previous experimental studies of a jet/plume issuing into the turbulence (with approximately zero-mean flow) generated by an oscillating grid. In these studies, the jet/plume axis was perpendicular to the plane of the oscillating grid, therefore having background turbulence level increasing in the downstream direction of the jet/plume (*i.e.*, as jet/plume turbulence level decreased) (Figure 5.23). The mean and RMS velocities of the jet decay as x^{-1} in a quiescent background. The RMS velocity of the oscillating grid turbulence decays as x^{-1} away from the grid. As a result the background turbulence is not

homogeneous along the jet: close to the jet exit, the background turbulence is weak, while close to the grid, the intensity of the background turbulence is high.

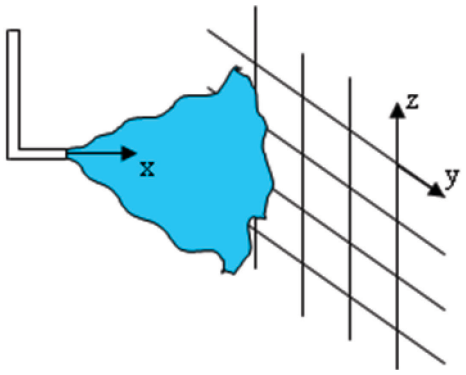

Figure 5.23 Jet issuing perpendicular to the plane of the oscillating grid.

Ching *et al.* (1995) studied a plume in the presence of background turbulence. They showed (by dye visualization and laser Doppler velocimetry) that the plume can be destroyed when the convective velocity of the plume is of the same order as the RMS velocity of the background turbulence. At the breakup location an increase in the spreading rate was observed. The effect of background turbulence generated by an oscillating grid on a jet was studied by Guo *et al.* (1999). Using a similar experimental setup as that of Ching *et al.* (1995), they showed (using the video-based Digimage processing technique) that the jet is destroyed when the RMS velocity of the background turbulence reaches about 0.125 of the centerline jet velocity. They observed that as a result of the jet breakup, the spreading angle increases and hypothesized that therefore the mixing and dilution of the jet is enhanced.

In similar studies Guo *et al.* (2005) and Cuthbertson (2006) studied a momentum-driven jet and a buoyancy-driven jet, respectively in the presence of background turbulence generated by the oscillating grid using flow visualization and the particle image velocimetry (PIV) technique. They showed that the jet is destroyed by the background turbulence when the RMS velocity of the jet is of the same order as the RMS velocity of the background turbulence.

The effect of background turbulence generated by the oscillating grid on a round jet was studied by Law *et al.* (2001). Their PIV measurements showed that in the presence of background turbulence, the downstream evolution of the jet is similar to that of the jet in a stagnant ambient up to $x/D = 55$ (the oscillating grid was located at $x/D = 78$). The effect of background turbulence on the jet then becomes significant as the jet approaches the oscillating grid ($x/D \geq 55$). They showed that in the presence of background turbulence, when close to the grid i) the jet velocity decays more rapidly, ii) the jet's spreading rate increases, iii) the rate of entrainment of the jet increases, and iv) the fluctuations near the centerline of the jet increase. An increased decay of mean properties was also found by Gaskin and Wood (1993) for an advected line thermal in turbulence created with a bubble jet array.

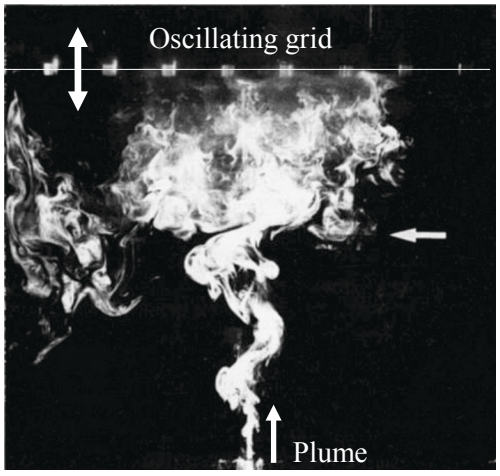

Figure 5.24 The evolution of a plume in the presence of background turbulence (from Ching *et al.*, 1995).

The results of the studies above must be interpreted in light of the experimental setup, in which the jet/plume axis was perpendicular to the plane of the oscillating grid, resulting in background turbulence level increasing in the downstream direction of the jet/plume (*i.e.*, as jet/plume turbulence level decreased). As a result, close to the jet exit, the background turbulence is weak and there is no effect on the jet structure as was seen by Law *et al.* (2001).

However, close to the grid, the intensity of the background turbulence is higher than that of the decaying jet and the background turbulence was observed to have a significant influence on the jet.

Law *et al.* (2001) showed that in the presence of background turbulence the entrainment rate of the jet increases. However in an experimental setup in which the jet/plume is perpendicular to the plane of the oscillating grid, the jet/plume is blocked by the oscillating grid resulting in accumulation of mass near the grid (as seen in the similar experimental setup of Ching *et al.* (1995) in Figure 5.24) and this is therefore the probable reason for the sudden increase of spreading rate and entrainment rate close to the grid. The problems with this experimental design render the conclusions thus obtained ambiguous. In the experimental setup of the present study, the plane of the random jet array generating the background turbulence was parallel to the jet axis and therefore the turbulence intensity of the background turbulence was constant (homogeneous) along the jet axis. The measurements of the mass flow rate in the presence of homogeneous background turbulence showed that the entrainment rate of the jet was lower when compared to that of the jet in a quiescent background.

There has also been a study on jet in open channel flow in which increases in ambient turbulence were obtained by increasing the roughness of the bed. Wright (1994) studied the previous experimental data of jets in shallow co-flows with different bed roughnesses. He showed that the entrainment into the jet increases as the free-stream turbulence (which increases with the bottom roughness) increases. (The free-stream turbulence level was not available for some of the data that was analysed by Wright (1994).) He proposed the theory of superposition of jet entrainment and ambient turbulence entrainment, which predicts an increase in the entrainment into the jet in the presence of ambient turbulence. However, the experimental results presented by Wright (1994) showed significant scatter especially in the case of a low ratio of jet velocity to ambient velocity.

5.3.3 Entrainment Mechanism

A jet discharged into a flow entrains fluid and hence increases its mass flow rate in the downstream direction. There are two proposed entrainment mechanisms for the near-field (which starts after the initial development region) of the jet issuing into a quiescent background. These entrainment mechanisms are engulfment and nibbling.

Engulfment is a large-scale inviscid process in which large volumes of ambient fluid are drawn into the jet by large eddies. Subsequent mixing is carried out by viscous diffusion of vorticity (*e.g.*, Townsend, 1956; Brown and Roshko, 1974). The existence of engulfment is confirmed by flow visualization and measurements of the scalar concentration field by Dahm and Dimotakis (1987, 1990). They confirmed that the entrainment and mixing processes in the near-field of a turbulent jet can be characterized by scales approximately equal to the local large scales of the flow (Morton *et al.*, 1956). The instantaneous concentration profiles from their work also show that the (unmixed) ambient fluid was transported deep into the jet. This is postulated as another proof for large-scale entrainment.

Nibbling is a small-scale viscous process that occurs by small-scale eddies at the very thin interface (on the order of the Kolmogorov microscale) between turbulent and non-turbulent flows. This interface or "laminar super-layer" plays a significant role in transmitting the vorticity to irrotational fluid by tangential viscous forces (and not by macroscopic shear forces, Corrsin and Kistler, 1955). Although there exists a debate as to the relative importance of the two processes, recent direct numerical simulations by Mathew and Basu, (2002) have shown nibbling to be the dominant entrainment process. This study has also been corroborated experimentally by Westerweel *et al.* (2008), who found that nibbling at the interface is effected by small scale eddies and that the engulfed mass consists of less than 10% of the total entrained mass. Westerweel *et al.* (2008) also characterized this laminar super-layer as having a thickness in the order of

the Taylor microscale. They analytically reasoned that since the engulfment is associated with the fluctuations in the enstrophy budget, and as the net contribution of engulfment to the enstrophy flux is small, then the engulfment does not contribute to the outward boundary entrainment velocity, E_b, ($E_b = -2V_i$, where V_i is the mean inward radial velocity at the jet interface).

Regardless of the entrainment mechanism, as long as scale similarity exists (as is the case in a self-similar jet), the overall rate of entrainment can be predicted by characteristic (large or small) scales of the flow. However when disrupted by an external turbulence, the jet is no longer self-similar. The change in the structure of the jet caused by the ambient turbulence can affect the mechanism of entrainment. Here, we hypothesize how the background turbulence can affect the entrainment mechanism.

The background turbulence affects the large-scale structure of the jet and results in a decrease in the entrainment rate. Therefore, the background turbulence should reduce the entrainment by engulfment. As shown in §5.2.2, the background turbulence results in: i) an increase in length and velocity scales of the large-scale eddies as shown by measurements of the half-width and RMS velocity, ii) a decrease in the mean axial velocity of the jet, and therefore faster jet decay, iii) a reduced rate of increase in the mass flow rate of the jet, and therefore, a decrease in the entrainment into the jet. These phenomena are consistent with the background turbulence reducing the entrainment by engulfment by modifications to the large-scale structure of the jet.

The background turbulence also affects the boundaries of the jet, therefore disrupting the entrainment by nibbling. For the case of the jet issuing into a quiescent background, Westerweel *et al.* (2008) detected discontinuities in the profiles of quantities such as conditional momentum flux and (mean and fluctuating) vorticity at the laminar super-layer (Figures 5.25 and 5.26 from Westerweel *et al.*, 2008). The discontinuity may vanish when the background turbulence is present, as the quantities such as vorticity asymptote to that of the background turbulence instead of jumping to zero. Therefore, the flux of vorticity

into the background turbulence should decrease compared to that in a quiescent background due to a lower gradient at the interface of the jet and the background fluid/flow. It is therefore hypothesized that, the entrainment by nibbling (resulting from diffusion of vorticity) may also be reduced in the presence of background turbulence.

The basic entrainment mechanism for the jet may change in the presence of background turbulence. No discontinuity was observed in RMS conditional velocities (Figure 5.26) and integral length scale (not shown) which exist on both sides of the super-layer, but these quantities eventually reach zero in the quiescent fluid (Westerweel *et al.*, 2008). In the presence of background turbulence, the RMS velocities and the integral length scale should also asymptote to those of the background turbulence. Therefore, the eddies with the intensity and the length scale of the order of those of the background turbulence dominate the interface. Consequently, entrainment by viscous diffusion at the interface (or laminar super-layer) is changed to turbulent diffusion by large-scale eddies in the presence of external turbulence. If (in the presence of the background turbulence) nibbling by small-scale eddies at the jet/ambient interface was the main entrainment mechanism, then the mass flow rate of the jet should have decreased, or at least not increased, with downstream distance. The observed, persistent increase of the mass flow rate of the jet issuing into a turbulent background with the downstream distance indicates that the entrainment is probably conducted by the large-scales or engulfment. This is consistent with the hypothesis of Westerweel *et al.* (2008) which states that when the external fluctuations are present, the basic structure of the jet changes and the entrainment process begins to be dominated by engulfment. However, drawing a solid conclusion regarding the mechanism of entrainment of the jet in the presence of background turbulence solely from the velocity field is not easy, and the information about the mixing of scalars transported within the jet would be of further benefit.

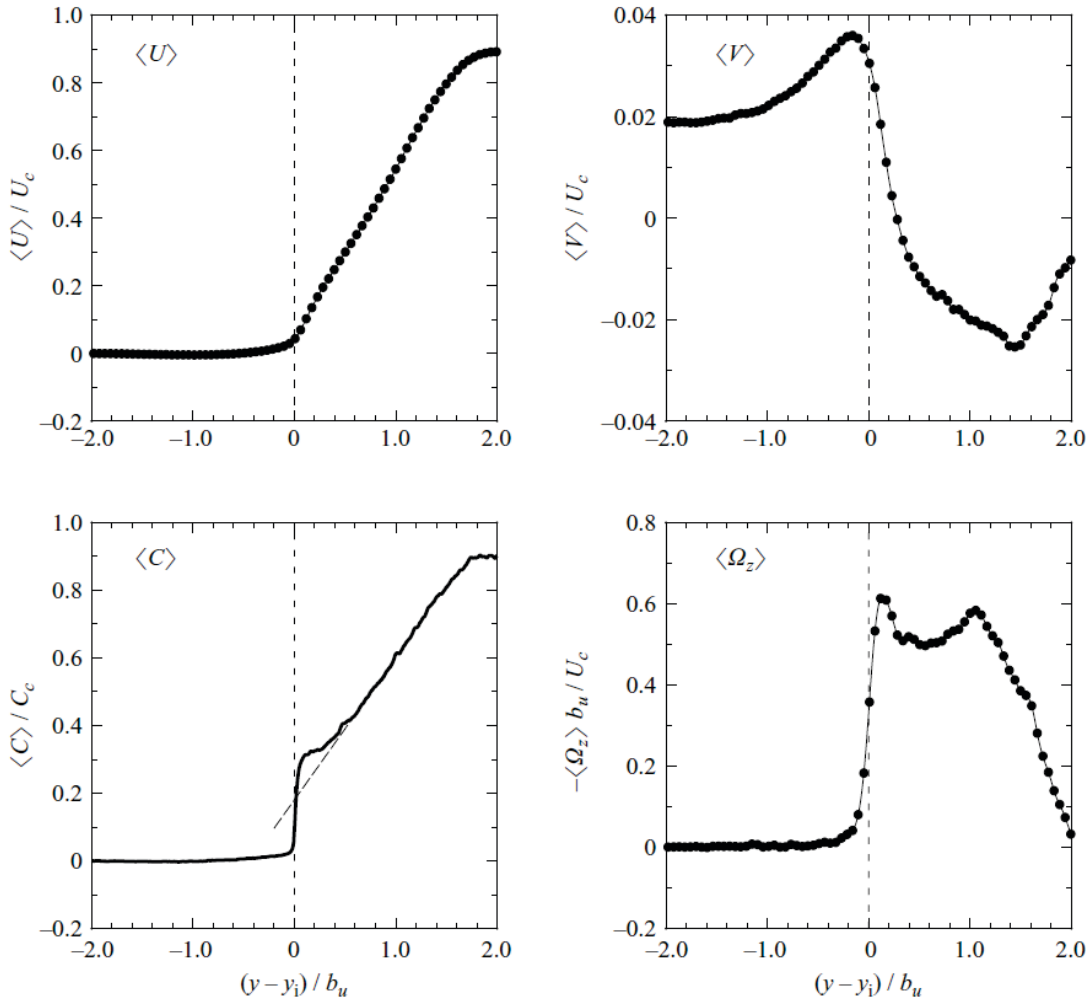

Figure 5.25 Conditional statistics from Westerweel *et al.* (2008). y - y_i is the distance from the interface and positive values on the x-axis are inside the jet and negative values are in the irrotational ambient fluid. b is the jet's half-width, C is the concentration and Ω_z is the (out-of-plane component of the) mean vorticity.

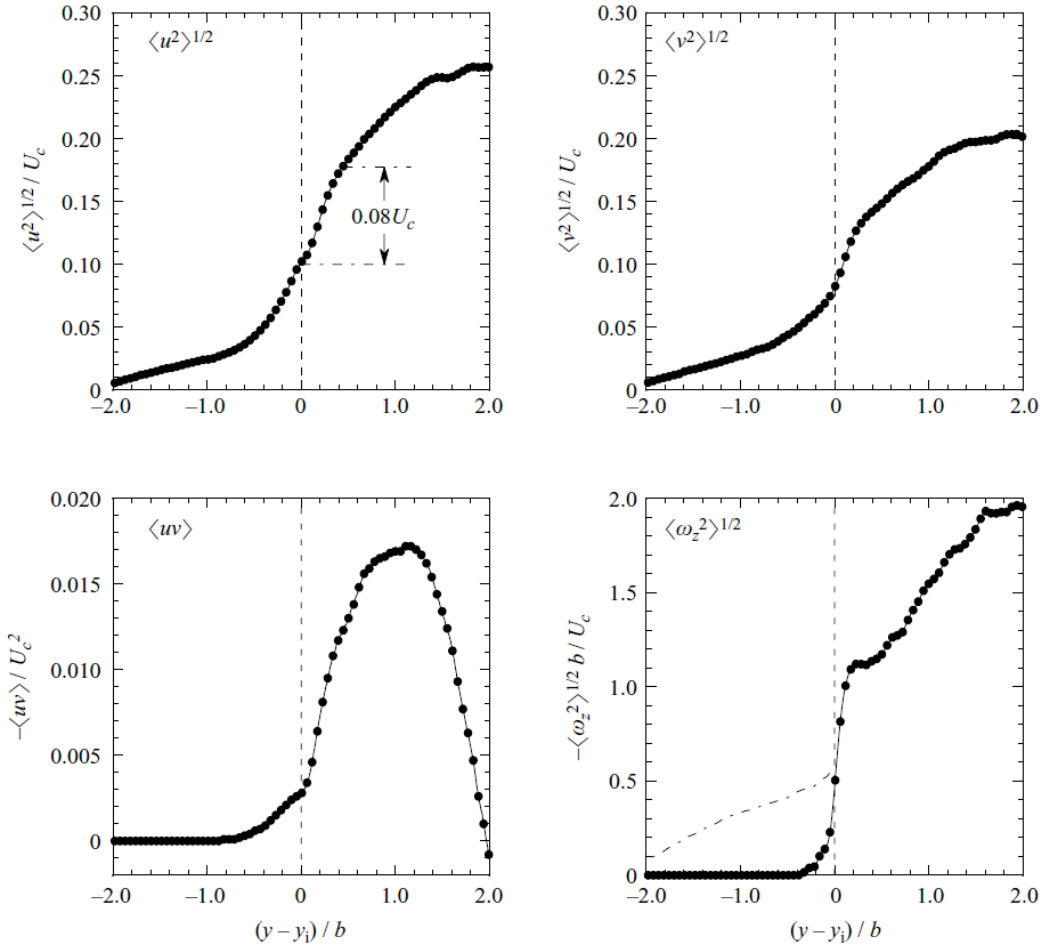

Figure 5.26 Conditional statistics (continued) from Westerweel *et al.* (2008). ω_z is the (out-of-plane component of the) vorticity fluctuation.

5.3.4 Breakup Location of the Jet

It can be argued that if the turbulent Reynolds number of the background turbulence were higher than the jet's Reynolds number, the jet structure would break up upon its arrival into the background flow. However, if the jet's Reynolds number is higher than the turbulent Reynolds number of the background turbulence, it would be reasonable to expect that the jet would develop downstream and its structure would be similar to a jet issued into a quiescent background (where the Reynolds number is zero). Downstream of the jet exit, when the RMS velocities of the jet become of the same order as that of the

ambient turbulence, the jet structure could break up into distinct eddies. At this point the mean velocity of the jet would approach zero, while the jet RMS velocities could be measured farther downstream compared to the mean velocities. At this stage, the dilution of the remainder of the jet would occur due to turbulent diffusion by the ambient turbulence.

Here, we attempt to predict the breakup location of the jet as a function of both the jet and background turbulence parameters. The effect of background turbulence on the jet is expected to be a function of i) the RMS velocities of both the background turbulence and that of the jet, ii) the integral length scales of both the background turbulence and that of the jet, and iii) the turbulent Reynolds numbers of the two, as well. As the turbulent Reynolds number of the jet is not constant and as i) $u_{rms\text{-}Jet} \propto U_{CL} \propto U_J$, and ii) $L_{Jet} \propto D$, the Reynolds number of the jet ($U_J D/\nu$) is used as a surrogate for the turbulent Reynolds number of the jet. Therefore, we define $Re_{T\text{-}RJA}/Re_{Jet} = u_{rms\text{-}RJA}L_{RJA}/U_J D$, which is the relative magnitude of the turbulent Reynolds number of the background turbulence to the jet Reynolds number.

The background turbulence initially affects the edges of the jet due to lower RMS velocities of the jet at its edges. Therefore, the breakup of the jet starts from the edges and moves towards the centerline. However, here the breakup location of the jet will be determined from the centerline velocities.

The threshold for the breakup location determined from the centerline mean velocity is defined as the position where the mean axial velocity reaches 1% of the exit velocity of the jet. Figure 5.27 plots the breakup location of the jet (found using the mean axial velocity measurements in §5.2.2) versus $Re_{T\text{-}RJA}/Re_{Jet}$. The data points on this graph correspond to the three different jet Reynolds numbers of 10,600, 5,800 and 5,300 issuing into turbulent backgrounds with TKE = 4.44 cm^2/s^2 and 9.33 cm^2/s^2. As seen in this graph, the breakup location monotonically moves towards the jet exit as the relative magnitude of the turbulent Reynolds number of the background turbulence to the jet Reynolds

number increases. Extrapolation of the results implies that at higher $Re_{T\text{-}RJA}/Re_{Jet}$ (~0.14), the jet breaks at its exit ($x/D = 0$).

Figure 5.28 plots the breakup location determined from the centerline RMS velocity versus $Re_{T\text{-}RJA}/Re_{Jet}$. The RMS velocity threshold is defined where the RMS velocity of the jet reaches 1.25 of that of the background turbulence. This threshold is defined higher than that of the mean velocity because the RMS velocity asymptotes to the level of background turbulence farther downstream than the location at which the mean velocity reaches zero. In contrast with Figure 5.27, with this definition the jet does not break up at $Re_{T\text{-}RJA}/Re_{Jet} = 0.04$. As can be seen in this graph, again a relatively higher turbulent Reynolds number of the background turbulence results in earlier breakup of the jet.

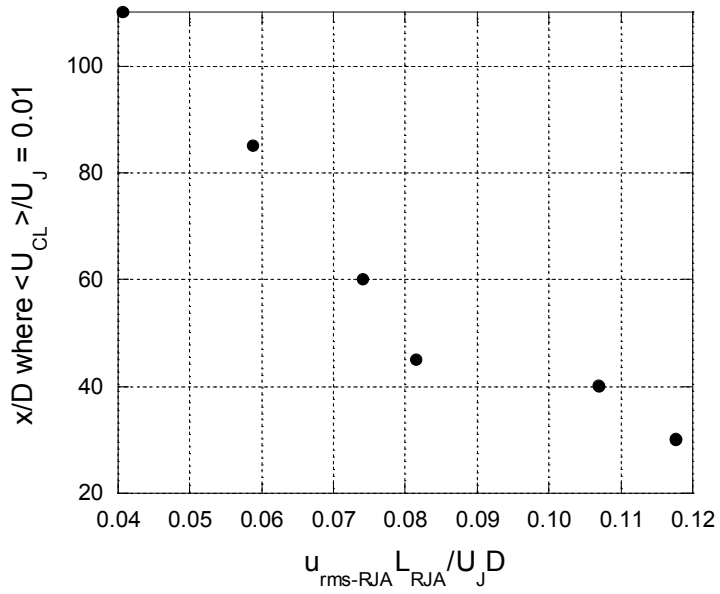

Figure 5.27 Breakup location of the jet determined from the mean velocity.

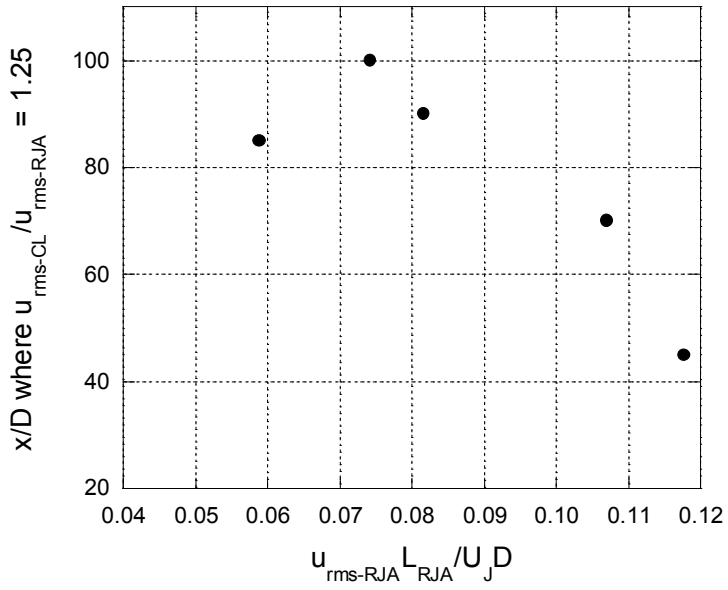

Figure 5.28 Breakup location of the jet determined from the RMS velocity.

The decay exponent (of the power-law decay region) of the centerline mean velocity of the jet is plotted versus $Re_{T\text{-}RJA}/Re_{Jet}$ in Figure 5.29. The decay exponent for the last point in this graph $Re_{T\text{-}RJA}/Re_{Jet} \approx 0.12$ may not be accurate as it was determined from only (the first) three data points, as the jet mean velocity had decreased to zero beyond that downstream distance. Without considering this point, the decay exponent decreases linearly (with the slope of about -23) with $Re_{T\text{-}RJA}/Re_{Jet}$. As expected the jet decays faster as the relative magnitude of the turbulent Reynolds number of the background turbulence to the jet Reynolds number increases.

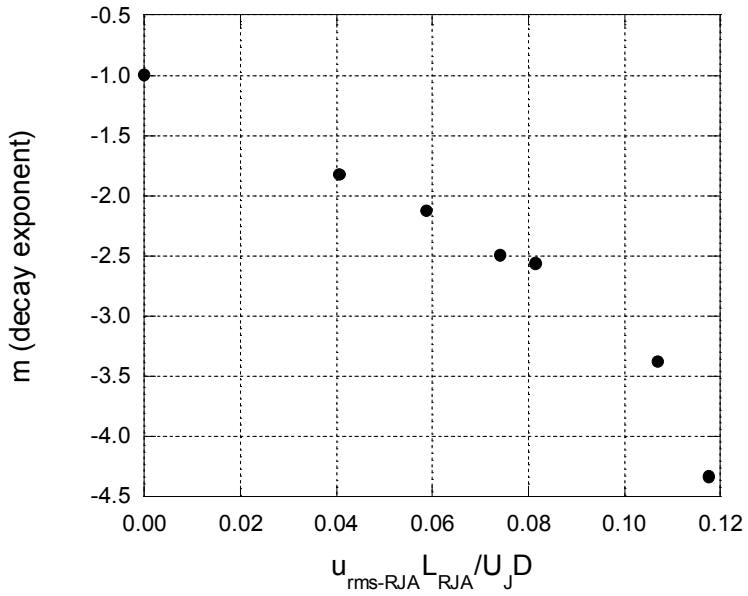

Figure 5.29 Decay exponents of the centerline mean velocity.

Chapter 6

Conclusions

6.1 Thesis Review

This thesis investigates the effect of different levels of background turbulence on the dynamics and mixing of a turbulent jet over a range of Reynolds numbers. The summary of each chapter is presented in this section.

- In Chapter 1, the topic of this thesis, the effect of background turbulence on the evolution of an axisymmetric turbulent jet is introduced. The motivation is to determine the effect of ambient turbulence on the dispersion of pollutants released into the environment in the form of a jet flow. The primary objective of this study is to experimentally investigate the effect of different levels of background turbulence on the velocity field of a turbulent jet at different Reynolds numbers. The secondary objective is to study the noise in turbulence measurements using the acoustic Doppler velocimeter (ADV) and thus improve the measured turbulence statistics. The organization of the thesis is outlined in the last section.

- Chapter 2 presents a literature review on axisymmetric turbulent jets, methods of generation of background turbulence in the laboratory, the effect of background turbulence on a jet/plume, and velocity measurement techniques. The axisymmetric turbulent jet issuing into a quiescent background is first reviewed. The variations of statistics such as mean velocities, Reynolds stresses of an axisymmetic turbulent jet as well as the variations of entrainment and mixing into an axisymmetic turbulent jet are discussed. The common means of generation of homogeneous, isotropic turbulence in the laboratory, the oscillating grid and the random jet array, are reviewed. Subsequently, the experimental studies on the effect of background turbulence generated by oscillating grid turbulence on a jet/plume, as well as the theories on the entrainment mechanisms, are presented. In the final section, the literature review on the measurement techniques used herein, acoustic Doppler velocimetry and hot-film/wire anemometry, are presented.

- Chapter 3 provides details of the experimental setup, in which a turbulent jet issues into a quiescent or turbulent background. The turbulent background flow is created in a tank with a random jet array (RJA), and the apparatus and its control algorithms are described. The turbulent jet setup and its components, including the water supply, flow control devices and connections are discussed in detail. The water filtration system and the heater used to keep the water clean at a constant temperature for the flying hot-film anemometry experiments are explained. The two velocity measurement techniques, acoustic Doppler velocimetry and flying hot-film anemometry, are described. The ADV parameters and its setup including the traversing mechanisms, data acquisition and the post-processing programs are discussed. The flying hot-film anemometer setup, along with its traversing mechanism, the data acquisition and control components and programs, calibration procedure, and the post-processing programs are explained in detail.

- The validation of flow measurements results for the ADV and the flying hot-film anemometer are presented in Chapter 4. The statistics of an axisymmetric

turbulent jet issued into a quiescent background measured with the ADV and the flying hot-film anemometer are compared to those of previous studies. These statistics include the downstream evolution of the mean axial velocity along the centerline, the profiles of the mean axial and radial velocities, the mean velocity decay constant, the spreading rate, the downstream evolution of the RMS velocity along the axis, the profile of RMS axial velocity, and the evolution of mass flow rate along the axis of the jet. The results shows that the RMS velocities measured by the ADV along the x- and y-direction of the probe are overestimated, while the rest of the statistics are measured accurately by both the ADV and the flying hot-film anemometer. In addition, the ADV has shown itself to be more accurate than the flying hot-film anemometer at low velocities (far downstream and near the edges of the jet). Therefore, the flying hot-film is used for measurements of the mean and RMS axial velocities, while the ADV is used to measure the mean radial velocities, and the mean axial velocity profiles from which the mass flow rate and the half-width are calculated.

- Chapter 5 describes the results in three sections.
  - The first section is an attempt to improve the turbulence statistics measured with the ADV using noise-reduction and post-processing methods. Among the noise-reduction methods suggested in the literature, that of Hurther and Lemmin (2001) improved the turbulence statistics, however the corrected RMS velocities measured by the ADV remained higher than those measured by well established turbulence measurement techniques. We propose a method for improving the turbulence statistics, in which, due to the symmetry of the jet, the two velocity components measuring the radial velocities can be compared, the noise determined and then subtracted from the third component. This method improves the data and can be used in axisymmetric flows or if measurements are conducted with the probe in two different orientations. In addition, it is attempted to relate Doppler noise to the mean velocity (to subsequently subtract the

Doppler noise from the RMS velocity). The results show that the Doppler noise does not appear to be a monotonic function of mean velocity, for the range of velocities studied herein, in contrast with the arguments of Lemmin and Lhermitte (1999).

- In the second section of this chapter, the results of the effect of background turbulence on an axisymmetric turbulent jet are discussed. The velocity statistics, spectra, along with the decay and homogeneity are first measured in the flow generated by the RJA. The results confirm that the turbulence is approximately homogeneous and isotropic and has a low mean flow. Subsequently, the results pertaining to the effect two different levels of the background turbulence on a jet at three different Reynolds numbers are discussed. The statistics measured along the centerline as well as the radial profile of the jet are presented. The results show that the mean axial velocities decay faster in the presence of background turbulence, while the mean radial velocities increase especially close to the edges of the jet. The RMS velocities increase when the background turbulence is present. The half-width of the jet, the mass flow rate and therefore the entrainment into the jet are calculated from the mean velocity profiles. The results show that the jet's width increases in the presence of the background turbulence. The mass flow rate of the jet decreases in the presence of the background turbulence, from which it can be inferred that the entrainment into the jet is reduced.
- The third section of Chapter 5 discusses the results. In the velocity measurements with the ADV, the mean velocities and only the RMS velocity measured along the z-direction of the probe are accurate. The turbulence statistics in the x- and y-directions can be corrected with a noise-reduction method. The relationship of the present study (on the effect of background turbulence on the jet) to previous studies is then discussed. It is argued that as the background turbulence level was increasing in the downstream direction of the jet (in contrast with homogeneous background turbulence in the current study), the conclusions

of these studies are ambiguous due to problems in the experimental design. In the third section, the entrainment mechanisms of the jet – large-scale engulfment and small-scale nibbling – are described and the effect of background turbulence on these mechanisms is discussed. It is concluded that in the presence of background turbulence, engulfment is expected to be the main entrainment mechanism. In addition, the breakup location of the jet and the mean velocity decay exponents of the jet are presented as a function the ratio of the turbulent Reynolds number of the jet and the jet's Reynolds number. As this ratio increases, the breakup location moves closer to the jet exit and the jet decays more rapidly.

6.2 Contributions of the Present Study

- The ADV is a relatively new instrument and has been used for velocity measurements in the laboratory and in the field, often without benchmarking, especially in turbulent flows. This work is the first to present a systematic laboratory benchmarking of the ADV in a well established turbulent flow, the turbulent jet. The jet statistics measured with the ADV are compared to those measured using stationary hot-film anemometry and flying hot-film anemometry (present study) as well as the results of previous studies. We have shown that the mean velocities were predicted accurately, while the RMS velocities measured along the horizontal components (x and y) of the ADV probe were overestimated. The RMS of the vertical velocity component (z) was found to be relatively accurate. Therefore, RMS velocity measurements should not be made without the appropriate post-processing of the data. A noise-reduction method correcting the overestimated RMS velocities is presented. This method reduced the RMS velocities of the jet to the accepted values measured by hot-film anemometry and those reported in the literature. In addition, this study is the first to show that there is no relation between the Doppler noise and the mean velocity, in contrast to the argument of Lemmin and Lhermitte (1999).

- This thesis presents the first systematic study of the effect of different levels of background turbulence on an axisymmetric turbulent jet at various Reynolds numbers. This is the first work to study the effect of homogeneous turbulence on a turbulent jet. In the limited previous studies, the jet axis was perpendicular to the oscillating grid, therefore having background turbulence level increasing in the downstream direction of the jet (*i.e.*, as jet turbulence level decreased). The contributions of this study are as follows:

  1. This work is the first systematic study showing that the mass flow rate, and therefore entrainment into the jet, are reduced by the presence of background turbulence. The mass flow rate still increases with downstream distance, but at a lower rate in the presence of the background turbulence, indicating that entrainment mechanisms are still active. The jet entrainment rate (dm/dx) is 0.34 in a quiescent background and decreases to 0.19 for the low-TKE background (4.44 cm^2/s^2) and to 0.16 for the high-TKE background (9.33 cm^2/s^2). The decrease of mass flow rate is in contrast to the theory of superposition of jet dilution and turbulent diffusion which predicts an increase in the entrainment into the jet in the presence of external turbulence (Wright, 1994). On the other hand, our results confirm i) the hypothesis of Hunt (1994) that the tendency of the jet to break up into distinct eddies by the external turbulence will decrease the entrainment into the jet, and ii) the more qualitative experimental study of Gaskin *et al.* (2004) who detected a decreased entrainment in a plane jet issuing into a shallow co-flow.

  2. This work also showed that the entrainment mechanism may change and be dominated by engulfment in the presence of background turbulence. As the interface between the jet and ambient flow is dominated by the eddies in the order of those of the background turbulence, entrainment cannot be due to the viscous diffusion of vorticity. Therefore, the entrainment due to nibbling by small scales at the interface is ruled out. We hypothesize that

the entrainment is dominated by large-scale engulfment when background turbulence is present.

3. The results of this study show, that in the presence of background turbulence, the mean axial velocity of the jet is reduced when compared to the case of a jet emitted into a quiescent environment. If entrainment is proportional to the characteristic velocity of the jet (Morton *et al.* 1956), then a decrease in centerline velocity would imply a decrease in the rate of entrainment. This argument is consistent with our measurements, which show a decrease in the entrainment rate of the jet in the presence of the background turbulence. Furthermore, the decay rate of the jet axial velocity is faster in the presence of background turbulence. It was observed that in the presence of background turbulence, the jet decay is initially governed by a power-law, which is followed by a faster logarithmic decay. As the intensity of background turbulence increases relative to that of the jet, the power-law decay region get smaller and the transition between the power-law and logarithmic decay regions moves upstream, towards the jet exit. In this work a relationship between the (power-law) decay exponent and the ratio of the turbulent Reynolds number of the background turbulence to the jet Reynolds number is presented. The rate of decay of the jet increases in the presence of background turbulence relative to that of the jet in quiescent background which decays as x^{-1}. By increasing the level of the background turbulence, the rate of decay (in the power-law region) of the mean axial velocities increases. For example, the mean axial velocity of a jet with Re = 10,600, decays as $x^{-1.83}$ for the low-TKE background and as $x^{-2.13}$ for the high-TKE background. For a jet with Re = 5,300, the rate of decay increases from $x^{-2.57}$ for the low-TKE background to $x^{-4.34}$ for the high-TKE background.

4. The jet is also shown to be wider in the presence of the background turbulence. In other words, the half-width, which is a characteristic length scale of the jet, increases in the presence of external turbulence. The

evolution of the jet half-width in the presence of external turbulence is no longer linear (in contrast with a $\sim x^1$ growth of the jet half-width in a quiescent background) and exhibits power-law growth as $\sim x^{1.5}$ and $\sim x^{1.7}$ for the low- and the high-TKE backgrounds, respectively. Although the jet is wider in the presence of the background turbulence, this does not result in an increased entrainment rate, as previously mentioned. As the rate of increase of the width is lower than the rate of decay of the mean velocity, the rate of entrainment into the jet decreased in the presence of background turbulence.

5. The RMS axial velocities of the jet are shown to increase (more than 50% for Re = 5,800 at x/D = 15) in the presence of background turbulence. However, the percentage increase of RMS velocities of the jet in the presence of background turbulence (relative the jet in quiescent background) reduces with the downstream distance. In addition, the RMS velocities asymptote to those of the background turbulence when the jet dies. It should also be noted that, the RMS velocities decrease to background turbulence levels farther downstream than the location at which the mean velocity reached zero indicating that the jet is ultimately reduces to a volume of turbulent flow with no jet structure. Furthermore, the RMS velocities of the jet in the high-TKE background are higher compared to those of the jet in low-TKE background close to the jet exit, *i.e.*, $x/D \leq 35$ for Re = 10,600, and $x/D \leq 15$ for Re = 5,800 and 5,300. This trend changes in the near-field (after the initial development region of the jet) where the RMS velocities of the jet in the low-TKE background are higher than those of the high-TKE background, *i.e.*, $40 \leq x/D \leq 100$ for Re = 10,600, and $20 \leq x/D \leq 45$ for Re = 5,800 and 5,300. This contradicts any notions of superposition of jet and background turbulence. Finally, far downstream (where the measured RMS velocities are close to those of the background turbulence), the RMS velocities of the jet in high-TKE are higher than those of the low-TKE, as must be the case.

6. This work also presents the break up location of the jet as a function of the level of the background turbulence. The break up position is found to be a monotonic function of the ratio of the turbulent Reynolds number of the background turbulence to the jet Reynolds number.

7. It is shown that the background turbulence results in an increase in the outward (positive) mean radial velocities. The profile of the mean radial velocity also confirms that the jet is wider when the background turbulence is present. In addition, the jet's mean radial velocities are less negative at the edges indicating that less fluid is being entrained into the jet, and therefore in the presence of background turbulence, the jet mass flow rate increases at a lower rate in the downstream direction (when compared to a jet in a quiescent background).

8. A list of publications and presentations on this research is presented in Appendix B.

6.3 Recommendations for Future Work

- The main objective of this work was to study the effect of different levels of background turbulence on a jet. The author recommends studying higher levels of turbulent kinetic energy of the background turbulence on the jet to further understand the effect of background turbulence on a jet. It would be interesting to see if the entrainment rate remains constant at higher levels of the background turbulence. In addition, by studying more cases, a relationship can be found between the TKE of the background turbulence and the entrainment rate for a given Reynolds number. In this thesis, two different levels of background turbulence were studied. To investigate the higher level of background turbulence, increasing the number of the jets (pumps) of the random jet array may be required. Furthermore, by studying the effect of background turbulence on the entrainment rate of jets at a range of Reynolds

numbers, a relationship can be found between the entrainment rate and the Reynolds number at a given background turbulence TKE.

- Measurements of the RMS radial velocities of the jet in the presence of background turbulence could also provide more information on this problem. By measuring the RMS radial velocities, it can be seen if the RMS radial velocities increase similar to the RMS axial velocities.

- To better understand the effect of background turbulence on a jet, it will be essential to investigate the concentration field of the jet using techniques such as laser induced fluorescence (LIF). LIF measurements of the effect of different levels of background turbulence on a jet can give more information regarding the dilution of the jet and entrainment into the jet. The measurement of a scalar field will also allow the contribution of the turbulent background on dilution to be determined. In addition, it will be interesting, to compare the velocity field to the concentration field of a turbulent jet in the presence of background turbulence. Furthermore, visual inspection of the process using the planar LIF can give more detail on the effect of background turbulence on the concentration of the jet as well as the entrainment into the jet.

References

Birouk, M., Sarh B., and Gokalp I. 2003. An attempt to realize experimental isotropic turbulence at low Reynolds number. Flow, Turbulence and Combustion, 70 (1-4): 325-348.

Brown, G. L. and Roshko, A. 1974. Large scales in the developing mixing layer. Journal Fluid Mechanics 64: 775-816.

Bruun, H. H. 1995. Hot-wire Anemometry, Oxford University Press.

Bruun, H. H. 1996. Hot-film anemometry in liquid flows. Measurement Science and Technology 7: 1301-1312.

Cabrera, R., Deines, K., Brumley, B., Terray, E. 1987. Development of a practical coherent acoustic Doppler current profiler. Conference proceedings of Ocean 87, Halifax, NS, Canada, IEEE Oceanic Engineering society, 93-97.

Cea, L., Puertas, J., and Pena, L. 2007. Velocity measurements on highly turbulent free surface flow using ADV. Experiments in Fluids 42:333-348.

Ching, C.Y., Fernando, H.J.S. and Robles, A. 1995. Break down of line plumes in turbulent environments. Journal of Geophysical Research, 100 (C3): 4707-4713.

Corrsin, S. and Kistler, A. L. 1955. Free-stream boundaries of turbulent flows. NACA TR 1244.

Crow, S., and Champagne, F., 1971, Orderly Structure of Jet Turbulence. Journal Fluid Mechanics. 48: 547–596.

Cuthbertson, A.J.S., Malcangio, D., Davies, P.A. and Mossa, M. 2006. The influence of a localized region on turbulence on the structural development of a turbulent, round, buoyant jet. Fluid Dynamics research, 38: 683-698.

Dahm, W. J. A. and Dimotakis, P. E. 1987. Measurements of entrainment and mixing in turbulent jets. AIAA J. 25: 1216-1223 (also, AIAA Pap. 85-0056).

Dahm, W. J. A. and Dimotakis, P. E. 1990. Mixing at large Schmidt number in the self-similar far field of turbulent jets. Journal of Fluid Mechanics 217:299-330.

De Silva, I.P.D. and Fernando, H.J.S. 1994. Oscillating grids as a source of nearly isotropic turbulence. Physics of Fluids, 6: 2455-2465.

Dimotakis, P. E. 2000. The mixing transition in turbulent flows. Journal of Fluid Mechanics, 409: 69-98.

Dombroski, D.E. and Crimaldi, J.P. 2007. The accuracy of acoustic Doppler velocimetry (ADV) measurements in turbulent boundary layer flows over a smooth bed. Limnology and Oceanography Methods 5:23-33.

Falcone, A.M. and Cataldo, J.C. 2003. Entrainment Velocity in an Axisymmetric Turbulent Jet. Journal of Fluids Engineering. 125: 620-627.

Ferdman, E., Ötügen, M.V. and Kim, S. 2000 Effect of Initial Velocity Profile on the Development of Round Jets. Journal of Propulsion Power 16, 676-686.

Fernando, H.J.S. and De Silva, I.P.D. 1993. Note on secondary flows in oscillating-grid, mixing-box experiments. Physics of Fluids, A5 (7): 1849-1851.

Fischer, H.B., List, E.J., Koh, R.C.Y., Imberger, J. and Brooks, N.H. 1979 *Mixing in inland and coastal waters*, Academic Press.

Fukushima, C. Aanen, L., and Westerweel, J. 2002. Investigation of the mixing process in an axisymmetric turbulent jet using PIV and LIF: Laser Techniques for Fluid Mechanics, 339-356.

Gaskin, S.J., McKernan, M and Xue, F. 2004. The effect of background turbulence on jet entrainment: an experimental study of a plane jet in a shallow coflow. Journal of Hydraulic Research, 42(5): 531-540.

Gaskin, S. and Wood, I.R., 1993. Advected Line Thermals in Non-turbulent and turbulent ambent. 11th Australian Conference on Coastal and Ocean Engineering Preprints, Townsville, Australia, 748-751.

Goring, D.G. and Nikora, V.I., 2002. Despiking acoustic Doppler velocimeter data. Journal of Hydraulic Engineering 128(1): 117-126

Guo, Y., Davies, P.A., Fernando, H.J.S. and Ching, C.Y. 1999 Influence of background turbulence on the evolution of turbulent jets. Conference proceedings of the 28th IAHR congress.

Guo, Y., Malcangio, D., Davies, P.A. and Fernando, H.J.S. 2005 A laboratory investigation into the influence of a localized region on turbulence on the evolution of a round turbulent jet. Fluid Dynamics research, 36: 78-89.

Hurther, D. and Lemmin, U., 2008. Improved Turbulence Profiling with Field-Adapted Acoustic Doppler Velocimeters Using a Bifrequency Doppler Noise

Suppression Method. Journal of Atmospheric and Oceanic Technology 25, 452–463.

Hurther, D. and Lemmin, U., 2001. A correction method for turbulence measurements with a 3D acoustic Doppler velocity profiler. Journal of Atmospheric and Oceanic Technology 18, 446-458.

Hopfinger, E.J. and Toly, J.A. 1976 Spatially decaying turbulence and its relation to mixing across density interfaces. *J. Fluid Mech*. **78**, 155-175.

Hunt, J.C.R. 1994. Atmospheric jets and plumes, In: Davies, P.A. and Valente Neves, M.I. (eds.), Recent Research Advances in the Fluid Mechanics of Turbulent Jets and Plumes, NATO ASI Series E, 255: 309-334.

Hussein, H.J., Capp, S.P. and George, W.K. 1994. Velocity-measurements in a high-Reynolds-number, momentum-conserving, axisymmetrical, turbulent jet. Journal of Fluid Mechanics 258: 31-75.

Hwang, W and Eaton, J.K. 2004. Creating homogeneous and isotropic turbulence without a mean flow. Experiments in Fluids, 36 (3): 444–454.

Jørgensen, F.E. 2002. How to measure turbulence with hot-wire anemometers. Dantec Dynamics publication.

Law, A.W.K., Cheng, N.-S. and Davidson, M.J. 2001. Jet spreading in oscillating-grid turbulence, Proceedings of the 3rd International Symposium on Environmental Hydraulics, IAHR, Tempe, Arizona, 1-6.

Lemmin, U. and Lhermitte, R. 1999. Discussion of 'ADV measurements of turbulence: Can we improve their interpretation? by V. I. Nikora, and D. G. Goring. Journal of Hydraulic Engineering 125_9: 987–988.

Lhermitte, R. and Lemmin, U. 1994. Open-channel flow and turbulence measurement by high-resolution Doppler sonar. Journal of Atmospheric and Oceanic Technology 11: 1295-1308.

Lohrmann, A., Cabrera, R., and Kraus, N.C. 1994. Acoustic Doppler velocimeter (ADV) for laboratory use. In Proceedings of the Symposium on Fundamentals and Advancements in Hydraulics Measurements and Experimentation, C. A. Pugh, ed., ASCE, 351-365.

Mathew, J. and Basu, A. 2002 Some characteristics of entrainment at a cylindrical turbulence boundary. Physics of Fluids 14: 2065–2072.

McDougall, T.J. 1979. Measurements of turbulence in a zero-mean shear mixed layer Journal of Fluid Mechanics, 94 (3): 409–431.

McKenna, S.P. and McGillis, W.R. 2004. Observations of flow repeatability and secondary circulation in an oscillating grid-stirred tank. Physics of Fluids, 16 (9): 3499-3502.

Ming, H. and Hongwu, T. and Huimin W. 2001. Applying ADV to a round jet flow. In Proc. 29th IAHR Congress: 21st Century: The New Era for Hydraulic Research and Its Applications. Beijing, China.

Morton, B.R., Taylor, G.I. and Turner, J.S. 1956. Turbulent gravitational convection from maintained and instantaneous sources. Proceedings of the Royal Society, London, Series A, 234: 1-23.

Mydlarski, L. and Warhaft, Z., 1996. On the onset of high-Reynolds-number grid-generated wind tunnel turbulence. Journal of Fluid Mechanics 320: 331-368.

Nikora, V.I. and Goring, D.G. 1998. ADV measurements of turbulence: Can we improve their interpretation? Journal of Hydraulic Engineering 124(6): 630-634.

Panchapakesan, N.R. and Lumley, J.L. 1993a. Turbulence measurements in axisymmetric jets of air and helium. Part 1. Air jet. Journal of Fluid Mechanics 246: 197-223.

Pope, S.B., 2000. Turbulent Flow, Cambridge University Press.

Raju, N. and Meiburg, E. 2005. The accumulation and dispersion of heavy particles in forced two-dimensional mixing layers. Part 2: The effect of gravity. Physics of Fluids, 7 (6): 1241-1264.

Ricou, F.P. and Spalding, D.B. 1961. Measurements of entrainment by axisymmetrical turbulent jets. Journal of Fluid Mechanics 11: 21-32.

Srdic, A., Fernando, H.J.S. and Montenegro, L. 1996. Generation of nearly isotropic turbulence using two oscillating grids. Experiments in Fluids, 20: 395-397.

Taylor, J.R., 1997. An Introduction to Error Analysis, University Science Books.

Tennekes, H. and Lumley, J. L., 1972. A First Course in Turbulence, MIT Press.

Thompson, S. and Turner, J. S. 1975. Mixing across an interface due to turbulence generated by an oscillating grid. Journal of Fluid Mechanics 67, 349-368.

Townsend, A. A. 1956. The Structure of Turbulent Shear Flow, 1st edn. Cambridge University Press.

Tsai, Y. S., Hunt, J. C. R., Nieuwstadt, F. T. M., Westerweel, J. and Gunasekaran, B. P. N. 2007. Effect of Strong External Turbulence on a Wall Jet Boundary Layer, Flow, Turbulence and Combustion 79:155-174.

Turner, J. S. 1986. Turbulent entrainment: the development of the entrainment assumption, and its application to geophysical flows. Journal of Fluid Mechanics 173: 431-471.

Variano, E.A., Bodenschatz, E. and Cowen, E.A. 2004. A random synthetic jet array driven turbulence tank. Experiments in Fluids 37: 613-615.

Variano, E.A. and Cowen, E.A. 2008. A random-jet-stirred turbulence tank. Journal of Fluid Mechanics 604: 1-32.

Vectrino Velocimeter User Guide, Nortek, 2004.

Voulgaris, G. and Trowbridge, J.H. 1998. Evaluation of the acoustic Doppler velocimeter (ADV) for turbulence measurements. Journal of Atmospheric and Oceanic Technology 15: 272-289.

Wahl, T.L. 2003. Discussion of "Despiking Acoustic Doppler Velocimeter Data" by Derek G. Goring and Vladimir I. Nikora. Journal of Hydraulic Engineering 129:484-488.

Webster, D., Roberts, P. and Ra'ad, L. 2001. Simultaneous DPTV/PLIF measurements of turbulent jet. Experiments in Fluids, 30:65-72.

Westerweel, J., Fukushima, C., Pedersen, J.M. and Hunt, J.C.R. 2009. Momentum and scalar transport at the turbulent/non-turbulent interface of a jet. Journal of Fluid Mechanics 631:199-230.

Wright, S.J. 1994. The effect of ambient turbulence on jet mixing, In: Davies, P.A. and Valente Neves, M.I. (eds.), Recent Research Advances in the Fluid Mechanics of Turbulent Jets and Plumes, NATO ASI Series E, 255: 13-27.

Wygnanski, I. and Fiedler, H. 1969 Some measurements in the self-preserving jet. Journal of Fluid Mechanics 38: 577-612.

Xu, G. and Antonia, R.A. 2002 Effect of different initial conditions on a turbulent round free jet. Experiments in Fluids 33: 677-683.

Ying, C., Davidson, M., Wang H., and Law, A. 2004. Radial velocities in axisymmetric jets and plumes. Journal of Hydraulic Research, 42:29-33.

Appendix A: Sources of Error and Uncertainty Analysis

In this section, an uncertainty analysis is performed for the velocity measurements conducted by both acoustic Doppler velocimetry and flying hot-film anemometry. The uncertainty for each individual source of error is first calculated. The contributions of individual sources of error are then combined to calculate the total relative standard uncertainty. In the case of the ADV measurements, the uncertainty analysis models of Voulgaris and Trowbridge (1998) and Taylor (1997), and in the case of the flying hot-film anemometer measurements, the uncertainty analysis models of Jørgensen (2002) and Taylor (1997) are used to calculate the relative standard uncertainty for individual sources of error.

A.1 Acoustic Doppler Velocimetry Uncertainties

Voulgaris and Trowbridge (1998) divided the total velocity error along each receiver beam of the ADV (σ_t) into three categories: i) sampling error (σ_m), caused by the inability of the system to accurately resolve the changes in phase of the return pulse, ii) Doppler noise (σ_D), and iii) mean velocity shear within the sampling volume (σ_u). The uncertainties corresponding to each of these sources of error are calculated in the following sections. Lohrmann *et al.* (1994) divided the measured instantaneous velocity ($\tilde{U}$) into a mean velocity, a fluctuating part (u) and the Doppler noise (σ_D), *i.e.*, $\tilde{U} =< U > + u + \sigma_D$. They showed that the Doppler noise does not affect the mean velocity, *i.e.*, $< u + \sigma_D >= 0$, but affects the velocity variance, *i.e.*, $< (u + \sigma_D)^2 >=< u^2 > + < \sigma_D{}^2 >$. Therefore, the contributions of all three sources of error will be considered in the calculations of

uncertainty for the RMS velocities, however, only the contributions of the sampling error and the mean velocity shear within the sampling volume will be accounted for in the calculations of uncertainty for the mean velocities. The relative uncertainty is then calculated for each velocity component. The calculations are conducted for velocities measured along the axis of the jet over the range $35 \leq x/D \leq 110$.

A.1.1 Sampling Error

Sampling error is related to the accuracy of the ADV's A/D board in resolving the changes in phase and the electronically induced noise. This error is independent of the flow and depends on the pulse length, which is set by the velocity range of the ADV. The sampling error uncertainty can be calculated as follows (Voulgaris and Trowbridge, 1998):

$$\sigma_m^2 = \frac{c^2}{4}\frac{1}{f_{ADV}^2}\frac{1}{4\pi^2}K^2\sigma_s^2\frac{1}{\tau}\frac{1}{\left(T_{ADV}-t_0\right)},$$

where c is the speed of sound in water (1,481 m/s at 20° C), f_{ADV} is the ADV's operating frequency (10 MHz), K is an empirical constant (1.4), σ_s is the system uncertainty to resolve the phase (1.08 for the velocity range of ±0.3 m/s), τ is the time between transmissions (4.35 ms for the velocity range of ±0.3 m/s), T_{ADV} is the time between two successive estimates of velocity (0.04 s at a sampling frequency of 25 Hz), and t_0 is the time that takes the sensor to carry out the necessary conversions (2 ms).

Using the above equation, the sampling error or σ_m^2 is 1.923×10^{-6} m^2/s^2 for $35 \leq x/D \leq 110$. This value does not change as the velocity range setting was not changed over the range of downstream distances used herein.

A.1.2 Doppler Noise

Doppler noise is an intrinsic feature of all Doppler backscatter systems and is flow-related. This noise is due to (1) turbulence and particle scattering, (2)

beam divergence, and (3) the finite residence time of the particles in the sampling volume. Doppler noise is a white noise and does not affect the mean velocity (Lohrmann *et al.*, 1994). Voulgaris and Trowbridge (1998) presented the following equation for calculating the uncertainty due to the Doppler noise:

$$\sigma_D^2 = \frac{\pi^{-1/2}}{16}\frac{c^2 B_D}{f_{ADV}^2 M_{ADV}\tau},$$

where B_D is the total Doppler bandwidth broadening which is the RMS of three individual contributions of turbulence (B_t), beam divergence (B_d) and finite residence time (B_r), *i.e.*, $B_D^2 = B_t^2 + B_d^2 + B_r^2$, and M_{ADV} is the number of acoustic pulses averaged for calculating the radial velocities (~11).

B_t is due to turbulent scales on the order of the sampling volume or smaller, which cause the particles to have a distribution of velocities within the sampling volume. This quantity can be estimated to be (Cabrera *et al*. 1987):

$$B_t = 2.4\frac{f_{ADV}(\varepsilon d)^{1/3}}{c},$$

where ε is the turbulence dissipation rate (calculated from u^3/ℓ, where u is the u_{rms} at the centerline and ℓ is the integral length scale of the jet), and d is the transverse size of the sampling volume (9 mm). B_t is shown in the following table:

x/D	ε (m^2/s^3)	B_t (1/s)
35	1.09×10^{-2}	748.3
42.5	5.73×10^{-3}	603.2
50	3.26×10^{-3}	499.6
60	1.77×10^{-3}	407.4
75	8.17×10^{-4}	315.2
90	3.80×10^{-4}	244.2
110	1.56×10^{-4}	181.4

Beam divergence can be calculated from the following equation (Cabrera *et al*. 1987):

$$B_d = 0.84\sin(\Delta\theta)\frac{f_{ADV}U_c}{c},$$

where $\Delta\theta$ is the bistatic angle, the angle bisector between the transmitter and receiver (15° for Vectrino ADV), and U_c is the cross-beam or transverse velocity component (<V>). B_d is estimated in the following table:

x/D	<V> (m/s)	B_d (1/s)
35	-0.001	-4.8
42.5	-0.001	-4.4
50	-0.001	-4.1
60	-0.002	-5.8
75	-0.003	-11.7
90	-0.002	-7.6
110	-0.002	-6.8

The uncertainty due to residence time can be calculated from the following equation (Cabrera *et al*. 1987):

$$B_r = 0.2\frac{U_h}{d},$$

where U_h is the mean horizontal speed (which is substituted by U_{CL}). B_r is estimated in the following table:

x/D	U_h (m/s)	B_r (1/s)
35	0.25	5.5
42.5	0.20	4.4
50	0.17	3.7
60	0.13	3.0
75	0.10	2.3
90	0.09	2.0
110	0.07	1.6

B_D, the RMS of the sum of the three individual contributions used to calculate σ_D^2, as well as σ_D^2 itself, are shown in the following table:

x/D	B_D (1/s)	σ_D^2 (m^2/s^2)
35	1176.5	1.90×10^{-5}
42.5	951.8	1.54×10^{-5}
50	790.3	1.28×10^{-5}
60	643.0	1.04×10^{-5}
75	498.4	8.06×10^{-6}
90	405.5	6.56×10^{-6}
110	314.9	5.09×10^{-6}

A.1.3 Mean Velocity Shear

This error is due to mean velocity gradients in the sampling volume. This error becomes important in sharp velocity gradient flows such as boundary layers. Here we estimate this error at the centerline of the axisymmetric turbulent jet based on the following equation presented by Voulgaris and Trowbridge (1998):

$$\sigma_u^2 = \frac{(\Delta U)^2}{3}$$

where ΔU is the variation of the velocity across the sampling volume which is estimated by the variation of the mean velocity at the centerline of the jet within 9 mm which is the length of the sampling volume. σ_u^2 is presented in the following table:

x/D	ΔU (m/s)	σ_u^2 (m^2/s^2)
35	5.29×10^{-3}	9.32×10^{-6}
42.5	2.92×10^{-3}	2.85×10^{-6}
50	1.76×10^{-3}	1.03×10^{-6}
60	9.96×10^{-4}	3.31×10^{-7}
75	4.96×10^{-4}	8.20×10^{-8}
90	2.89×10^{-4}	2.79×10^{-8}
110	1.54×10^{-4}	7.91×10^{-9}

A.1.4 Total Uncertainty for the Acoustic Doppler Velocimetry Measurements

To calculate the total uncertainty, the following equation is used assuming random independent errors (Taylor, 1997):

$$Total\ Uncertainty = \sqrt{(\text{uncertainty}_1)^2 + (\text{uncertainty}_2)^2 + (\text{uncertainty}_3)^2 + \ldots}$$

The total velocity uncertainty (σ_t^2) pertaining to the RMS velocity along each receiver beam of the ADV is the sum of sampling error (σ_m^2), Doppler noise (σ_D^2), and mean velocity shear within the sampling volume (σ_u^2), *i.e.*, $\sigma_{t\text{-}rms}^2 = \sigma_m^2 + \sigma_D^2 + \sigma_u^2$, which is presented in the following table:

x/D	$\sigma_{t\text{-}rms}^2$ (m^2/s^2)
35	2.33×10^{-5}
42.5	1.45×10^{-5}
50	1.10×10^{-5}
60	8.84×10^{-6}
75	7.10×10^{-6}
90	5.90×10^{-6}
110	4.87×10^{-6}

The total velocity uncertainty (σ_t^2) pertaining to the mean velocity along each receiver beam of the ADV is the sum of sampling error (σ_m^2), and mean velocity shear within the sampling volume (σ_u^2), *i.e.*, $\sigma_{t\text{-}mean}^2 = \sigma_m^2 + \sigma_u^2$, which is presented in the following table:

x/D	$\sigma_{t\text{-}mean}^2$ (m^2/s^2)
35	1.12×10^{-5}
42.5	4.77×10^{-6}
50	2.96×10^{-6}
60	2.25×10^{-6}
75	2.00×10^{-6}
90	1.95×10^{-6}
110	1.93×10^{-6}

If the receiver transducers are identical and ideal, then we can assume that the noise variance is the same along each receiver beam. Using the transformation matrix, σ_t^2 is calculated for each velocity component. The variance of noise in x-, y- and z-direction are denoted by σ_x^2, σ_y^2, and σ_z^2, respectively and are presented in the following tables for the RMS velocity and mean velocity:

x/D	$\sigma_{x\text{-}rms}^2$ (m^2/s^2)	$\sigma_{y\text{-}rms}^2$ (m^2/s^2)	$\sigma_{w\text{-}rms}^2$ (m^2/s^2)	$\sigma_{x\text{-}mean}^2$ (m^2/s^2)
35	1.90×10^{-4}	1.92×10^{-4}	1.24×10^{-5}	4.53×10^{-5}
42.5	1.18×10^{-4}	1.20×10^{-4}	7.74×10^{-6}	1.92×10^{-5}
50	8.97×10^{-5}	9.09×10^{-5}	5.88×10^{-6}	1.19×10^{-5}
60	7.19×10^{-5}	7.28×10^{-5}	4.71×10^{-6}	9.09×10^{-6}
75	5.78×10^{-5}	5.85×10^{-5}	3.79×10^{-6}	8.09×10^{-6}
90	4.80×10^{-5}	4.86×10^{-5}	3.15×10^{-6}	7.87×10^{-6}
110	3.96×10^{-5}	4.01×10^{-5}	2.59×10^{-6}	7.79×10^{-6}

The total relative uncertainties for RMS velocity and mean velocity, *i.e.*, $(\sigma_i^2/\langle u_i^2\rangle)^{1/2}$ and $(\sigma_i^2/\langle U\rangle^2)^{1/2}$, for the ADV velocity measurements are calculated and presented in the following table:

x/D	% u_{rms} error	% v_{rms} error	% w_{rms} error	% $<U>$ error
35	2.09	2.69	0.58	0.03
42.5	1.76	2.29	0.45	0.02
50	1.75	2.32	0.43	0.01
60	1.86	2.51	0.44	0.02
75	2.16	3.03	0.48	0.02
90	2.64	3.41	0.58	0.04
110	3.45	4.60	0.67	0.05

The total relative uncertainty of the RMS velocities for the acoustic Doppler velocimetry velocity measurements is calculated to be ~3% for the horizontal RMS velocities and less than 1% for the vertical RMS velocity. The mean velocity measured by the ADV has an error of less than 0.1%. Voulgaris and Trowbridge (1998) estimated the ADV's mean velocity error of ~1%. 3% uncertainty in the RMS velocity and 0.1% uncertainty in the mean velocity results in 3% uncertainty in $u_{rms}/<U>$ and $v_{rms}/<U>$. This value is much smaller than the observed error in turbulence intensity measurements using the ADV in an axisymmetric turbulent jet, which was more than 30% (relative to the stationary and flying hot-film anemometer measurements of the present study and the measurements of Hussein *et al.* (1994)) as shown in Chapter 4. This indicates that the above analysis does not account for all sources of error.

A.2 Flying Hot-Film Anemometry Uncertainties

The sources of error in the flying hot-film anemometry measurements can be caused by: i) the anemometer, ii) ambient effects/drifts, iii) the calibration curve-fit and the traversing mechanism, and iv) the DAQ board resolution. These will be discussed and the uncertainty corresponding to each source of error will be calculated in the following sections.

A.2.1 Constant Temperature Anemometer

The constant temperature anemometer has low noise and good repeatability and therefore, these factors have negligible uncertainty compared to the other sources of error (Jørgensen, 2002). In addition, the frequency response and the electronic noise do not affect the large-scale quantities measured in this study.

A.2.2 Ambient Effects/Drifts

One of the largest sources of error for the anemometer is the calibration drift caused by probe fouling and temperature changes. This error mostly affects the mean velocities rather than RMS velocities as u_{rms} is a function of the slope of the calibration curve, *i.e.*, $u_{rms} = \frac{d<U>}{dE} \times E_{rms}$, (and not the absolute value of the output voltage) which does not vary significantly when a calibration drifts. To minimize the effects of calibration drift, two calibrations, one immediately before and one immediately after each test were conducted. For a given hot-film calibration, the probe was moved (using the traversing mechanism) at 19 different speeds from 0.01-1.1 m/s. If any significant shift in the final calibration was observed, the experiment was repeated. Assuming the calibration drift to be linear in time, the average of the two calibration curves was used to analyse the data. To calculate the uncertainty due to this averaging, the standard deviation of the averaging error is calculated. The following equation returns the relative uncertainty due to calibration drift (Taylor, 1997):

$$Uncertainty = \sqrt{\frac{1}{N-1}\sum_{i=1}^{N}\left(\frac{U_{i,Average} - U_{i,measured}}{U_{i,Average}}\right)^2} \times 100\%$$

where N = 19 is the number of data points in the calibration, $U_{i,\ measured}$ is the measured velocity, and $U_{i,\ average}$ is the average of U_i measured before and after each test at the same voltage.

The relative standard uncertainty due to using an average calibration (based on three typical calibration curves) is 2.1%. As mentioned earlier, this number pertains to mean velocity measurement and is expected to be smaller for RMS measurements.

A.2.3 Calibration Curve-Fit and the Traversing Mechanism

The curve-fit to the calibration data results in an uncertainty in velocity measurements. This uncertainty also includes the error (in the measured velocity) resulting from the traversing mechanism. For the flying hot-film anemometry experiments, the speed of the traversing mechanism was subtracted from the measured velocity obtained from the calibration curve. The speed of the traversing mechanism is subject to error itself. Ideally, the speed of the traversing mechanism should be the same as that measured by the hot-film anemometer probe. The uncertainty from the curve-fit and the traversing mechanism is found by the following equation:

$$Uncertainty = \sqrt{\frac{1}{N-3}\sum_{i=1}^{N}\left(\frac{U_{i,curve-fit}-U_{i,TM}}{U_{i,curve-fit}}\right)^2}\times 100\%$$

where N-3 results from having three degrees of freedom, A, B, and n in $E^2 = A + BU^n$ (Taylor, 1997). $U_{i,\ curve}$ is the velocity predicted by the curve-fit and $U_{i,TM}$ is the traversing mechanism velocity set through the controller.

Using the above equation, the relative standard uncertainty (based on three typical calibration curves) is 2.9%. Note that, this uncertainty also includes the contributions from the flow disturbances and the oscillations caused by the traversing mechanism.

A.2.4 DAQ Board Resolution

The data acquisition board resolution uncertainty can be estimated by the following expression (Jørgensen, 2002):

$$Uncertainty = \left(\frac{1}{\sqrt{3}} \frac{E_{DAQ}}{2^n} \frac{1}{U} \frac{\partial U}{\partial E} \right) \times 100\%$$

where, E_{DAQ} is the input voltage span of the A/D board (20 V), n is the resolution of the board (16 bits), and U the velocity and $\partial U/\partial E$ is the slope of the inverse calibration curve (the maximum value for $\frac{1}{U}\frac{\partial U}{\partial E}$ is 0.04).

The relative standard uncertainty for the DAQ board is 0.001% which is negligible relative to the other uncertainties calculated from other sources.

A.2.5 Total Uncertainty for the Flying Hot-Film Anemometry Measurements

To calculate the total uncertainty, the equation presented in A.1.4 is used. The total relative uncertainty for the flying hot-film anemometry measurements is 3.6%. The relative uncertainty is also calculated from three velocity measurement experiments conducted (using the flying hot-film anemometer) along the centerline of the jet. 20 points in the range of $15 \leq x/D \leq 110$ were analysed and the results showed that the relative uncertainty for the mean velocity and RMS velocity are 3% and 4%, respectively. This is in agreement with the theoretical calculations of the total relative uncertainty.

Appendix B: Publications and Presentations

- Khorsandi, B., Gaskin, S.J., and Mydlarski, L., 2011. The effect of background turbulence on the dynamics and mixing of an axisymmetric turbulent jet. In preparation for submission to the Journal of Fluid Mechanics.

- Khorsandi, B., Mydlarski, L., and Gaskin, S.J., 2011. Noise in turbulence measurements using acoustic Doppler velocimetry. Submitted to the Journal of Hydraulic Engineering.

- Khorsandi, B., Mydlarski, L., and Gaskin, S.J., 2009. Laboratory study of noise in turbulence measurements using acoustic Doppler velocimetry.
  - Presented at the Nortek Symposium, Newport, RI, March 16-18, 2011.

- Khorsandi, B., Gaskin, S.J. and Mydlarski, L., 2010. Flying-hot-film anemometry measurements of the effect of background turbulence on a turbulent jet.
  - Presented at The sixth International Symposium on Environmental Hydraulics (ISEH V), Athens, Greece, June 23-25, 2010.
  - Published in the Proceedings of the 6th International Symposium on Environmental Hydraulics, International Association of Hydraulic Engineering and Research. (6 pages)

- Khorsandi, B., Mydlarski, L., and Gaskin, S.J., 2009. A laboratory study of noise in turbulence measurements using acoustic Doppler velocimetry.
  - Presented at The 33rd International Association of Hydraulic Engineering and Research (IAHR) Congress, Vancouver, BC, August 9-14, 2009.
  - Published in the Proceedings of the 33rd International Association of Hydraulic Engineering and Research (IAHR) Congress: Water Engineering for a Sustainable Environment. (7 pages)

- Khorsandi, B., Gaskin, S.J. and Mydlarski, L., 2008. The effect of background turbulence on the entrainment into an axisymmetric turbulent jet.
  - Presented at the 2nd International Symposium on Shallow Flows (ISSF), Hong Kong, China, December 10-12, 2008.
  - Published in the Proceedings of the 2nd International Symposium on Shallow Flows. (6 pages)

- Khorsandi, B., Gaskin, S.J.* and Mydlarski, L., 2007. Effect of background turbulence on the velocity field of a turbulent jet.
  - Presented at the 5th International Symposium on Environmental Hydraulics (ISEH V), Tempe, Arizona, December 4-7, 2007*.
  - Published in the Proceedings of the 5th International Symposium on Environmental Hydraulics, International Association of Hydraulic Engineering and Research. (6 pages)

- Khorsandi, B., Lavertu, T., Gaskin, S.J. and Mydlarski, L., 2007. A random jet array for laboratory studies of jet dilution within a turbulent environment.
  - Presented at The Eighteenth Canadian Hydrotechnical Conference and Symposium, Winnipeg, MB, August 22-24, 2007.
  - Published in the Proceedings of the Eighteenth Canadian Hydrotechnical Conference, Canadian Society for Civil Engineering, Paper HYD-057 (10 pages).